

DISSERTATION

ASSIMILATION OF GEOSTATIONARY, INFRARED
SATELLITE DATA TO IMPROVE FORECASTING OF MID-
LEVEL, MIXED-PHASE CLOUDS

Submitted by

Curtis J. Seaman

Department of Atmospheric Science

In partial fulfillment of the requirements
for the Degree of Doctor of Philosophy

Colorado State University

Fort Collins, Colorado

Spring 2009

UMI Number: 3374619

INFORMATION TO USERS

The quality of this reproduction is dependent upon the quality of the copy submitted. Broken or indistinct print, colored or poor quality illustrations and photographs, print bleed-through, substandard margins, and improper alignment can adversely affect reproduction.

In the unlikely event that the author did not send a complete manuscript and there are missing pages, these will be noted. Also, if unauthorized copyright material had to be removed, a note will indicate the deletion.

UMI[®]

UMI Microform 3374619
Copyright 2009 by ProQuest LLC
All rights reserved. This microform edition is protected against
unauthorized copying under Title 17, United States Code.

ProQuest LLC
789 East Eisenhower Parkway
P.O. Box 1346
Ann Arbor, MI 48106-1346

COLORADO STATE UNIVERSITY

February 2, 2009

WE HEREBY RECOMMEND THAT THE DISSERTATION PREPARED UNDER OUR SUPERVISION BY CURTIS J. SEAMAN ENTITLED ASSIMILATION OF GEOSTATIONARY, INFRARED SATELLITE DATA TO IMPROVE FORECASTING OF MID-LEVEL, MIXED-PHASE CLOUDS BE ACCEPTED AS FULFILLING IN PART REQUIREMENTS FOR THE DEGREE OF DOCTOR OF PHILOSOPHY.

Committee on Graduate Work

M. R. Azimi-Sabaji

Outside Committee Member Mahmood R. Azimi

William R. Cotton

Committee Member William R. Cotton

Wayne Schubert

Committee Member Wayne H. Schubert

Thomas H. Vonder Haar

Adviser Thomas H. Vonder Haar

Richard H. Johnson

Department Head Richard H. Johnson

ABSTRACT OF DISSERTATION

ASSIMILATION OF GEOSTATIONARY, INFRARED SATELLITE DATA TO IMPROVE FORECASTING OF MID-LEVEL, MIXED-PHASE CLOUDS

Mid-level, mixed-phase clouds (altocumulus and altostratus) are difficult to forecast due to the fact that they are generally thin and form in areas of weak vertical velocity where operational models typically have poor vertical resolution and poor moisture initialization. This study presents experiments designed to test the utility of assimilating infrared window and water vapor channels from the Geostationary Operational Environmental Satellite (GOES) instruments, Imager and Sounder, into a mesoscale cloud-resolving model to improve model forecasts of mid-level clouds. The Regional Atmospheric Modeling Data Assimilation System (RAMDAS) is a four-dimensional variational (4-DVAR) assimilation system used to test the viability of assimilating cloudy scene radiances into a cloud-free initial model state for one case of a long-lived, isolated altocumulus cloud over the Great Plains of the United States. Observations from one observation time are assimilated and significant innovations are achieved. Three experiments are performed: 1) assimilation of the 6.7 μm (water vapor) and 10.7 μm (window) channels from GOES Imager, 2) assimilation of the 7.02 μm (water vapor) and 12.02 μm (window) channels from GOES Sounder, and 3) assimilation of the 6.7 μm channel from GOES Imager and the 7.02 μm channel from GOES Sounder. It is shown that the GOES Sounder channels provide more useful information than the GOES

Imager channels due to increased sensitivity to the mid-troposphere. The decorrelation lengths and variance used in the background error covariance are varied and the impact on the results of the experiments is discussed. The effect of constraining the surface temperatures during assimilation of the window channels is also discussed. It is found that, in a cloud-free initial model state, the adjoint sensitivities are calculated on the assumption that there is no cloud, even with cloud in the satellite observations. This has a significant impact on the success of other 4-DVAR satellite data assimilation experiments.

Curtis J. Seaman

Department of Atmospheric Science

Colorado State University

Fort Collins, Colorado 80523

Spring 2009

ACKNOWLEDGMENTS

This work would not have been possible were it not for the following people: my advisor, Tom Vonder Haar, who made this research possible, and provided valuable guidance; my committee members, Bill Cotton, Wayne Schubert, and Mo Azimi, who provided advice and constructive criticism; Tomi Vukićević, who inspired this work and briefly served as a committee member before transferring to the University of Colorado; Adam Kankiewicz, project manager of CLEX before his departure to WindLogics, Inc. and master of IDL and PowerPoint; the exceedingly helpful research scientists at CIRA, including, in no particular order, Scott Longmore, Manajit Sengupta, Andy Jones, John Forsythe, Steve Fletcher, Laura Fowler, Stan Kidder, Cindy Combs, Louie Grasso, and Adam Carheden, who, collectively, provided advice and assistance on RAMS, RAMDAS, DPEAS, satellite data processing, data assimilation and proofreading this very document; the equally helpful administrative assistants Holli Knutson and Loretta Wilson for handling the non-science aspects of completing a dissertation; the entire CLEX team; and the federal government, particularly the Department of Defense Center for Geosciences/Atmospheric Research, for providing the funding for this study.

This work was supported by the DoD Center for Geosciences/Atmospheric Research under Cooperative Agreement from the Army Research Laboratory (DAAD19-02-2-0005 and W911FF-06-2-0015).

Table of Contents

ABSTRACT OF DISSERTATION	III
ACKNOWLEDGMENTS	V
TABLE OF CONTENTS	VI
1. INTRODUCTION	7
1.1 THE NATURE OF THE PROBLEM.....	9
1.2 SCIENTIFIC OBJECTIVES	19
2. OVERVIEW OF CASE STUDY	21
2.1 THE NINTH CLOUD LAYER EXPERIMENT	21
2.2 THE 2 NOVEMBER 2001 ALTOCUMULUS	22
2.3 PREVIOUS MODELING EFFORTS	28
3. EXPERIMENT SET-UP	33
3.1 REGIONAL ATMOSPHERIC MODELING DATA ASSIMILATION SYSTEM.....	33
3.2 GEOSTATIONARY OPERATIONAL ENVIRONMENTAL SATELLITES	39
3.3 METHODOLOGY	44
4. RESULTS	47
4.1 THE CONTROL: INITIAL RAMS FORWARD MODEL RUN	47
4.2 EXPERIMENT 1: GOES IMAGER	58
4.3 EXPERIMENT 2: GOES SOUNDER.....	66
4.4 EXPERIMENT 3: WATER VAPOR CHANNELS ONLY	74
4.5 THE EFFECT OF VARYING DECORRELATION LENGTHS.....	81
4.6 THE EFFECT OF CONSTRAINING SURFACE TEMPERATURE	87
5. CONCLUSIONS	93
5.1 DISCUSSION OF RESULTS	93
5.2 CONCLUSIONS	98
5.3 FUTURE WORK.....	100
6. REFERENCES	104

1. Introduction

The layered clouds of the mid-troposphere – altocumulus and altostratus, referred to generally as mid-level clouds in this work – have been termed the “forgotten clouds” (Vonder Haar et al. 1997). Although they may be associated with frontal systems or produced as outflow from deep convective storms, they rarely produce what is commonly referred to as “interesting weather”. These clouds rarely produce precipitation that reaches the ground (Gedzelman 1988). Non-frontal, non-orographic mid-level clouds are transient and difficult to forecast for numerous reasons that will be outlined below. In contrast, boundary layer stratus and stratocumulus are persistent, particularly in marine and Arctic environments, making them relatively easy targets for *in situ* field experiments. Deep convective clouds and precipitating systems are important for their effects on both human and non-human life (e.g. beneficial precipitation, deadly lightning and damaging winds) as well as energy transport through the atmosphere. Cirrus clouds have been known for their importance to climate (e.g. Stephens et al. 1990; McFarquhar et al. 2000), contributing to global warming while boundary layer stratus and deep convective clouds contribute to global cooling (Poetsch-Heffter et al. 1995). The importance of mid-level clouds on climate is not well known.

A common assumption about mid-level clouds is that they are radiatively neutral, blocking as much incoming solar radiation as outgoing infrared radiation. Mid-level clouds are typically mixed-phase, meaning they contain both liquid droplets and ice particles, to greatly varying degrees (Seaman and Vonder Haar 2003), and there are large uncertainties in their radiative properties. Numerous studies have highlighted the effect various microphysical assumptions and parameterizations have on radiative transfer modeling of mixed-phase clouds (e.g. Li and Le Treut 1992; Sun and Shine 1995; Fowler and Randall

1996; Fleishauer 2001; Yang et al. 2003; McFarquhar and Cober 2004). Mid-level clouds cover 20-25% of the Earth (Warren et al. 1986, 1988), so any small contribution to warming or cooling on a cloud-by-cloud basis may be significant when summed up over the globe.

In addition to acting as a source of uncertainty in climate modeling, mid-level clouds are important to military operations as well as civilian aviation. Mid-level clouds form between 2 and 7 km above mean sea level (MSL), which are “mission critical” altitudes (i.e. altitudes important for military operations). They routinely obscure surface targets from both aircraft and satellites, and they interfere with pilot visibility as well as laser and infrared- based communication systems (Vonder Haar et al. 1997; Seaman et al. 2005). At these altitudes, temperatures are typically between 273 K and 243 K (0 °C and -30 °C), so any liquid droplets present would be supercooled. Supercooled liquid droplets cause aircraft icing. With the recent rise in interest in using Unmanned Aircraft Systems (UAS¹, Stephens et al. 2000; MacDonald 2005) for both military and civilian applications, this icing hazard is a significant problem. UAS currently in use by the U.S. military have little to no anti-icing capabilities and are therefore grounded in the presence of supercooled liquid clouds (Ms. Pamela Clark, Army Research Laboratory, personal communication). Other lightweight aircraft with flight ceilings in this altitude range will also be affected by the icing. Altocumulus clouds are also a source of turbulence, a fact that is readily apparent to anyone who has flown through one.

Furthermore, in the author’s own experience, the unpredicted presence of mid-level clouds can lead to as much as a 5 K error in the surface temperature forecast, due to the reflection of incoming solar radiation to space. This may cause skepticism, if not contempt, from the general public regarding meteorologists and their forecasts.

¹ These were formerly known as Unmanned Aerial Vehicles, or UAVs.

The importance of improving model representation of mid-level, mixed-phase clouds, both in a short term weather forecasting sense and a long term climate modeling sense, has been introduced in the preceding paragraphs. In this work, the efforts to improve short term weather forecasts of mid-level clouds by assimilating geostationary, infrared satellite data into a mesoscale model will be presented. First, we will discuss the observed properties of non-frontal, non-orographic, mid-level, mixed-phase clouds as derived by *in situ* and remote sensing measurements and how these properties affect the ability of current forecast models to predict the formation of these clouds. We will review satellite data assimilation efforts used at operational forecast centers and how these efforts apply to cloud forecasting. Following this, the specific goals of this research will be discussed and an outline of the work will be given.

1.1 The Nature of the Problem

During Operations “Desert Storm” and “Desert Shield” in the early 1990s, it was known that mid-level clouds had significant impacts on military operations and that these clouds were very difficult to forecast (Vonder Haar et al. 1997). From this, the U.S. Department of Defense (DoD) sponsored the Cloud Layer EXperiment (CLEX), a series of field experiments designed to improve our understanding of the processes involved in the formation, sustenance and dissipation of non-frontal, non-orographic mid-level clouds. A primary goal is to use this understanding to improve mid-level cloud forecasts. These experiments used a combination of *in situ* aircraft measurements of cloud properties as well as ground-based and satellite remote sensing observations.

During the Ninth CLEX field experiment (CLEX-9), the University of Wyoming King Air research aircraft flew ten flight missions into mid-level clouds during eight days between 8 October and 4 November 2001. A rotating team of forecasters met on a daily basis to

attempt to predict the occurrence of suitable mid-level clouds on the following day so the aircraft crew and scientists responsible for data collection would be prepared for possible flights. Forecasters, of which the author was one, used a variety of operational forecast models and research models (run in operational forecast mode) including the Eta (Black 1994), Rapid Update Cycle (RUC, Benjamin et al. 2004), Navy Operational Global Atmospheric Prediction System (NOGAPS, Hogan and Rosmond 1991), European Centre for Medium-range Weather Forecasts (ECMWF, Rabier et al. 2000), Pennsylvania State University- National Center for Atmospheric Research Mesoscale Model (MM5, Barker et al. 2004) and Regional Atmospheric Modeling System (RAMS, Cotton et al. 2003). None of these models predicted the formation of any of the clouds that were sampled.

Furthermore, Illingworth et al. (2007) compared ground-based radar and lidar observations of clouds with forecasts produced by a variety of European forecast models, including the ECMWF, Deutscher Wetterdienst Lokal Modell (Doms and Schättler 2002), Royal Netherlands Meteorological Institute (KNMI) Regional Atmospheric Climate Model (Lenderink et al. 2003), UK Met Office regional and global models (Cullen 1993), Météo France ARPEGE (Courtier et al. 1991) and the Swedish Meteorological and Hydrological Institute Rossby Centre Regional Atmospheric Model (Jones et al. 2004). With the exception of the Deutscher Wetterdienst Lokal Modell, all of the models underpredicted mid-level cloud occurrence.

A review of observed mid-level cloud properties as well as properties of various forecast models provides insight as to why mid-level clouds are difficult to forecast. Aircraft observations of mid-level clouds have been reported by Hobbs and Rangno (1985, 1998), Paltridge et al. (1986), Heymsfield et al. (1991), Pinto (1998), Tulich and Vonder Haar (1998), Fleishauer et al. (2002) and Seaman and Vonder Haar (2003). Table 1.1 presents a comparison of cloud properties observed during these studies. This comparison reveals that mid-level clouds are, with a few exceptions, less than 1 km thick, have liquid water contents

(LWC) less than 0.5 g m^{-3} and exist at temperatures between $0 \text{ }^\circ\text{C}$ and $-30 \text{ }^\circ\text{C}$ (273 K and 243 K). The conceptual picture of mid-level clouds based on these studies is shown in Figure 1.1.

Table 1.1. Comparison of cloud depth, liquid water content (LWC) and temperature of mid-level clouds observed by aircraft for various field studies. The studies referenced here collectively contain direct observations of nearly 70 mid-level clouds.

<i>Field Study</i>	<i>Cloud Depth</i> [m]	<i>LWC</i> [g m ⁻³]	<i>T</i> [°C]
Continental North American			
Tulich and Vonder Haar (1998)	200-800	.03 - .31	-10 to -23
Fleishauer et al. (2002)	500-2300	.005 - .35	-1 to -31
Seaman and Vonder Haar (2003)	250-3100	.04 - .28	+2 to -25
Heymsfield et al. (1991)	200-500	.01 - .12	-29 to -31
Marine and Arctic			
Hobbs and Rangno (1985)	100-1000	< .1 - 1.3	-4.5 to -26
Hobbs and Rangno (1998)	30-800	.02 - .14	-1 to -31
Pinto (1998)	130-290	.005 - .1	-13 to -20
Continental Australian			
Paltridge et al. (1986)	300-700	.01 - 1.2	-6 to -11

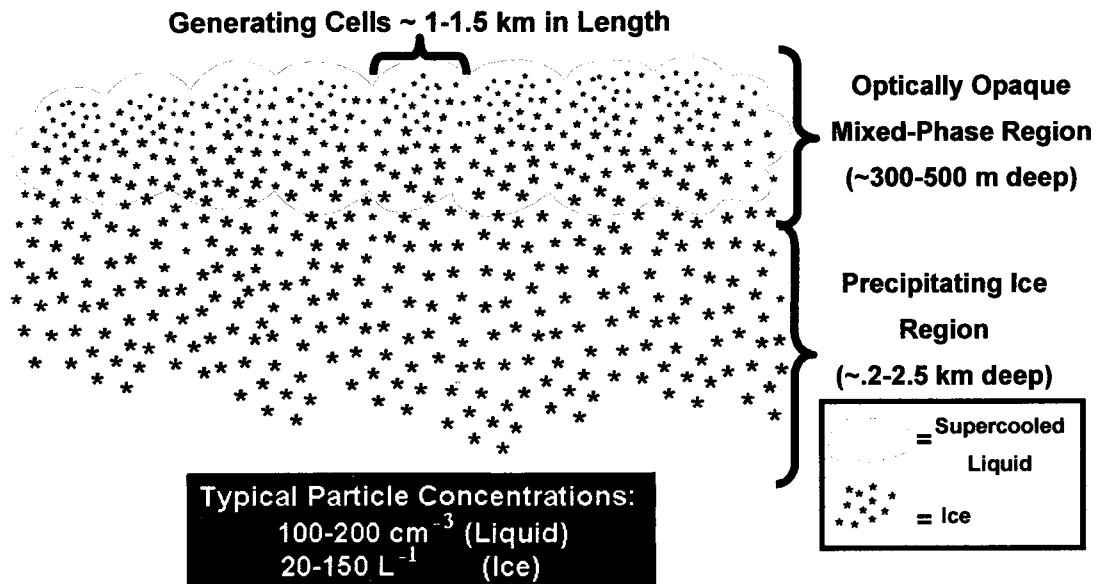


Figure 1.1. A conceptual picture of non-frontal, non-orographic, mid-level, mixed-phase clouds based on the results of CLEX (Fleishauer et al. 2002; Seaman and Vonder Haar 2003; Carey et al. 2008). This is similar to the schematic of glaciating altocumulus clouds presented in Hobbs and Rangno (1985), although the clouds observed during CLEX have been known to last up to ten hours in a mixed-phase state without glaciating.

The conceptual picture of mid-level cloud formation based on previous and on-going CLEX research is that of a humid layer in the mid-troposphere lifted to the point of condensation. The lift may come from convection, gravity waves, mountain waves, frontal boundaries or the passage of potential vorticity anomalies. Once saturation is reached, the water vapor condenses on the available cloud condensation nuclei (CCN) and ice nuclei (when present) and a cloud is formed. Any ice particles that form will scavenge the available water vapor preferentially over the liquid droplets, grow by this vapor deposition, and precipitate out of the base of the cloud. The cloud is maintained by either (or both) the large scale dynamic lift and/or by radiation-induced instability in the cloud layer, provided there is a sufficient supply of moisture. These processes are discussed in more detail in Seaman and Vonder Haar (2003).

It is not uncommon for operational forecast models to have ~500 m vertical resolution in the mid-troposphere. To highlight one example, the RUC model uses a hybrid θ - σ vertical coordinate (Figure 1.2) with a maximum pressure resolution of 15 mb in the free troposphere below 600 mb (Benjamin et al. 2004). Clearly visible in Figure 1.2 are the relatively high resolution in the boundary layer, near the tropopause, and at the boundaries of synoptic features (i.e. fronts) and the relatively poor resolution in the mid-troposphere (350 – 650 hPa). Pressure resolutions of 50 hPa – 100 hPa seen in the mid-troposphere in Figure 1.2 correspond to height resolutions of 500 m – 1000 m or more. Furthermore, the target virtual potential temperature, θ_v , values of RUC layers between 290 K and 320 K are separated by 2 K (Benjamin et al. 2004). Fleishauer et al. (2002) examined θ_v profiles of several mid-level clouds observed during CLEX-5 and found that θ_v typically varied by less than 2 K between cloud base and cloud top. These clouds all had θ_v values between 290 K and 320 K. Mid-level clouds are thus typically observed to exist at or below the resolution limit of the RUC (and other models).

The ECMWF and Global Forecast System (GFS, Kanamitsu et al. 1991) models are examples of operational forecast models that use simple, linear temperature relationships to discriminate between the liquid and ice phase for cloud particles below 0 °C. In the case of the GFS, the percentage of ice particles varies linearly with temperature such that none of the cloud particles are ice at or above 1 °C and all are ice at or below -20 °C (Figure 1.3). This is also a common assumption in general circulation models (GCM) and cloud resolving models (Smith 1990; Bower et al. 1996; Fowler and Randall 1996; Rasch and Kristjansson 1998; Zhang et al. 2003; Khairoutdinov and Randall 2003). For comparison, Heymsfield et al. (1991) and Fleishauer et al. (2002) observed supercooled liquid droplets in mid-level clouds at temperatures as low as -31 °C.

The common microphysical structure of mid-level, mixed-phase clouds is such that a layer of supercooled liquid droplets occurs at or near cloud top, from which ice particles precipitate (Figure 1.1), thus the peak LWC is near cloud top (where temperatures are the lowest) and the peak ice water content (IWC) is near cloud base (Fleishauer et al. 2002; Seaman and Vonder Haar 2003; Carey et al. 2008). Arctic boundary layer stratus and stratocumulus clouds have shown a similar microphysical structure (Pinto 1998; Lawson et al. 2001; Zuidema et al. 2005; Verlinde et al. 2007). There has been some debate on this topic. The results of Korolev et al. (2003), and the studies mentioned therein, show that the lower the temperature, the more likely the cloud is to be comprised of ice. It should be noted that clouds observed by Korolev et al. (2003) were associated with frontal systems, while those of the previously referenced studies were not. The dynamics of frontal versus non-frontal clouds may explain the differences in microphysical structures. It may also be that, in a globally averaged sense, the colder the cloud, the more likely it is to be comprised of ice due to increased activation of ice nuclei at lower temperatures (e.g. Heymsfield and Miloshevich 1993) but, on an individual cloud basis, microphysical processes favor the liquid-over-ice paradigm in layered mixed-phase clouds. This discrepancy will need to be resolved before models can rightfully be blamed for not accurately replicating the microphysical structure of all mixed-phase clouds. The impacts on simulated cloud morphology through the use of this temperature-phase relationship have been discussed in Fleishauer (2001).

Mid-level clouds are weakly forced, with vertical velocities typically less than 1 m s^{-1} (Fleishauer et al. 2002; Seaman and Vonder Haar 2003). Such small vertical velocities are difficult for models to accurately reproduce. One reason for this is that direct vertical velocity measurements are virtually non-existent. Although various dynamical equations relate vertical velocity to other atmospheric variables (i.e. horizontal winds, quasi-geostrophic vorticity, temperature advection, geopotential), accurate solution of these equations is

hampered by relatively inaccurate, infrequent or non-existent measurements of the required quantities (Holton 1992).

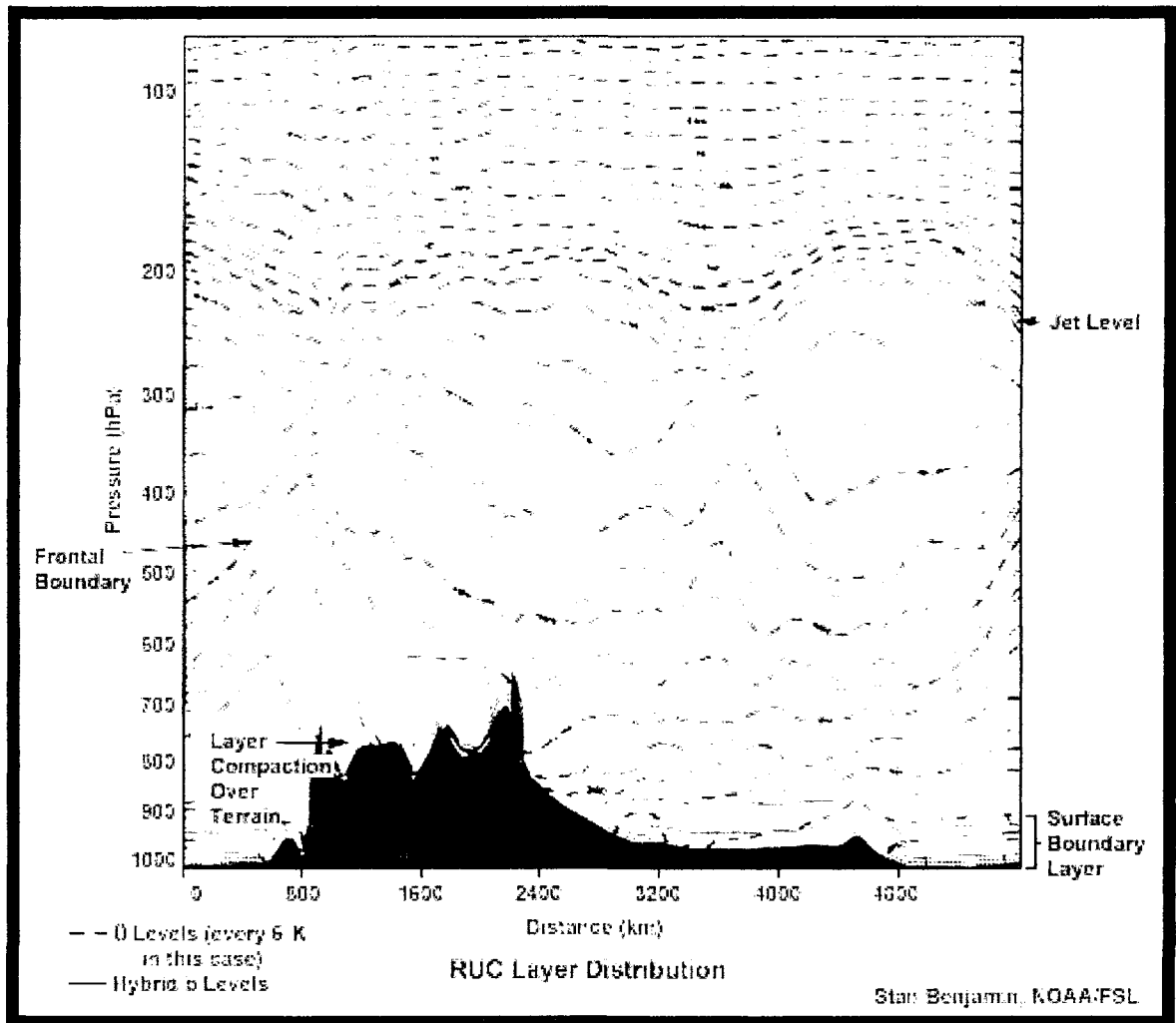


Figure 1.2. Representative distribution of the hybrid θ - σ vertical layers in the RUC model in an east-west cross-section of the United States. The black shaded region represents the land surface, with the Rocky Mountains on the left and Appalachians on the right. The actual model levels are given by the solid lines. These levels are designed to follow isentropes in the mid- and upper troposphere, given by the dashed lines, and the terrain in the lower troposphere. Mid-level clouds typically occur between 650 hPa and 350 hPa, where the resolution is the coarsest. Various features of note are labeled. Image courtesy Stan Benjamin, NOAA/FSL.

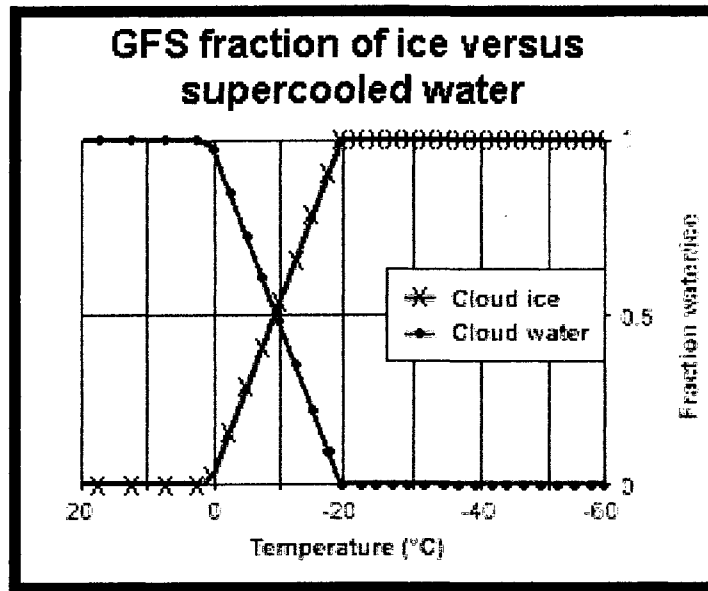


Figure 1.3. Mathematical representation of the fraction of cloud liquid water (green) and cloud ice (blue) in the GFS model as a function of temperature.

Mid-level clouds, by definition, form above the boundary layer. This means that the moisture necessary to form mid-level clouds does not come directly from the surface. It may come from the remnants of other clouds that existed in the mid-troposphere or it may be transported by favorable dynamics that carry moisture out of the boundary layer and into the mid-troposphere. Historically, the primary source of moisture data used to initialize forecast models was radiosondes. Numerous studies have shown that radiosondes have biases that lead to underestimation of relative humidity, particularly in the mid- and upper troposphere (Soden et al. 1994; Ferrare et al. 1995; Lesht and Liljegren 1997; Kley et al. 2000; Miloshevich et al. 2001; Wang et al. 2002; Turner et al. 2003; Soden et al. 2004). Additionally, it will be shown that a water vapor feature identified by satellite imagery associated with the altocumulus cloud that constitutes the focus of this work had a length scale at or below the resolution limit of the current radiosonde network. It is the hypothesis

of this work that this cloud was not forecast in part due to poor moisture initialization within the forecast model.

Satellites provide information on atmospheric humidity and many operational forecast centers have recently begun assimilating humidity- sensitive satellite observations into their models. Infrared water vapor channels have been assimilated into many regional and global models (e.g. McNally and Vespineri 1995; Garand and Hallé 1997; Ruggiero et al. 1999; McNally et al. 2000; Raymond et al. 2004; Fan and Tilley 2005). McNally and Vespineri (1995) used a one-dimensional variational assimilation technique (1-DVAR) to assimilate TOVS² radiances in cloud-free areas into the ECMWF global model. McNally et al. (2000) also assimilated TOVS radiances in cloud-free areas in the National Center for Environmental Prediction's (NCEP) Spectral Statistical Interpolation (SSI) assimilation system (Parrish and Derber 1992). Ruggiero et al. (1999) assimilated cloud-free radiances from GOES-6³ into a joint Naval Research Laboratory/Air Force Research Laboratory mesoscale model using a modified successive corrections scheme. Raymond et al. (2004) assimilated GOES water vapor in both clear and cloudy areas, using a novel procedure to account for clouds during the radiance assimilation that the authors describe as "suboptimal". Garand and Hallé (1997) assimilated retrievals of dew point depression from GOES-8 and GOES-9 using a 3-DVAR assimilation system for the Canadian Meteorological Centre. Fan and Tilley (2005) assimilated retrieved profiles of water vapor from MODIS⁴ into the MM5 mesoscale model using a 4-DVAR technique. These retrievals were performed in cloud-free areas only. The assimilation of retrievals introduces an additional source of error – namely, error in the retrieval – over direct radiance assimilation that must be accounted for. These studies have demonstrated the benefits of assimilating infrared satellite data despite the limitations of using primarily only cloud-free radiances.

² Television Infrared Observation Satellite (TIROS) Operational Vertical Sounder (Reale et al. 1986).

³ Geostationary Operational Environmental Satellite (Menzel and Purdom 1994).

Both passive and active microwave satellite sensors are sensitive to atmospheric water vapor and numerous operational forecast centers assimilate microwave data for this reason (Hoffman et al. 1990; Wu et al. 1995; Zapotocny et al. 2002; Marécal and Mahfouf 2002; Deblonde and English 2003; Benjamin et al. 2004). Operational assimilation of microwave radiances has been generally restricted to cloud free areas over the ocean, due to signal attenuation by clouds and precipitation as well as poorly known land surface emissivities, although there are recent efforts to rectify this (Marécal and Mahfouf 2002; Ruston and Vonder Haar 2004; Bauer et al. 2006; Weng et al. 2007). Recent studies have also shown a benefit to assimilating humidity information from Global Positioning System (GPS) satellites (Ha et al. 2003; Cucurull and Derber 2007; Cucurull et al. 2008), which detect an active radio wave signal whose speed is dependent on atmospheric humidity.

The limitation of assimilating satellite water vapor data in cloud-free areas is a significant one, considering that clouds cover more than half of the globe (Warren et al. 1986, 1988; Mokhov and Schlesinger 1993; Rossow and Duenñas 2004) however, this limitation is one of ease and computational efficiency. As discussed in Vukićević et al. (2006), cloudy radiance data assimilation is possible given the following considerations:

- 1) The forward model must be able to resolve cloud scale motions. Cloud resolving models typically have large state vectors with poorly quantified uncertainties and are computationally expensive.
- 2) The assimilation of satellite radiance data in cloudy scenes requires the use of a radiative transfer model of sufficient complexity to resolve the interaction of clouds and radiation on the scales needed for item 1 for the broad range of wavelengths used by environmental satellites.

⁴ MODerate resolution Imaging Spectrometer (King et al. 2003).

- 3) Temporal consistency must be maintained during the assimilation over the period of cloud evolution, given the high temporal variability of cloud properties. This requires the development and use of a full adjoint of the cloud resolving model, or another similar “smoothing data assimilation method” (van Leeuwen 2001). This is difficult to implement and is also computationally expensive.
- 4) The error statistics necessary for optimal implementation of variational assimilation techniques are not well known as cloud resolving models have not been systematically compared with satellite radiance observations.
- 5) Independent verification data are required to evaluate the accuracy of the results and to better quantify the information content of the satellite data.

The present work is based on the work of Greenwald et al. (2002, 2004) and Vukićević et al. (2004, 2006), who have addressed items 2, 3 and 5. One goal of this work is to contribute additional knowledge to item 5. The uncertainties and error statistics mentioned in items 1 and 4 are left as subjects for future research.

1.2 Scientific Objectives

This study may be considered a follow-up to the study of Vukićević et al. (2006), which examined the impacts of assimilating the GOES Imager window channels to improve model characterization of a cirrus cloud case using independent verification data. In this work, a mesoscale cloud resolving model (RAMS) is used in a 4-DVAR assimilation system for one case of an altocumulus cloud that was observed during CLEX-9. Water vapor and window channels from both GOES instruments (Imager and Sounder) are assimilated and the impacts on the model forecast are assessed. Independent verification data were gathered during CLEX-9 and are used to assess model and assimilation performance. Unlike Vukićević et al. (2006), where cloud was present in the forward model and the data were

assimilated to improve the model characterization of the cloud, this study explores the use of similar data for the case where the model had no pre-existing cloud. The ability to assimilate a cloud into the model where no cloud is present is discussed.

Three experiments have been performed: one assimilating only GOES Imager water vapor and window channels, another assimilating similar channels from GOES Sounder, and a third assimilating only the water vapor channels from both GOES Imager and Sounder – termed the water vapor-only experiment.

The goals of this study are as follows: 1) explore the use of cloudy radiance data in a cloud-free initial forward model run, 2) quantify the impact of water vapor and window channel data on the initial temperature and dew point profiles, 3) compare and contrast the impact of GOES Imager vs. GOES Sounder data for similar channels, 4) compare and contrast the impact of using only water vapor channels versus using water vapor plus window channels.

This dissertation is organized as follows. Chapter 2 presents a description of the case study used in the experiments, namely that of a long-lived, isolated, non-frontal, non-orographic altocumulus cloud. Chapter 3 discusses the experimental set-up, including a description of the satellite data used, the mesoscale cloud resolving model and the 4-DVAR assimilation system. Chapter 4 presents the results of each experiment. A review of the results and conclusions are presented in Chapter 5, along with proposed areas for future research.

2. Overview of Case Study

In this chapter, we discuss the case study of 2 November 2001: a long-lived, isolated, non-frontal, non-orographic, altocumulus cloud observed during CLEX-9. This case is an ideal subject for this work. We begin with a brief overview of the CLEX-9 field project in section 2.1. Section 2.2 discusses the properties of the observed altocumulus cloud. Finally, Section 2.3 presents the results of previous attempts to modify a forecast model to successfully forecast this cloud and provides further justification for the present work.

2.1 The Ninth Cloud Layer Experiment

As mentioned in the introduction, the Cloud Layer Experiment (CLEX) is an ongoing Department of Defense (DoD) Center for Geosciences and Atmospheric Research (CGAR) sponsored research program dedicated to understanding the processes inherent in the formation, maintenance, and dissipation of non-frontal, non-orographic, mid-level clouds. This research has allowed for investigation into the problems of satellite detection (Jones and Vonder Haar 2003), radiative transfer in mixed-phase clouds (Fleishauer 2001; Seaman and Vonder Haar 2003; Larson et al. 2007; Niu et al. 2008), as well as understanding cloud microphysics and dynamics (Tulich and Vonder Haar 1998; Larson et al. 2001; Fleishauer et al. 2002; Seaman and Vonder Haar 2003; Larson et al. 2006; Carey et al. 2008).

The ninth CLEX intensive observation period occurred between 8 October and 4 November 2001. The University of Wyoming King Air research aircraft was flown for ten flight missions on eight different days through mid-level clouds over western Nebraska and eastern Wyoming. The aircraft was outfitted with numerous microphysical and thermodynamic probes as well as a 95 GHz cloud radar (Jones and Vonder Haar 2003; Seaman and Vonder Haar 2003; Carey et al. 2008). In addition to the aircraft measurements, ground based measurements were taken from North Platte, NE (41.1 °N latitude, 100.8 °W longitude) and included the NOAA-ETL dual frequency microwave radiometer, the Colorado State University (CSU) MicroPulse Lidar, and short- and long-wave radiation instrumentation. Radiosondes were launched from North Platte, both at the National Weather Service Office (KLBF), at 00 and 12 UTC, and at the ground instrumentation site typically before and after aircraft sampling of the clouds. Geostationary and polar orbiting satellite remote sensing data was gathered when available.

2.2 The 2 November 2001 Altocumulus

A broad altocumulus cloud formed near 06:00 UTC over the tri-state point of Wyoming, Nebraska and Colorado on 2 November 2001. This cloud remained stable in a mixed-phase state until shortly after sunrise (14:16 UTC) as it advected toward south-central Nebraska, eventually dissipating by 17:00 UTC. The cloud formed in WNW flow in a region of positive vorticity advection on the boundary of a flattening ridge, which dominated the western half of the United States, and a trough over the Western Great Lakes and Upper Midwest (Figure 2.1). A large low pressure system was centered over Southern Hudson Bay/James Bay with a surface cold front extending from Southwestern Quebec to Eastern Oklahoma. A smaller mid-level trough and associated low existed off the coast of California. This was the typical

scenario for mid-level cloud formation during CLEX-9 (i.e. NW flow on the back edge of a mid-level trough/leading edge of a ridge in a region of positive vorticity advection). What made this cloud unique among CLEX-9 cases was, in part, its longevity and its isolation from other cloud systems. The isolation of this cloud relative to the other synoptic features mentioned is evident in visible satellite imagery taken shortly after sunrise (Figure 2.2).

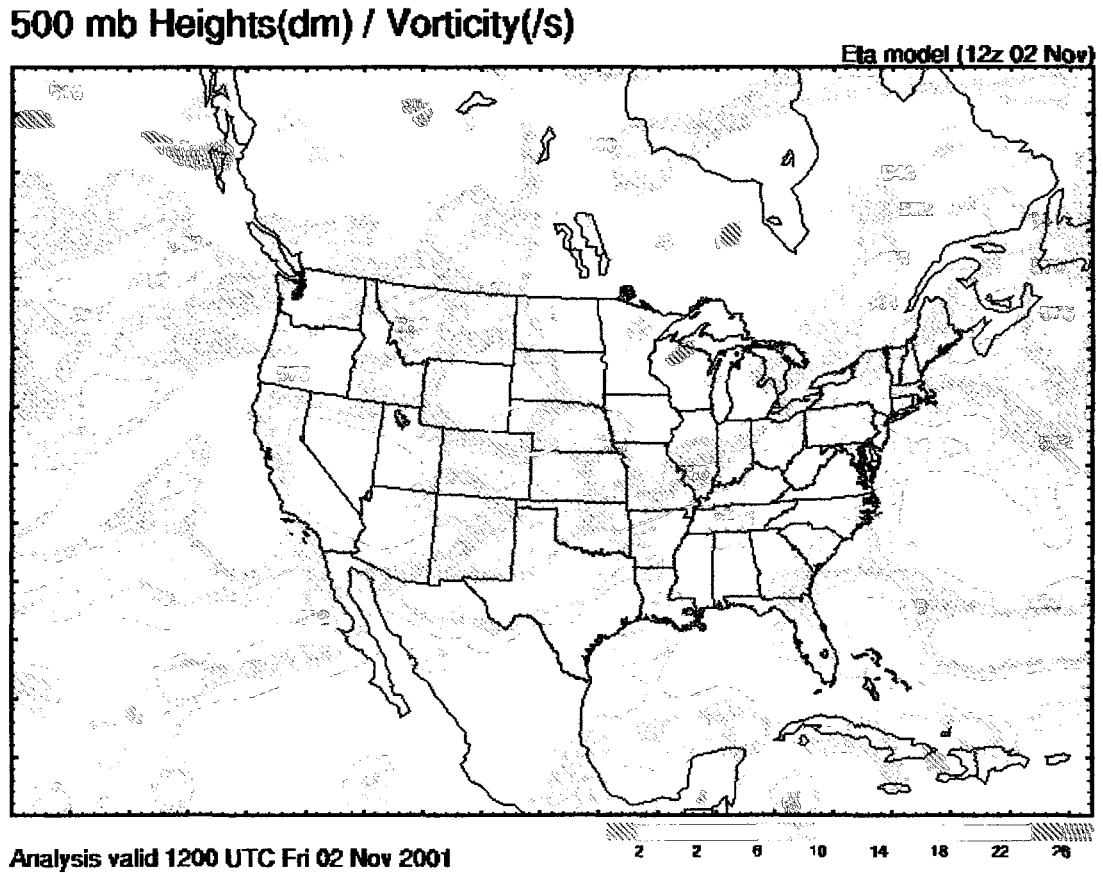


Figure 2.1. Eta model analysis of 500 hPa heights (lines) in dm and vorticity (shading) in s^{-1} for 12:00 UTC 2 November 2001. The location of the altocumulus cloud at this time is circled. Image courtesy RAP@UCAR.

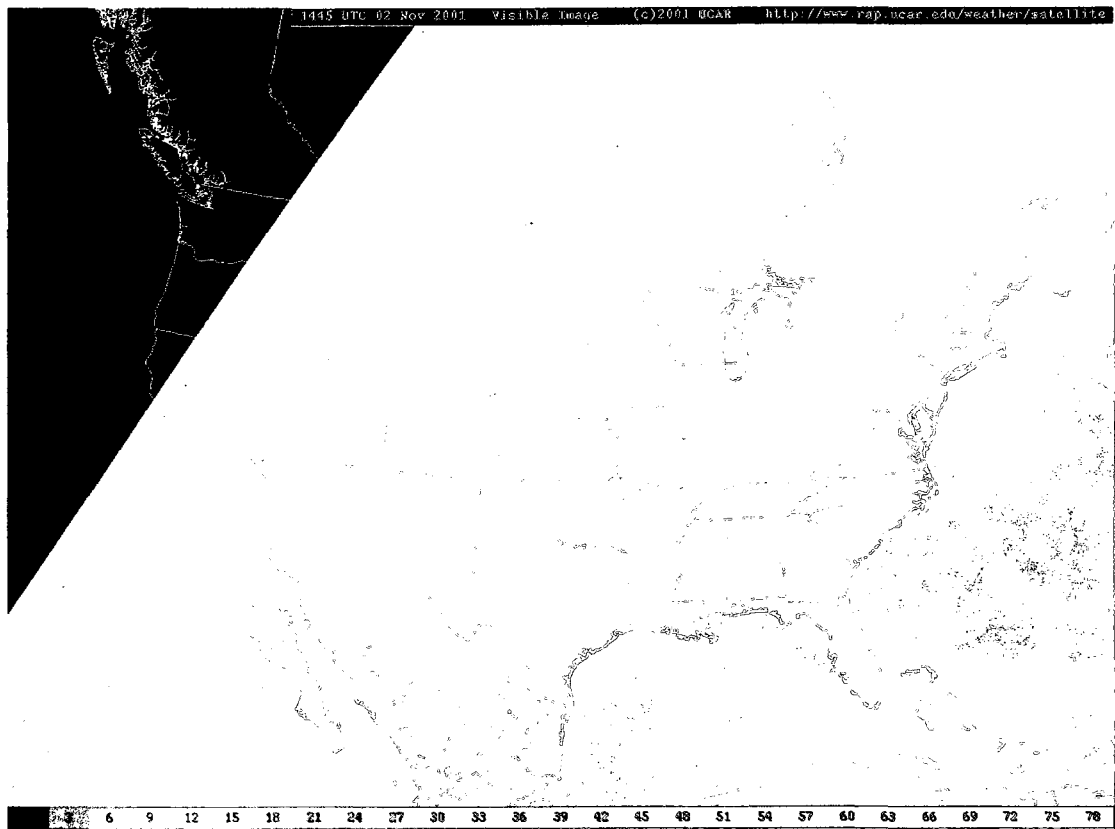


Figure 2.2. Visible satellite composite image from GOES taken at 14:45 UTC 2 November 2001. The altocumulus cloud of this study is circled. Image courtesy RAP@UCAR.

Direct aircraft observations of the cloud were made between 13:00 UTC and 16:30 UTC as the cloud transitioned from mature to dissipating following sunrise. During its mature phase, this cloud was approximately 400 km by 200 km in horizontal extent and was less than 500 m thick. Vertical profiles of the microphysical probe data indicate this cloud existed as a supercooled liquid layer that varied between 100 m and 200 m thick above precipitating ice virga that extended 200 – 300 m below the liquid layer (Carey et al. 2008). Cloud base and cloud top were 4.2 and 4.7 km MSL (550 and 600 hPa), respectively. A surface photograph taken during the dissipation stage is shown in Figure 2.3 that demonstrates the thin nature of the cloud.

Hourly infrared satellite imagery from the Imager on GOES-8 is shown for both the window (Figure 2.4) and water vapor (Figure 2.5) channels. The fact that this cloud was not

topped by overrunning cirrus makes this an ideal case to test the value of assimilating these infrared channels in a cloud resolving model since, as demonstrated in Vukićević et al. (2006), infrared window channels are primarily only sensitive to the upper-most cloud layer in a given column. Also, the lack of surrounding cloud features simplifies the dynamics that the model must reproduce. It is also worthy of note that features are evident in the water vapor imagery on a scale smaller than the current radiosonde network. The cloud itself exists in a plume of moisture of similar horizontal scale (cf. Figures 2.4 and 2.5). The nearest daily radiosonde launches occur at Omaha, NE, Dodge City, KS, Denver, CO, and Rapid City, SD – all of which are 350 - 400 km away from North Platte, NE. This highlights the need for the assimilation of water vapor measurements on smaller spatial scales, such as provided by satellites.



Figure 2.3. Photograph of the altocumulus cloud of 2 November 2001 taken at North Platte, NE at 16:48 UTC. The University of Wyoming King Air research aircraft is shown in the foreground. Image courtesy Larry Carey.

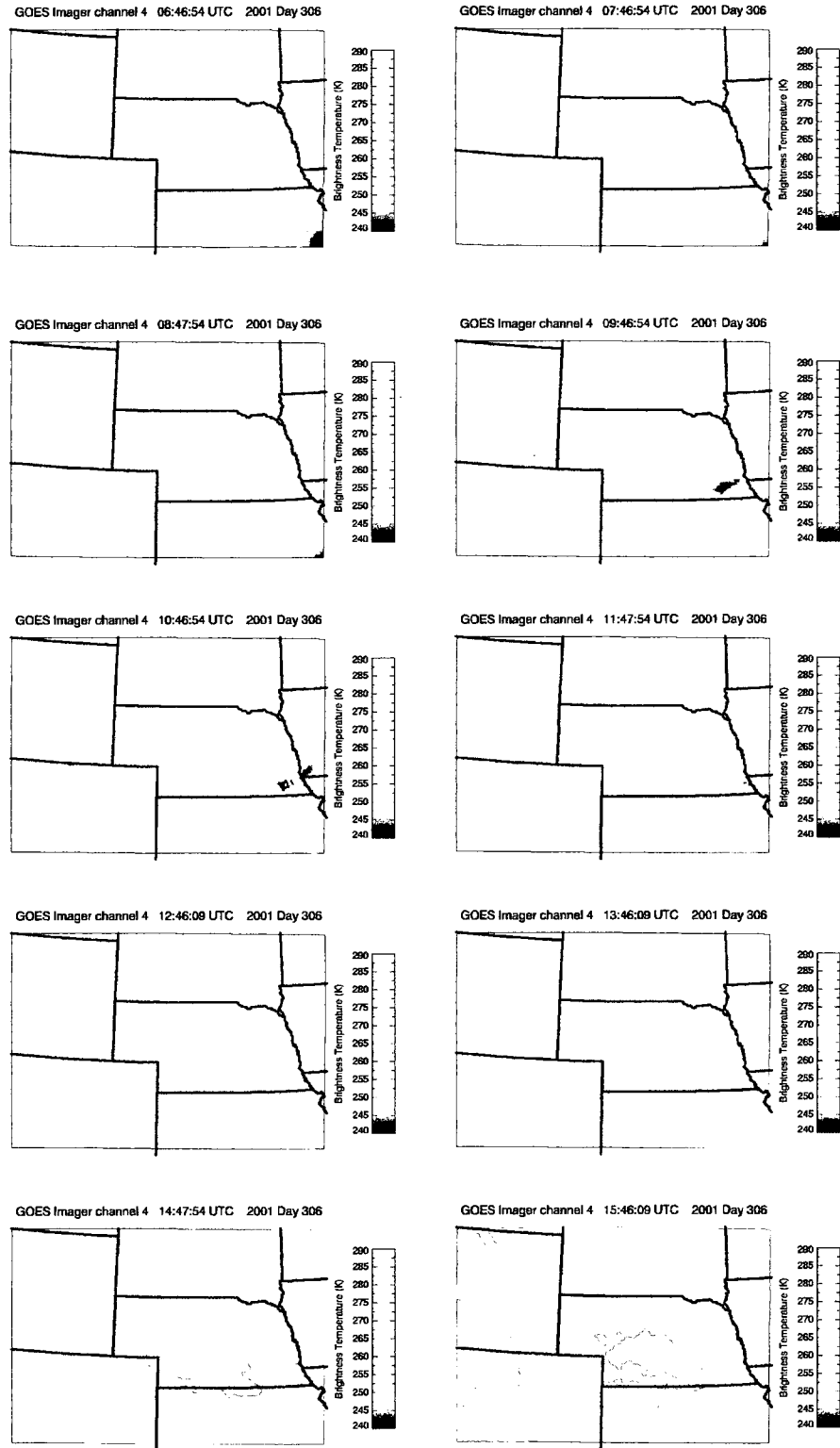


Figure 2.4. Hourly infrared satellite images from GOES-8 Imager channel 4 (window) beginning at 6:45 UTC 2 November 2001.

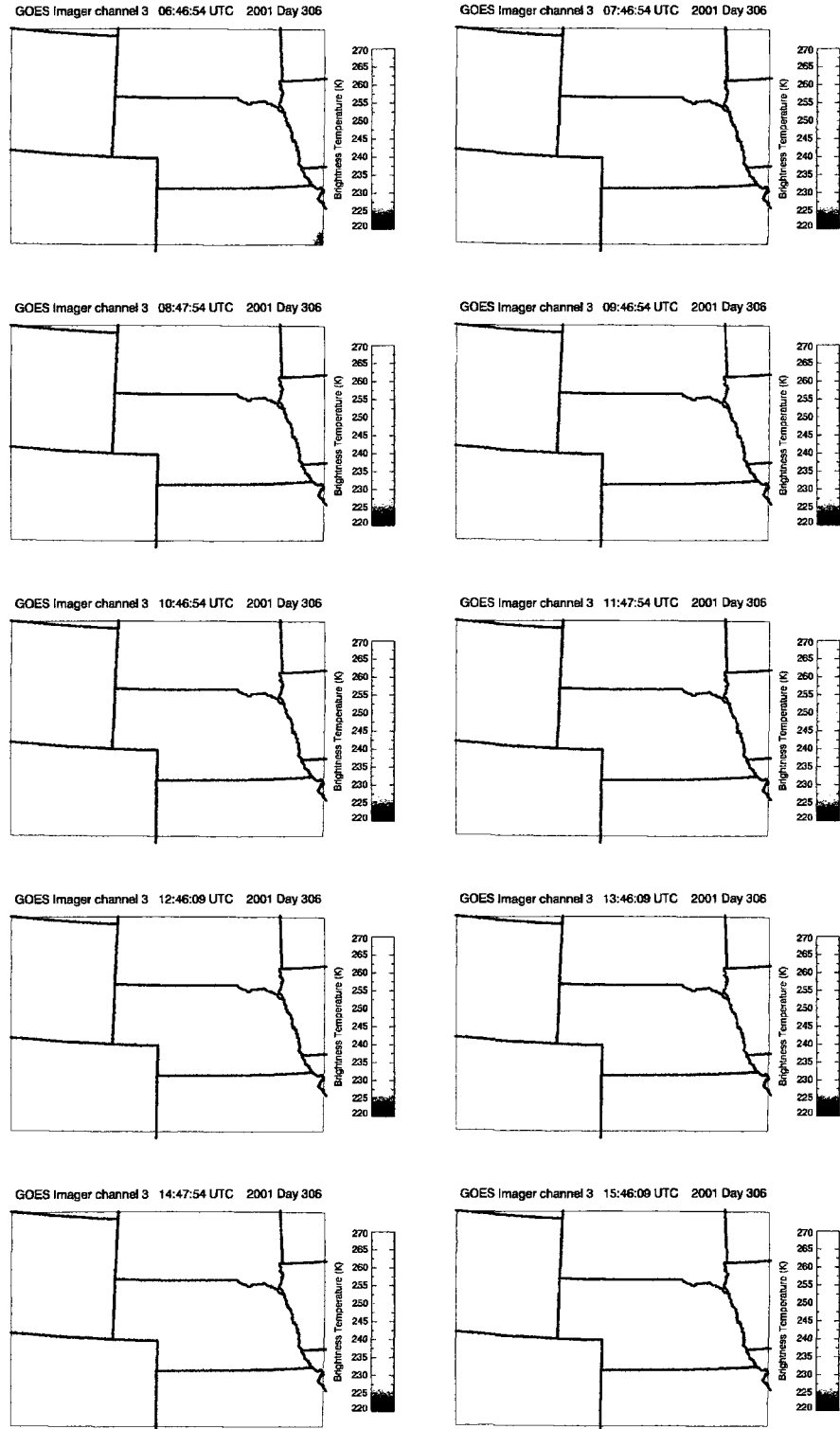


Figure 2.5. Hourly infrared satellite images from GOES-8 Imager channel 3 (water vapor) beginning at 6:45 UTC 2 November 2001. Lower temperatures correspond to higher water vapor amounts.

2.3 Previous Modeling Efforts

During CLEX-9, the RAMS model was run in operational mode to support the forecasting team. RAMS is a non-hydrostatic primitive equation model with cloud resolving capability that will be discussed in more detail in Chapter 3. Forecasts were made at 00:00 UTC and 12:00 UTC daily during the intensive observation period. The 12:00 UTC RAMS forecast relative humidity and cloud water content for 14:00 UTC 2 November 2001 are shown in Figure 2.6. It should be noted that the cloud existed over the entire domain shown in Figure 2.6 at this time, as it did at the initial model time (12:00 UTC). The model captured an elevated layer of humidity at 4 km MSL, near where the cloud actually formed, but the peak relative humidity in the layer was only 86% and no cloud formed. RAMS requires 100% relative humidity to form a cloud. It was hypothesized that RAMS failed to produce a cloud in part due to relatively poor vertical resolution in the mid-troposphere. In operational mode, the RAMS vertical resolution in the mid-troposphere is ~ 500 m, the same thickness as the cloud we are trying to forecast.

Additional model runs were performed after the conclusion of the field experiment to test the impact of increasing the vertical resolution to 100 m in the mid-troposphere. These results are shown in Figures 2.7 and 2.8. Figure 2.7 compares the forecast relative humidity at 4 km MSL with the infrared satellite imagery of the cloud at 13:00 UTC. Figure 2.8 compares the vertical profile of relative humidity vs. time with the observed backscatter from the CSU MicroPulse Lidar at North Platte, NE. The location of the relative humidity maximum in both the horizontal and vertical match very closely with the observed cloud, however, the maximum predicted relative humidity was only 85%, which, again, is too low to form a cloud. Changing the vertical resolution alone was insufficient to produce a cloud in the model.

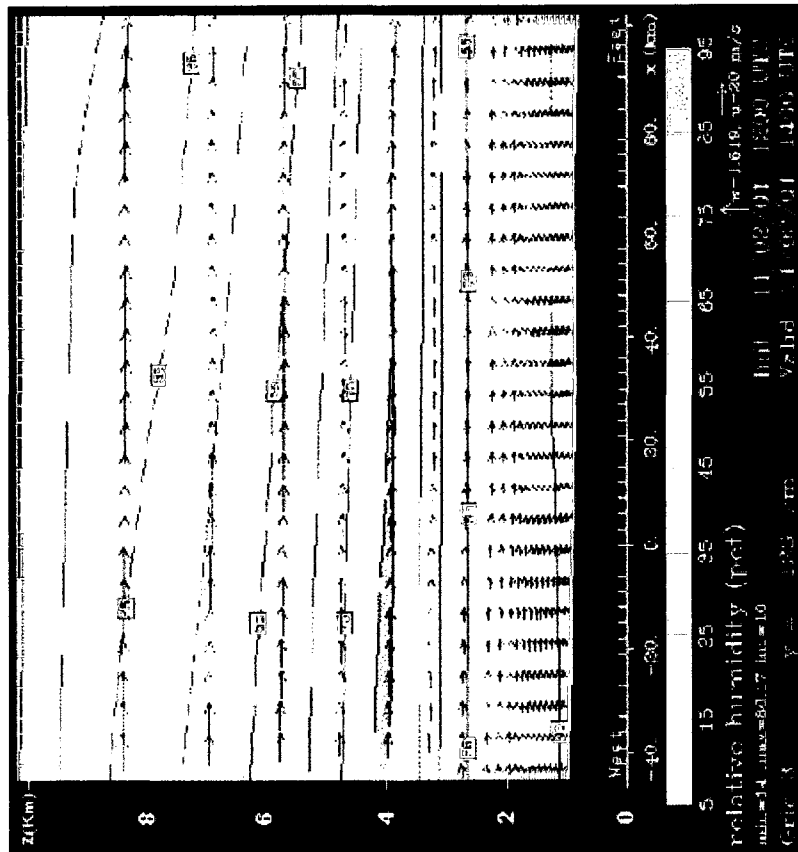
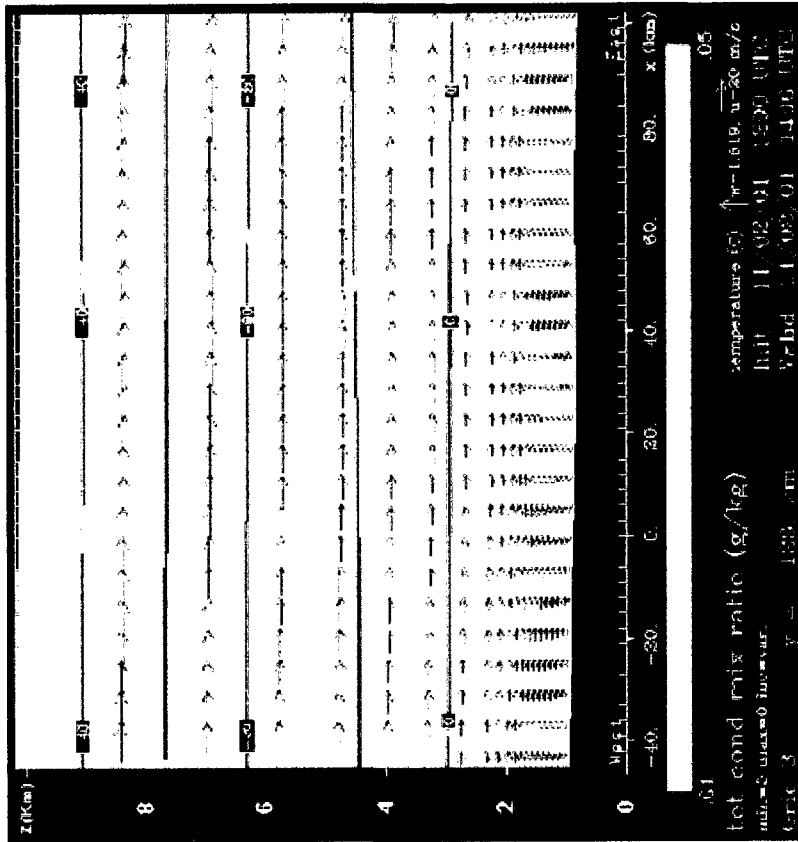
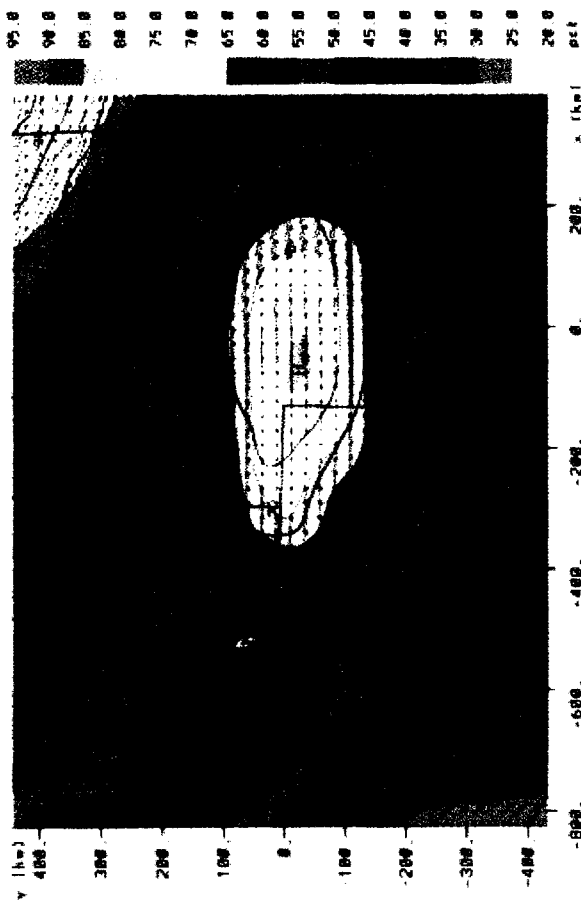


Figure 2.6. RAMS forecast relative humidity (left) and total condensate mixing ratio (right) vs. height for an east-west cross-section through North Platte valid 14:00 UTC 2 November 2001. The maximum relative humidity was 86% at 4 km MSL and no cloud condensate was present. A cloud was observed to exist between 4.2 and 4.7 km at this time.

2 Nov 2001 13 UTC RAMS Relative Humidity (%)



2 Nov 2001 13 UTC IR Satellite Image

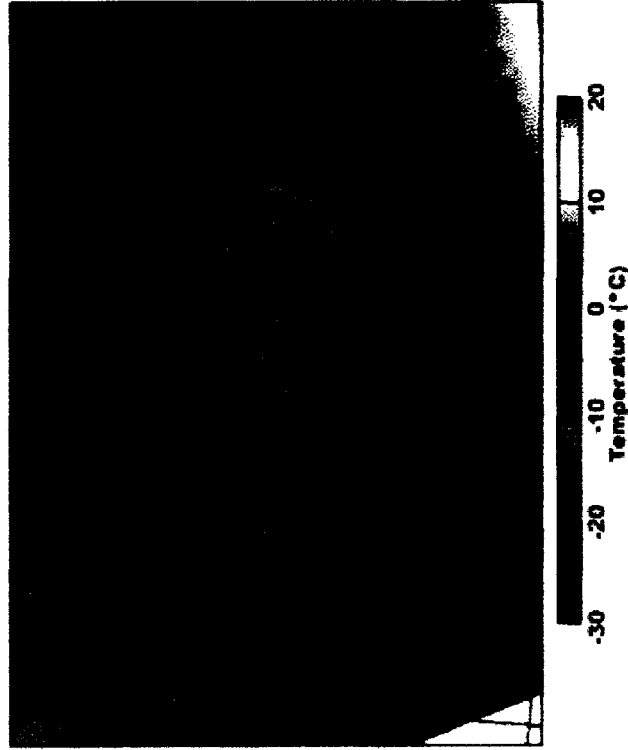


Figure 2.7. RAMS simulated relative humidity at a height of 4 km MSL (left) and observed infrared satellite image (right) taken at 13:00 UTC 2 November 2001. The humidity maximum in the model occurred in the same location as the cloud, but at 85%, was insufficient for cloud formation.

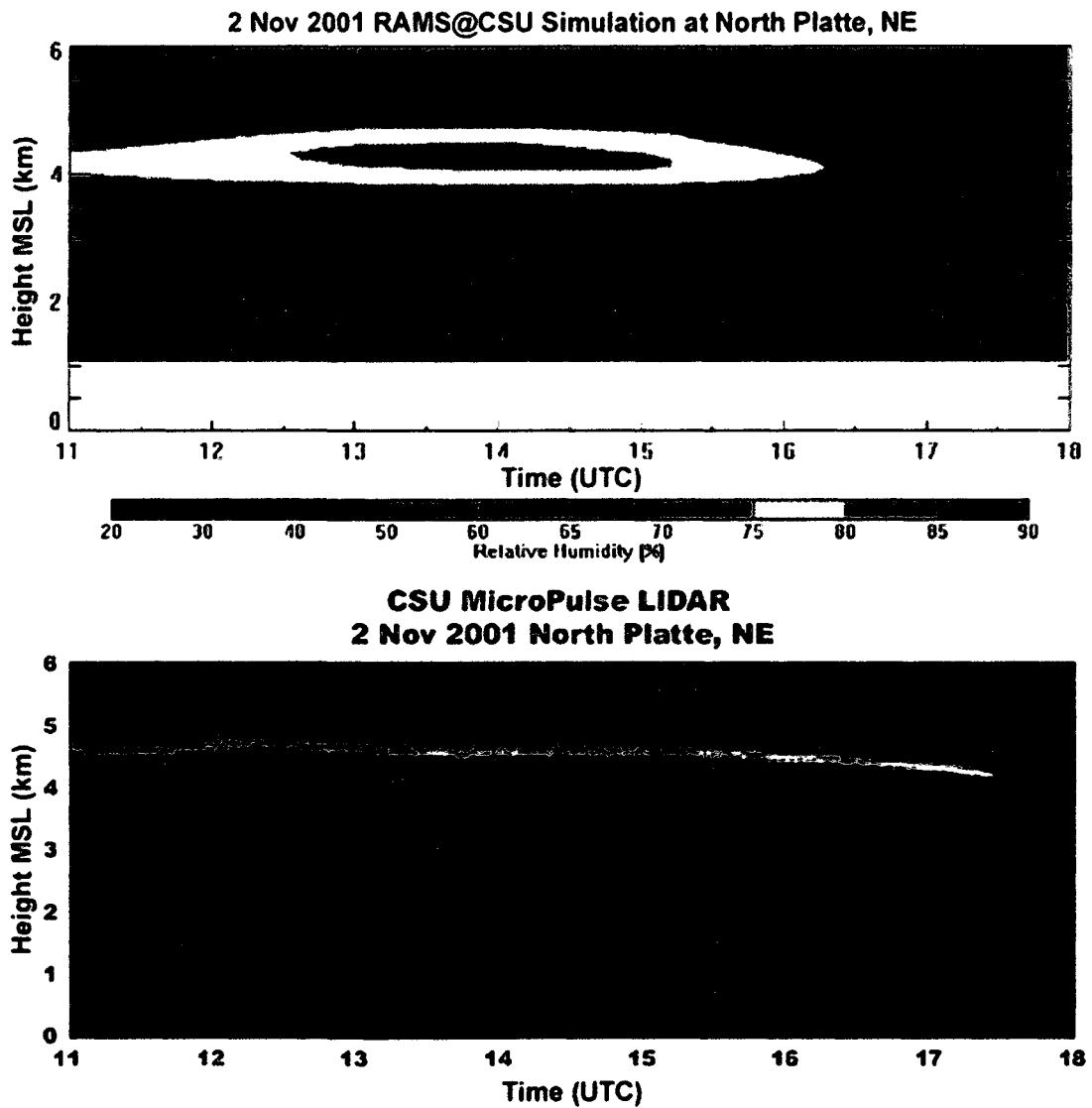


Figure 2.8. RAMS simulated relative humidity vs. height and time (top) compared with observed lidar backscatter (bottom) from the CSU MicroPulse Lidar at North Platte, 2 November 2001. The lidar return peaks at the base of the supercooled liquid layer. Vertical resolution in RAMS was 100 m in the mid-troposphere for this simulation vs. 500 m in Figure 2.6.

These results indicate that RAMS was capable of capturing the dynamics, although the moisture was insufficient to produce a cloud. It is hypothesized that assimilating moisture information from infrared satellite data would increase the humidity in the mid-troposphere and thus be sufficient for RAMS to produce a cloud in this case.

3. Experiment Set-Up

In this chapter, we provide an overview of the data assimilation system used, discuss the satellite data to be assimilated, and detail the methodology used in the experiments presented in the next chapter. The data assimilation system is presented in Section 3.1. Section 3.2 discusses the satellite data. Section 3.3 provides the methodology of the experiments presented in this work.

3.1 Regional Atmospheric Modeling Data Assimilation System

The Regional Atmospheric Modeling Data Assimilation System (RAMDAS) was recently developed at Colorado State University with a primary emphasis on the assimilation of satellite radiance data in both clear and cloudy conditions. This system utilizes a non-hydrostatic, mesoscale, cloud resolving model (RAMS) with full adjoint, a visible and infrared observational operator (VISIROO) designed to handle both clear and cloudy radiative transfer, and a computationally efficient 4-DVAR minimization algorithm. A brief overview of RAMDAS and each of its components follows. Further details of RAMDAS can be found in Zupanski et al. (2005).

RAMDAS is a “weak constraint” 4-DVAR assimilation system designed to minimize the cost function, $J(\bar{\mathbf{x}}_0)$, given by:

$$\begin{aligned}
J(\bar{\mathbf{x}}_0) = & \frac{1}{2}(\bar{\mathbf{x}}_0 - \bar{\mathbf{x}}_b)^T \mathbf{B}^{-1}(\bar{\mathbf{x}}_0 - \bar{\mathbf{x}}_b) + \frac{1}{2} \sum_t (H(M_t(\bar{\mathbf{x}}_0)) - \bar{\mathbf{y}}_t)^T \mathbf{R}_t^{-1} (H(M_t(\bar{\mathbf{x}}_0)) - \bar{\mathbf{y}}_t) \\
& + \frac{1}{2}(\bar{\mathbf{x}}_\tau - F(\bar{\mathbf{x}}_\tau))^T \mathbf{G}^{-1}(\bar{\mathbf{x}}_\tau - F(\bar{\mathbf{x}}_\tau)) + \sum_\tau \bar{\boldsymbol{\varepsilon}}_\tau^T \mathbf{E}^{-1} \bar{\boldsymbol{\varepsilon}}_\tau
\end{aligned} \tag{3.1}$$

where $\bar{\mathbf{x}}_0$ is the initial model state vector. In each term, superscript T represents a transpose. The first term in (3.1) represents the difference between the initial model state vector and the background (first guess or previous iteration) state vector, $\bar{\mathbf{x}}_b$, weighted by the inverse of the background error covariance matrix, \mathbf{B} . The second term is the sum of the differences between the model states, $M_t(\bar{\mathbf{x}}_0)$, and the observations, $\bar{\mathbf{y}}_t$, for all observation times, t , weighted by the inverse of the observation error covariance matrix, \mathbf{R}_t . The observation error covariance matrix varies with time only to allow for the possibility of assimilating different observations (satellite channels) at different times. As discussed in Section 3.3, the observation error covariance for each channel is considered time-invariant. M is the model that integrates the initial state vector $\bar{\mathbf{x}}_0$ forward to time t . H is the observational operator that maps the model state into the observation space (i.e. the radiative transfer model that converts the forward model output to brightness temperatures). The third term represents the “gravity wave penalty”, which is the weighted difference between the model state at time τ , and the model state filtered to remove high frequency variations of the control variables. F is a diabatic, nonlinear digital filter operator as in Huang and Lynch (1993). The matrix \mathbf{G} is the weighting given to the high frequency component of the control variables. The final term in (3.1) represents the model error, $\bar{\boldsymbol{\varepsilon}}$, summed over all model times, τ , weighted by the inverse of the model error covariance matrix, \mathbf{E} . Additional information about the background and observation error covariance matrices is given in Section 3.3.

In this work, the gravity wave penalty and model error terms have been neglected, simplifying the cost function to:

$$J(\bar{\mathbf{x}}_0) = \frac{1}{2}(\bar{\mathbf{x}}_0 - \bar{\mathbf{x}}_b)^T \mathbf{B}^{-1}(\bar{\mathbf{x}}_0 - \bar{\mathbf{x}}_b) + \frac{1}{2} \sum_t (H(M_t(\bar{\mathbf{x}}_0)) - \bar{\mathbf{y}}_t)^T \mathbf{R}_t^{-1} (H(M_t(\bar{\mathbf{x}}_0)) - \bar{\mathbf{y}}_t) \quad (3.2)$$

The model error was previously represented as a linear forcing for each of the prognostic variables contained in $\bar{\mathbf{x}}_0$ with temporal variability represented as a Markov process with systematic and random components (Zupanski 1997). However, Vukićević et al. (2006) concluded the following: a) this characterization of the model error produced instabilities in the model solution, b) it was unable to account for gross errors due to a lack of constraint by observations in cloudy scenes and with large lateral boundary condition errors, and c) that the results were of sufficient quality without compensating for model error. Gravity waves may be important in altocumulus dynamics (Seaman and Vonder Haar 2003), so the gravity wave penalty was left off so as to not filter them out (Zupanski et al. 2005). With this simplification, the initial model state vector is then the control variable to which the cost function is minimized.

Minimization of the cost function (3.2) is achieved by calculating the gradient of the cost function with respect to the control variable at the initial time, and finding where the gradient most closely equals zero. This gives:

$$\begin{aligned} \frac{\partial J}{\partial \bar{\mathbf{x}}_0} = \frac{\partial}{\partial \bar{\mathbf{x}}_0} \left\{ \frac{1}{2} (\bar{\mathbf{x}}_0 - \bar{\mathbf{x}}_b)^T \mathbf{B}^{-1} (\bar{\mathbf{x}}_0 - \bar{\mathbf{x}}_b) \right\} + \\ \frac{\partial}{\partial \bar{\mathbf{x}}_0} \left\{ \frac{1}{2} \sum_t (H(M_t(\bar{\mathbf{x}}_0)) - \bar{\mathbf{y}}_t)^T \mathbf{R}_t^{-1} (H(M_t(\bar{\mathbf{x}}_0)) - \bar{\mathbf{y}}_t) \right\} \approx 0 \end{aligned} \quad (3.3)$$

Since \mathbf{B} and \mathbf{R} are symmetric, the first term on the right-hand side of (3.3) becomes:

$$\frac{\partial}{\partial \bar{\mathbf{x}}_0} \left\{ \frac{1}{2} (\bar{\mathbf{x}}_0 - \bar{\mathbf{x}}_b)^T \mathbf{B}^{-1} (\bar{\mathbf{x}}_0 - \bar{\mathbf{x}}_b) \right\} = \mathbf{B}^{-1} (\bar{\mathbf{x}}_0 - \bar{\mathbf{x}}_b) \quad (3.4)$$

The second term on the right-hand side of (3.3), similar to (3.4), becomes:

$$\begin{aligned} \frac{\partial}{\partial \bar{\mathbf{x}}_0} \left\{ \frac{1}{2} \sum_t (H(M_t(\bar{\mathbf{x}}_0)) - \bar{\mathbf{y}}_t)^T \mathbf{R}_t^{-1} (H(M_t(\bar{\mathbf{x}}_0)) - \bar{\mathbf{y}}_t) \right\} = \\ \sum_t \frac{\partial (H(M_t(\bar{\mathbf{x}}_0)) - \bar{\mathbf{y}}_t)}{\partial \bar{\mathbf{x}}_0} \mathbf{R}_t^{-1} (H(M_t(\bar{\mathbf{x}}_0)) - \bar{\mathbf{y}}_t) \end{aligned} \quad (3.5)$$

Since the observations are independent of the control variable,

$$\frac{\partial (H(M(\bar{\mathbf{x}}_0)) - \bar{\mathbf{y}})}{\partial \bar{\mathbf{x}}_0} = \frac{\partial H}{\partial M(\bar{\mathbf{x}}_0)} \frac{\partial M}{\partial \bar{\mathbf{x}}_0} = \mathbf{H}\mathbf{M} \quad (3.6)$$

where $\mathbf{H} = \frac{\partial H}{\partial M(\bar{\mathbf{x}}_0)}$ represents the tangent linear model of the observational operator and

$\mathbf{M} = \frac{\partial M}{\partial \bar{\mathbf{x}}_0}$ represents the tangent linear model of the forward model. Substitution of (3.6) into

(3.5) yields:

$$\begin{aligned} \frac{\partial}{\partial \bar{\mathbf{x}}_0} \left\{ \frac{1}{2} \sum_t (H(M_t(\bar{\mathbf{x}}_0)) - \bar{\mathbf{y}}_t)^T \mathbf{R}_t^{-1} (H(M_t(\bar{\mathbf{x}}_0)) - \bar{\mathbf{y}}_t) \right\} \\ = \sum_t \mathbf{M}^T \mathbf{H}^T \mathbf{R}_t^{-1} (H(M_t(\bar{\mathbf{x}}_0)) - \bar{\mathbf{y}}_t) \end{aligned} \quad (3.7)$$

Substitution of (3.4) and (3.7) into (3.3) gives:

$$\frac{\partial J}{\partial \bar{\mathbf{x}}_0} = \mathbf{B}^{-1}(\bar{\mathbf{x}}_0 - \bar{\mathbf{x}}_b) + \sum_t \mathbf{M}^T \mathbf{H}^T \mathbf{R}_t^{-1} (H(M_t(\bar{\mathbf{x}}_0)) - \bar{\mathbf{y}}_t) \approx 0 \quad (3.8)$$

There is no analytical solution for finding the initial model state vector that solves (3.8). The solution must be estimated by searching the gradient defined by (3.8) in control variable space using an iterative algorithm (e.g. Kalnay 2003). RAMDAS uses the limited memory quasi-Newton algorithm of Nocedal (1980). For faster convergence of the minimization, a Hessian preconditioning algorithm is used (Zupanski 1993, 1996; Zupanski et al. 2005). The preconditioning algorithm utilizes a change of variable, which transforms the control variable

into a minimization subspace in which the cost function is more “spherical”, thus allowing the minimization algorithm to come closer to the center of the cost function minimum after each iteration. The minimization algorithm stops when either the change in cost function between iterations is sufficiently small (convergence) or the maximum number of iterations has been achieved. Convergence monitoring and the restart procedure are based on the angle test of Shanno (1985).

A schematic of RAMDAS is presented in Figure 3.1. The forward numerical weather prediction (NWP) model (M in equation 3.8) is RAMS, a well-documented and oft-used non-hydrostatic, primitive equation model (Tripoli and Cotton 1982; Pielke et al. 1992; Cotton et al. 2003). Clouds and precipitation are explicitly represented by a microphysical parameterization that utilizes a one-moment cloud liquid water scheme (Walko et al. 1995) and a two-moment rain and ice particle (snow, hail, graupel, pristine ice and aggregates) scheme (Meyers et al. 1997). RAMS is coupled with the Land Ecosystem Atmosphere Feedback model (LEAF-2; Walko et al. 2000), which accounts for feedbacks between the atmosphere and the surface soil and vegetation. Radiative fluxes are parameterized using the two-stream approach developed by Harrington (1997).

RAMDAS utilizes version 4.2.9 of the RAMS code, which has been “frozen” for the development of a full RAMS adjoint. The adjoint (the transpose of the tangent linear model, M^T in equation 3.8) is an adjoint of the true tangent linear model of the RAMS discrete algorithm – including moist physics and microphysical processes – except that radiative and convective parameterizations have not been included. The effects of radiation are assumed to be of secondary importance over the short time scales of RAMDAS assimilation experiments, and the convective parameterization is not needed at the spatial resolution used for cloudy scene data assimilation, where cloud processes can be explicitly resolved. An adjoint of the LEAF-2 model is included. Additional details of the RAMS adjoint are discussed in Zupanski et al. (2005).

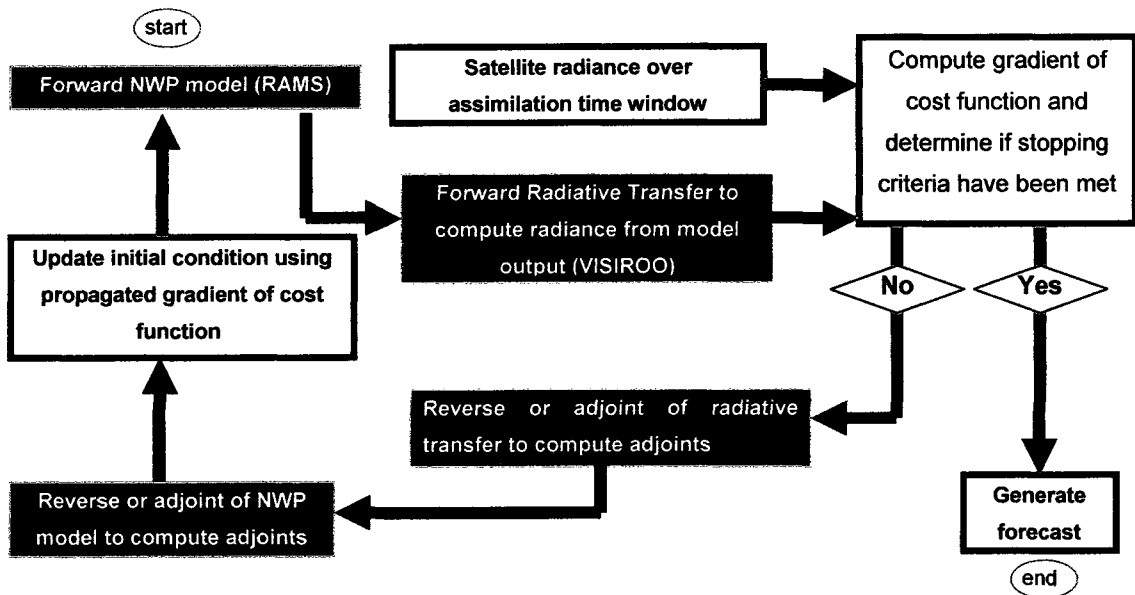


Figure 3.1. Schematic of the RAMDAS algorithm. RAMDAS begins in the upper-left with the forward numerical weather prediction (NWP) model run (RAMS). The forward model output is converted to radiance via the operational operator (VISIROO), which is then compared to the satellite observations. The cost function and its gradients are calculated. The adjoints calculate the sensitivities of the model radiances to the control variables, which are then used to update the initial conditions of the forward model for the next iteration to minimize the cost function. When the change in the cost function value is small enough, the system exits with a final forecast based on these updated initial conditions.

The visible and infrared observational operator (VISIROO) and its adjoint (H and H^T in equation 3.8, respectively) consist of two radiative transfer models that convert the RAMS output to radiance at the wavelengths of the satellite observations. For visible wavelengths, VISIROO utilizes the Spherical Harmonic Discrete Ordinate Method (SHDOM, Evans 1998). For infrared wavelengths, VISIROO uses a delta-Eddington approach (Deeter and Evans 1998). Both of these models consider multiple scattering and assume a plane parallel atmosphere. Anomalous diffraction theory (Bryant and Latimer 1969) is also used to estimate single scattering properties for all types of cloud and precipitation particles

predicted by RAMS. Gaseous extinction is calculated using the Optical Path Transmittance (OPTRAN) method (McMillin et al. 1995).

The adjoint of the observational operator is based on the assumption of linearity within the forward radiative transfer models, which was found to hold for infrared wavelengths, but not for visible wavelengths (Greenwald et al. 2004). The visible channels of GOES are not used in this study. The observational operator and its adjoint are discussed in more detail in Greenwald et al. (2002) and Greenwald et al. (2004).

3.2 Geostationary Operational Environmental Satellites

The data assimilated in this work comes from Geostationary Operational Environmental Satellites (GOES), specifically GOES-8⁵. GOES have been in use since 1975 for their ability to observe weather systems on a hemispheric scale, which has greatly improved weather analysis and forecasting, as well as our understanding of atmospheric motions. GOES-8 introduced two instruments, Imager and Sounder, which are utilized in this study. These instruments are discussed in detail in Menzel and Purdom (1994). A brief overview follows.

The Imager instrument takes images in five spectral bands (channels) in the visible and infrared range (Table 3.1), with a spatial resolution of 8 km or higher and a temporal resolution of 15 min. In this study, we assimilate data from channels 3 and 4. Channel 3 (6.7 μm) is sensitive to upper-tropospheric water vapor. Channel 4 (10.7 μm) is an infrared window channel sensitive to surface and/or cloud top temperature. Images of channel 3 and 4 for the 2 November 2001 case study have been shown in Figures 2.4 and 2.5.

Table 3.1. Properties of the GOES Imager channels. From Menzel and Purdom (1994).

Channel	Central Wavelength [μm]	Spatial Resolution [km]	Atmospheric Constituent Response / Purpose
1	0.63	1	window / view clouds and surface
2	3.9	4	window / liquid and ice discrimination
3	6.7	8	H ₂ O / upper-tropospheric water vapor
4	10.7	4	window / surface, cloud-top temperature
5	12.0	4	window, H ₂ O / temperature and humidity

The Sounder instrument takes images in 19 spectral bands (channels) in the visible and infrared range (Table 3.2), with a spatial resolution of 8 km for each channel and a temporal resolution of one hour. Combinations of channels provide soundings of atmospheric water vapor and temperature (e.g. Ma et al. 1999), however, in this work, we use the images rather than retrieved profiles. As with the Imager, we use an infrared window channel (channel 7, 12.02 μm) and a water vapor channel (channel 11, 7.02 μm). Of the three water vapor channels on the Sounder (Table 3.2), channel 11 was selected because it has the highest sensitivity to water vapor between 4 and 7 km MSL (Koyama et al. 2006), the mid-level cloud range. Channel 7 has sensitivity to lower tropospheric humidity in addition to temperature, which is evident in Figure 3.2 when compared with Figure 2.4. Figure 3.3 shows hourly images of mid-troposphere water vapor from channel 11 for the 2 November 2001 case study.

⁵ GOES-8 was also known as GOES-I or GOES-East (prior to the launch of GOES-12 in 2001).

Table 3.2. Properties of the GOES Sounder channels. From Menzel and Purdom (1994).

<i>Channel</i>	<i>Central Wavelength [μm]</i>	<i>Atmospheric Constituent Response</i>	<i>Purpose</i>
1	14.71	CO₂	stratospheric temperature
2	14.37	CO₂	upper-tropospheric temperature
3	14.06	CO₂	upper-tropospheric temperature
4	13.96	CO₂	mid-tropospheric temperature
5	13.37	CO₂	lower-tropospheric temperature
6	12.66	H₂O	total column water vapor
7	12.02	window	surface temperature and humidity
8	11.08	window	surface temperature
9	9.71	O₃	total ozone
10	7.43	H₂O	lower-tropospheric humidity
11	7.02	H₂O	mid-tropospheric humidity
12	6.51	H₂O	upper-tropospheric humidity
13	4.57	CO₂	lower-tropospheric temperature
14	4.52	CO₂	mid-tropospheric temperature
15	4.45	CO₂	upper-tropospheric temperature
16	4.13	N₂	boundary layer temperature
17	3.98	window	surface temperature
18	3.74	window	surface temperature and humidity
19	0.70	window	view surface and clouds

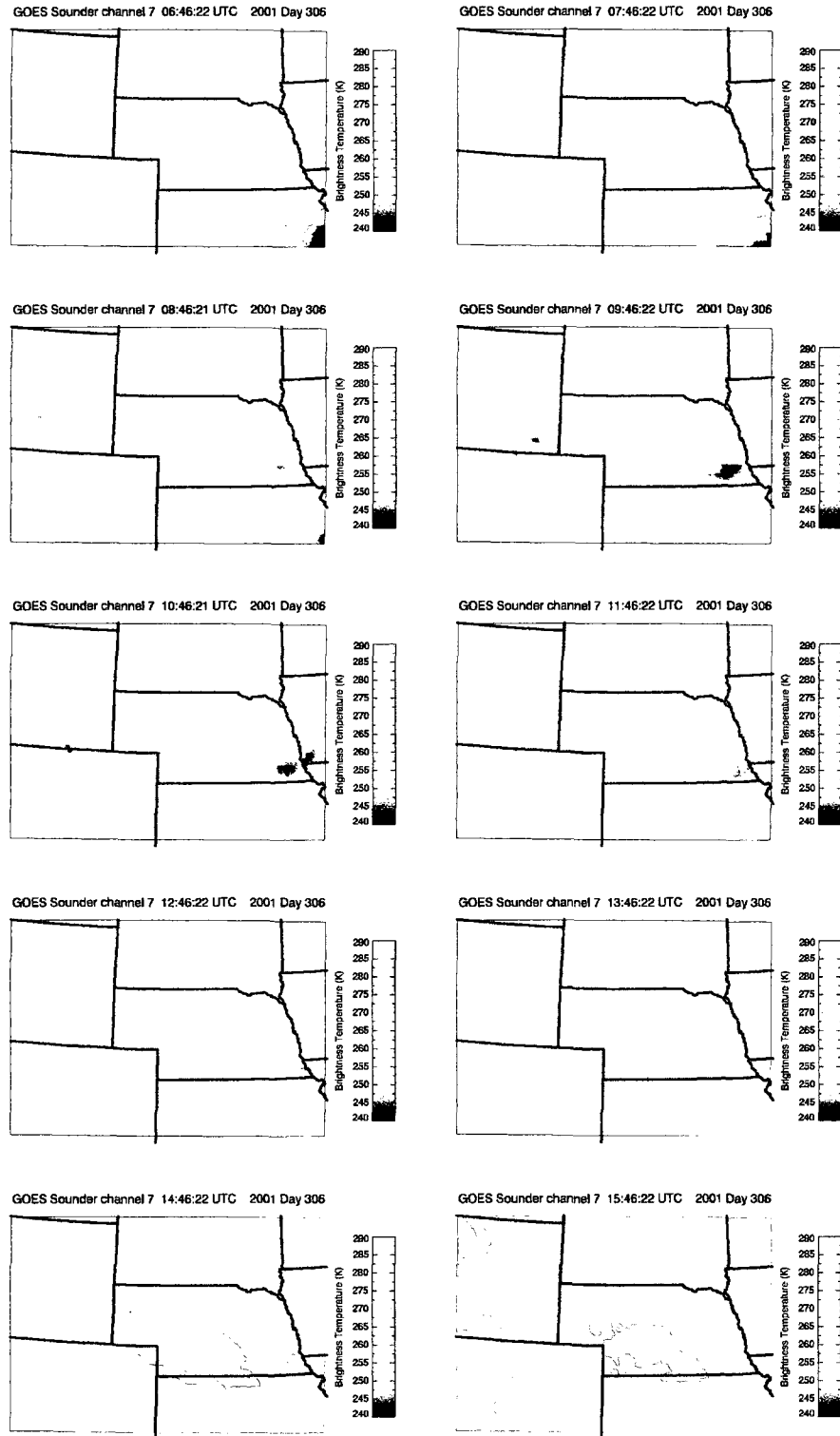


Figure 3.2. Hourly images from GOES-8 Sounder channel 7 (window) beginning at 6:45 UTC 2 November 2001. Note the “surface” does not rise to the same temperature after sunrise as GOES Imager channel 4 (Figure 2.4), due to the contribution of lower tropospheric humidity.

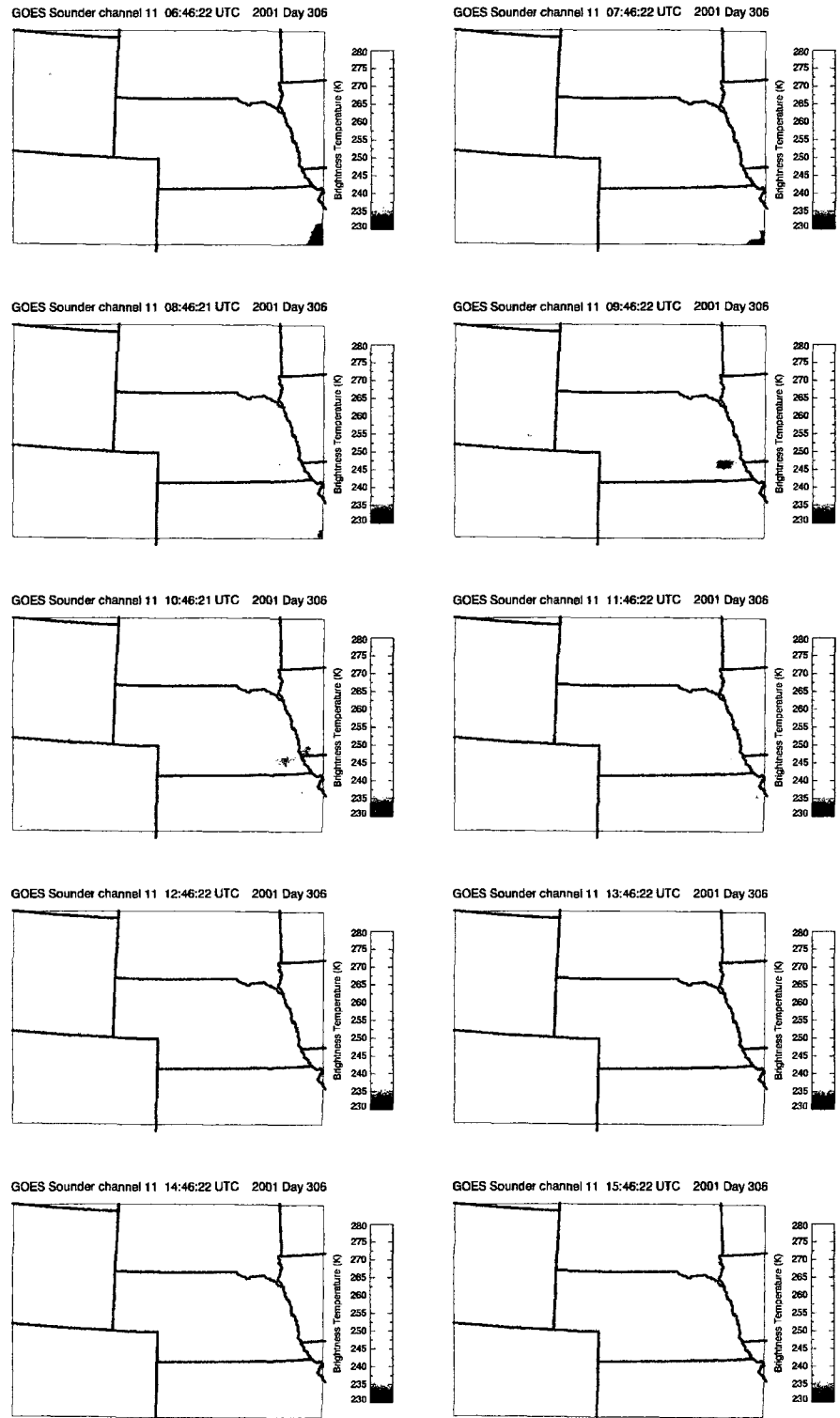


Figure 3.3. Hourly images from GOES-8 Sounder channel 11 (mid-tropospheric water vapor) beginning at 6:45 UTC 2 November 2001. Note: There is a difference in temperature scales between this figure and Figure 2.5.

3.3 Methodology

The previous sections presented an overview of the data and the data assimilation system. The specifics of how these will be implemented in the experiments presented in the next chapter will now be discussed.

A 75 x 75 (horizontal) x 84 (vertical) grid was set up in RAMS, centered on North Platte, NE (Figure 3.4) for the 2 November 2001 case study. Horizontal grid spacing is 6 km, which is near the lower limit for resolving cloud processes (Khairoutdinov and Randall 2003). Vertical levels were determined using a stretched-z grid, beginning at 50 m for the lowest level, increasing by 3% per level, and capped at 1000 m in the stratosphere. Vertical resolution at the height of the aircraft-observed cloud is approximately 150 m, which is just sufficient to resolve a 500 m thick cloud. The total volume of the domain is 450 km x 450 km x 18 km.

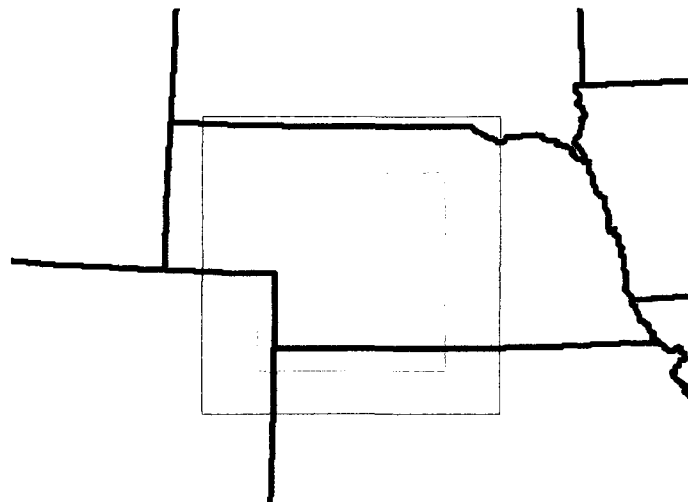


Figure 3.4. Location and size of the forward/adjoint model grid. The shaded region represents the portion of the grid excluded from the cost function calculation and, hence, is not modified by the assimilation. The background image is that of the 11:45 UTC image from GOES-8 Sounder channel 7, indicating that the cloud dominates the domain at this time.

Lateral boundary condition errors are particularly large in cloudy-scene data assimilation and have a tendency to dominate the total cost. Therefore, as in Vukićević et al. (2006), the lateral boundaries have been masked out of the cost function calculation (Figure 3.4). The cost function is calculated (and the initial conditions updated) only on the 50 x 50 domain at the center of the grid, while the forward model and its adjoint are integrated over the entire 75 x 75 domain.

The satellite data were processed and remapped to the RAMS grid using the Data Processing and Error Analysis System (DPEAS, Jones and Vonder Haar 2002). The observation error covariance matrix, \mathbf{R} , is assumed diagonal with a time-invariant standard deviation set at 2.5 K for each channel. This value was chosen so as to roughly account for both measurement and representativeness errors (Cohn 1997). It is thus assumed that measurement errors in each channel are not cross-correlated.

The background error covariance matrix, \mathbf{B} , was developed by Zupanski et al. (2002, 2005). This error is modeled using a spatial, unimodal correlation method and depends on horizontal and vertical decorrelation lengths, and variance, which are assumed time-invariant. These quantities are not well known in cloud resolving data assimilation. The variances can be (and are in this work) reasonably assumed values based on expected relative error amplitude (e.g. 50% of an average value in a particular vertical layer) as in Vukićević et al. (2006). The decorrelation lengths were varied and the impacts on the results will be discussed in the next chapter. It is believed that, while not necessarily optimal, these values are a reasonable first guess.

In each of the experiments presented in the next chapter, the RAMS model was initialized with the Final Run (FNL) of the Global Data Assimilation System (GDAS) reanalysis (Stunder 1997) beginning at 00:00 UTC 2 November 2001. RAMS was run out to 18:00 UTC, the time by which the cloud had dissipated. The RAMS output at 11:00 UTC from this run was used to initialize the RAMDAS experiments. RAMDAS was then set up to

assimilate the 11:45 UTC observations from the GOES Imager and/or Sounder. Thus, the 11:00 UTC model state was modified through the assimilation system so that the forecast 11:45 UTC model state produced brightness temperatures closest to the observations. This time configuration was chosen due to the location of the cloud over the center of the domain, and the availability of verification data (i.e. ground based remote sensing observations [Figure 2.8] and 12:00 UTC KLBF radiosonde sounding).

4. Results

In this chapter, we present and discuss the results of the experiments performed to test the usefulness of assimilating cloudy scene infrared window and water vapor channels for mid-level cloud forecasting. We begin in Section 4.1 by discussing the results of the initial forward model run (i.e. before any data has been assimilated). The usefulness of assimilating these data is then determined by comparing the results of each experiment with this initial model run, as well as comparing to the independent verification data mentioned in Chapter 2. The first experiment – the assimilation of GOES Imager channels 3 & 4 – is presented in Section 4.2. The second experiment – assimilation of GOES Sounder channels 7 & 11 – is presented in Section 4.3. The third and final experiment – assimilation of GOES Imager channel 3 and GOES Sounder channel 11, termed the water vapor-only experiment – is presented in Section 4.4. The effect of changing the decorrelation lengths used in the background error covariance matrices on the results of these experiments will be discussed in Section 4.5. Section 4.6 explores the effect of constraining the surface temperature.

4.1 The Control: Initial RAMS Forward Model Run

As discussed in the previous chapter, a RAMS simulation was initialized using the 00:00 UTC 2 November 2001 analysis from the FNL reanalysis archive. This simulation was run out to 18:00 UTC, covering the period during which the observed cloud existed, although it

should be noted the cloud did not exist within the specified domain the entire time. The results of this simulation at 11:00 UTC were then used to initialize each of the data assimilation experiments presented in the next four sections. In this section, we examine the results of this simulation as compared with the available observations. This provides insight into how well the model, without any data assimilated, handled the 2 November 2001 case. These results act as the scientific control to which the impacts of assimilating the satellite data will be assessed.

With no data assimilated, it is clear that the model alone is unable to replicate the cloud that was observed. Figure 4.1 shows vertical (X-Z) cross-sections⁶ of RAMS-simulated relative humidity at the latitude of North Platte at one-hour intervals from the beginning of the simulation. The reanalysis captures a layer of elevated humidity between 1 and 3 km above ground level (AGL) at 00:00 UTC (2 – 4 km MSL). The layer of elevated humidity is roughly one kilometer lower than where the cloud actually formed (Figure 2.8), and the peak relative humidity in the layer is only 66%, much too low to form a cloud. During the first two hours of the simulation, ascent in the lower troposphere increases the relative humidity in the layer (Figure 4.2), but only up to a maximum of 72%. Near 02:00 UTC, the vertical velocity becomes negative as subsidence begins to dominate the troposphere, and the layer of high relative humidity begins eroding away. By 11:00 UTC, the time at which the assimilation experiments were initialized, the relative humidity between 1 and 3 km AGL is less than 40%.

Relative humidity is a function of temperature and water vapor amount (which is measured by the dew point). A comparison of the 12:00 UTC model temperature and dew point sounding and the observed sounding from the National Weather Service

⁶ In this work, as with RAMS convention, “X” refers to the east-west direction (longitude), “Y” refers to the north-south direction (latitude) and “Z” refers to the vertical (height or pressure).

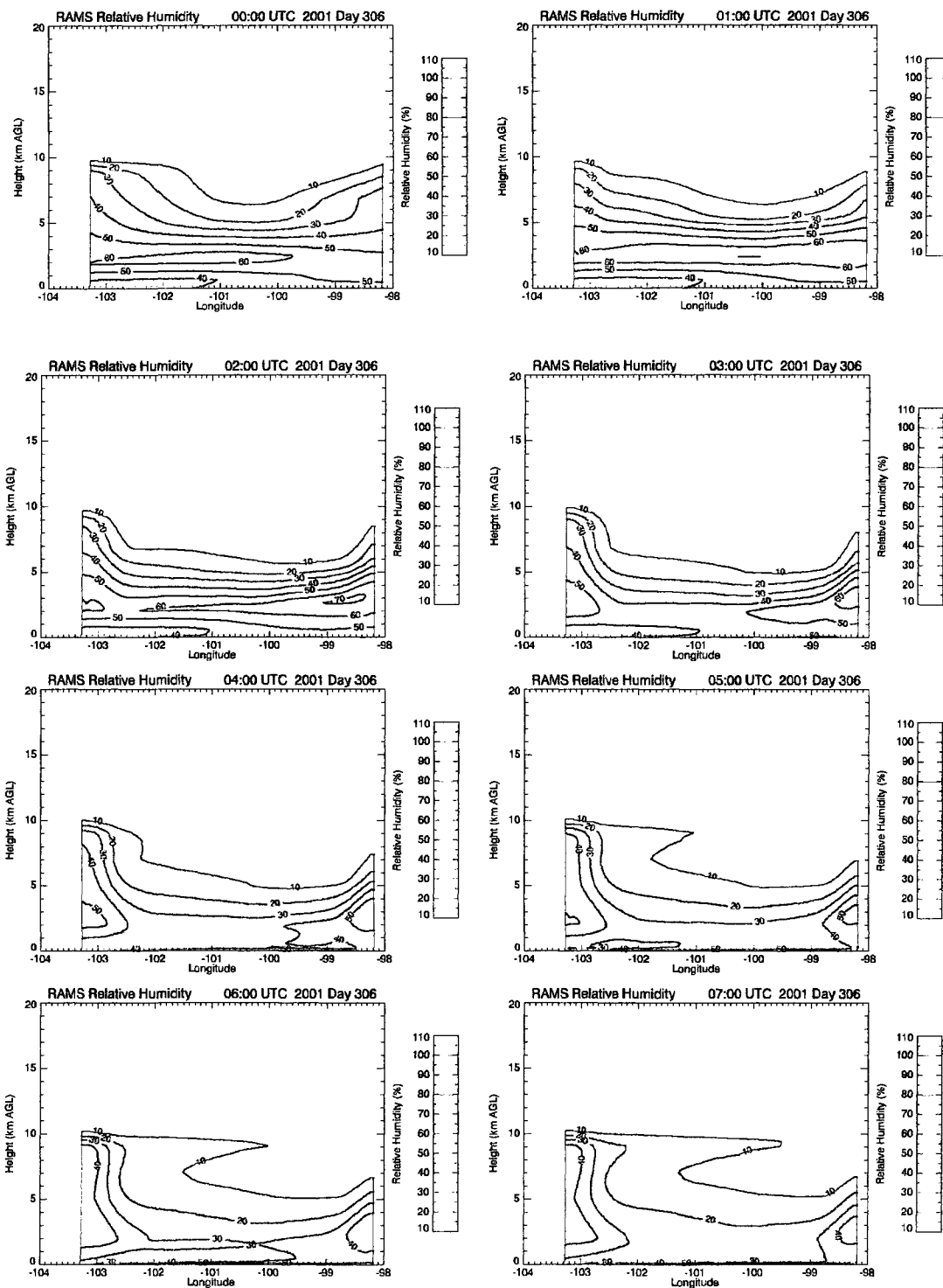


Figure 4.1. RAMS-simulated relative humidity (%) for the X-Z cross-section through North Platte, NE at hourly intervals beginning 00 UTC 2 November 2001.

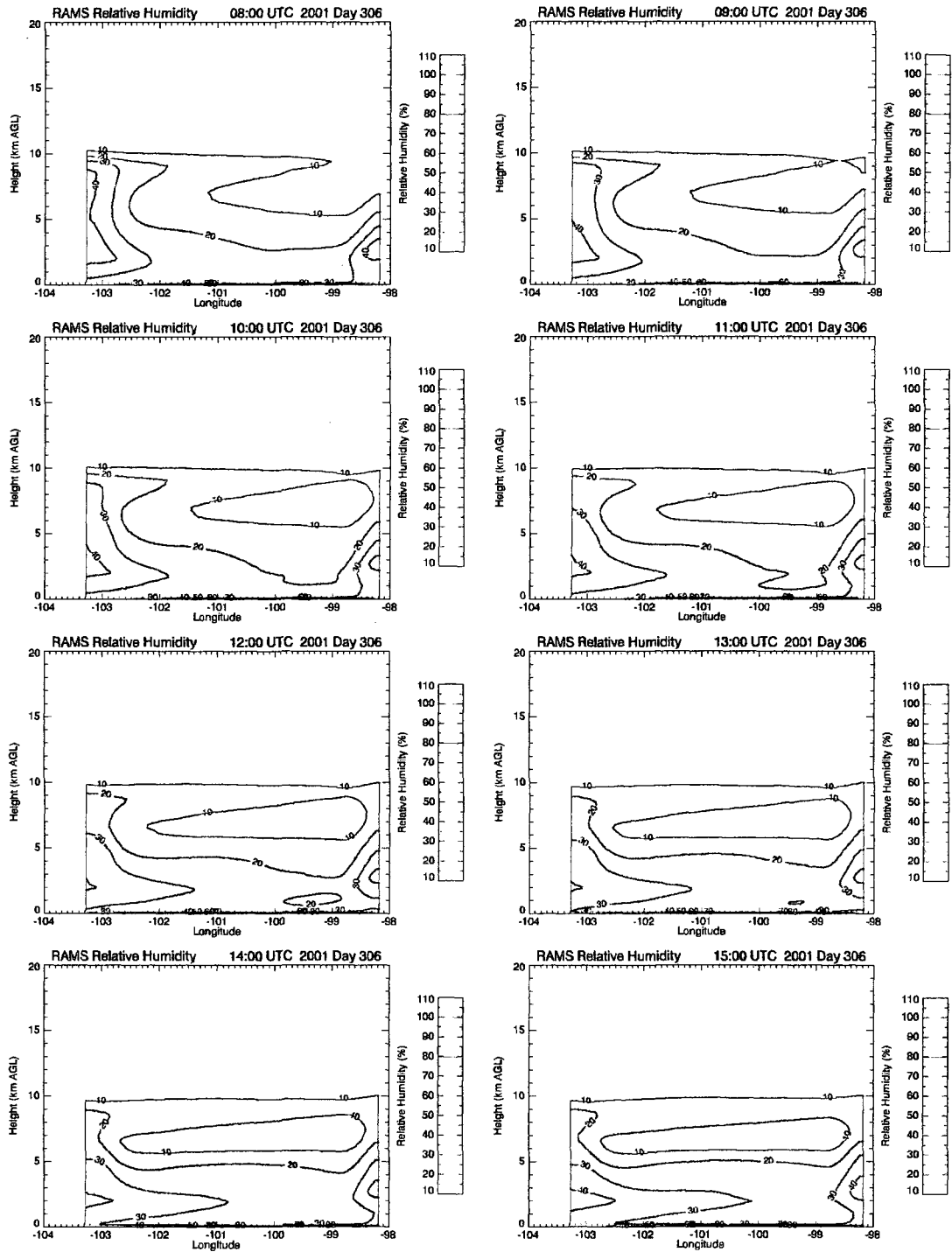


Figure 4.1 continued.

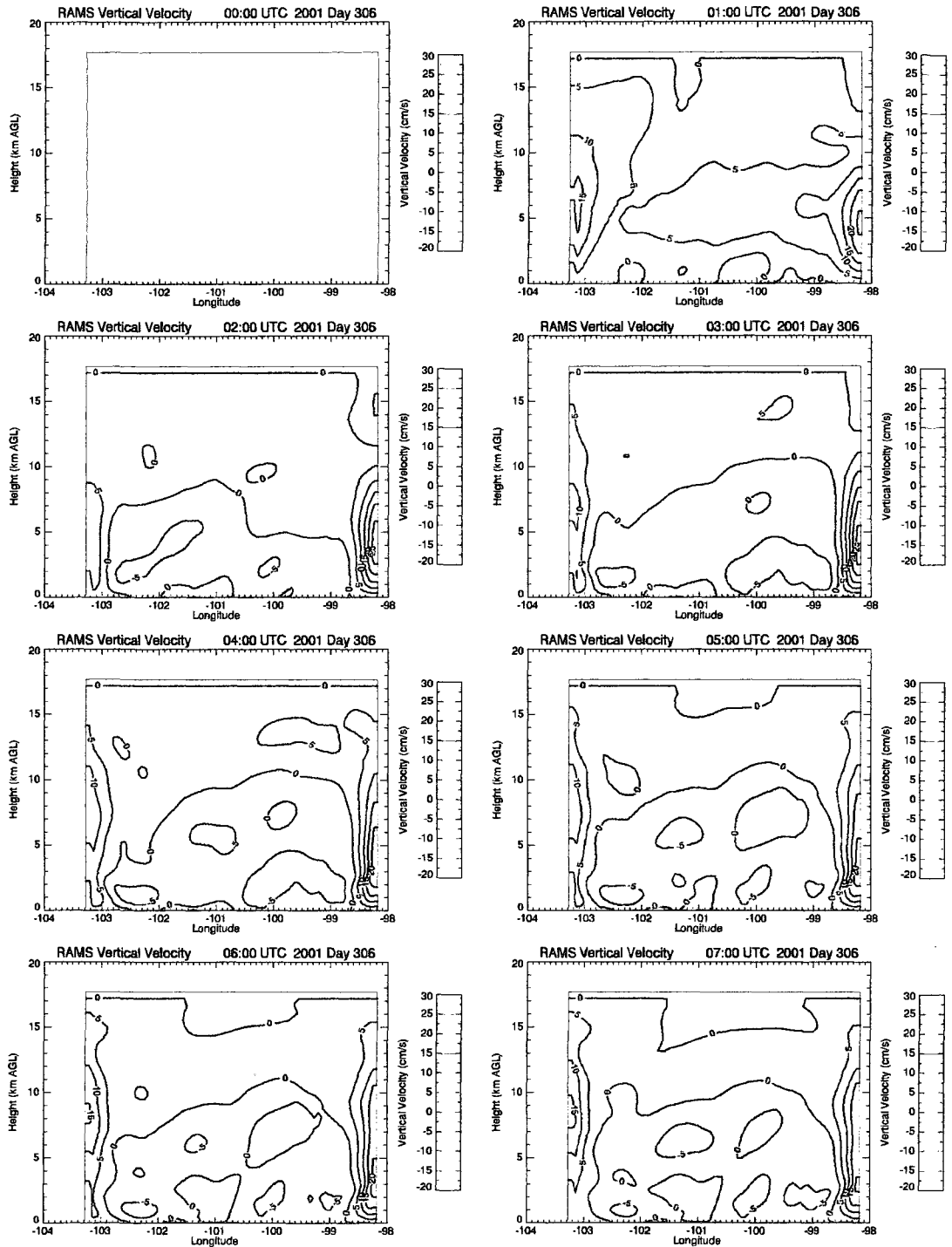


Figure 4.2. RAMS-simulated vertical velocity for the X-Z cross-section through North Platte, NE at hourly intervals beginning 00 UTC 2 November 2001.

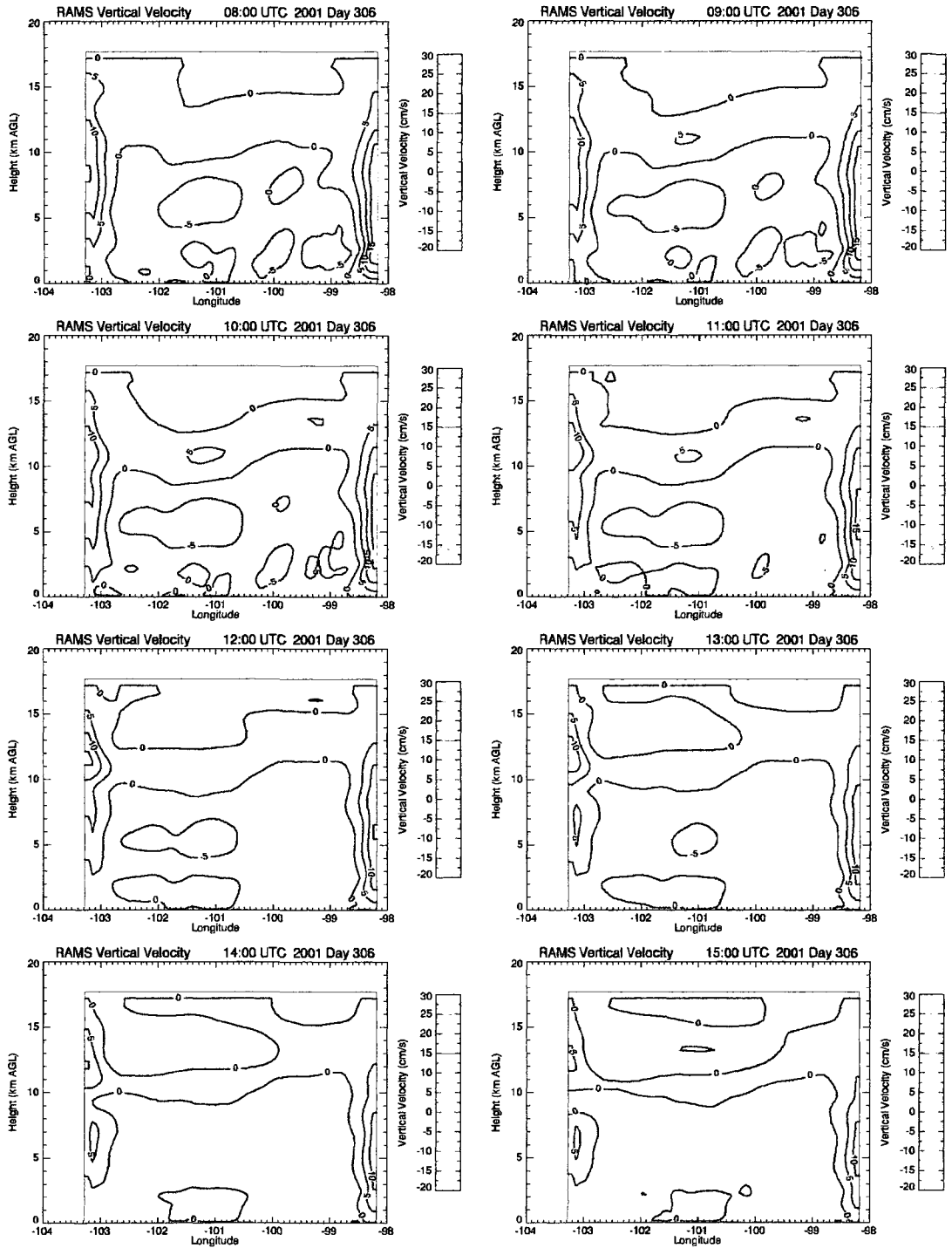


Figure 4.2 continued.

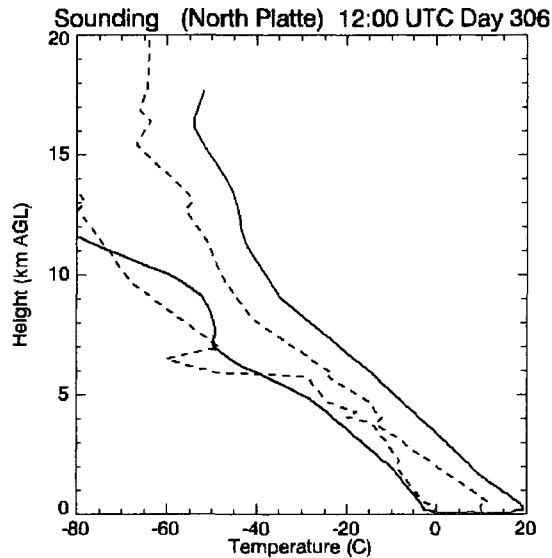


Figure 4.3. Comparison of RAMS-simulated (solid lines) and observed (dashed) sounding of temperature (red) and dew point (green) at North Platte, NE, 12 UTC 2 November 2001.

radiosonde launch at North Platte, NE (Figure 4.3) indicates that both the model temperature and dew point are in error, resulting in the model's low relative humidity values at this time. The radiosonde passed through the observed cloud and its signature is evident in Figure 4.3 just below 4 km AGL, where the observed temperature and dew point approach the same value at the base of a slight temperature inversion. The modeled temperature profile, however, is biased warm by 5 – 10 °C throughout the troposphere, while the dew point is biased low below 6 km. The largest errors in dew point occur between 2 and 6 km AGL, the layer in which the observed cloud formed, making this a poor simulation of the 2 November 2001 case study.

Attempts were made to improve this initial forward model run. The RAMS Newtonian relaxation (nudging) scheme (Walko and Tremback 2002) was applied to levels above 12 km, with an e-folding timescale of 1000 seconds. In addition, radiative transfer

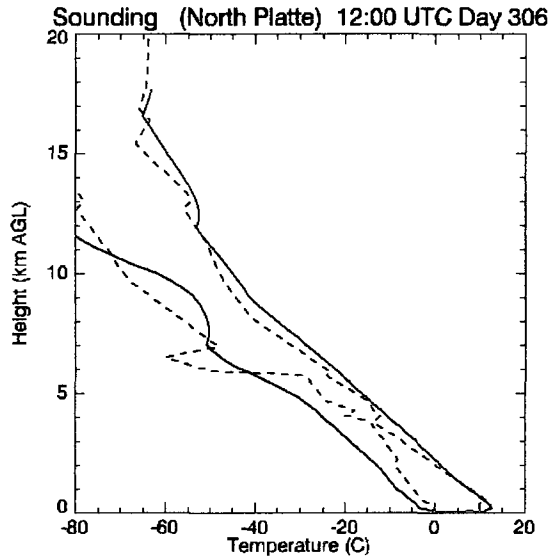


Figure 4.4. Same as Figure 4.3 except, in this case, the frequency of radiative transfer calculations was increased and nudging was added as described in the text.

calculations in RAMS were increased in frequency from once every twenty minutes of model time to once every ten minutes. The resulting 12:00 UTC temperature profile is much closer to the observations (Figure 4.4), and the relative humidity is increased as a result (Figure 4.5), although the model is still not close to producing a cloud. The vertical velocity remains largely unchanged.

The result of the nudging and more frequent radiative transfer updates is that the temperature and pressure (not shown) are kept closer to the observations, although there are still some significant differences. The surface temperatures are still biased warm throughout the domain (Figure 4.6). As will be discussed in the next chapter, the surface temperature has a significant effect on the results of the assimilation of the infrared window channels. In addition, the dew point profile is largely unchanged (cf. Figure 4.3 and Figure 4.4), and is still biased low throughout the low to mid- troposphere, except at the surface (Figure 4.6).

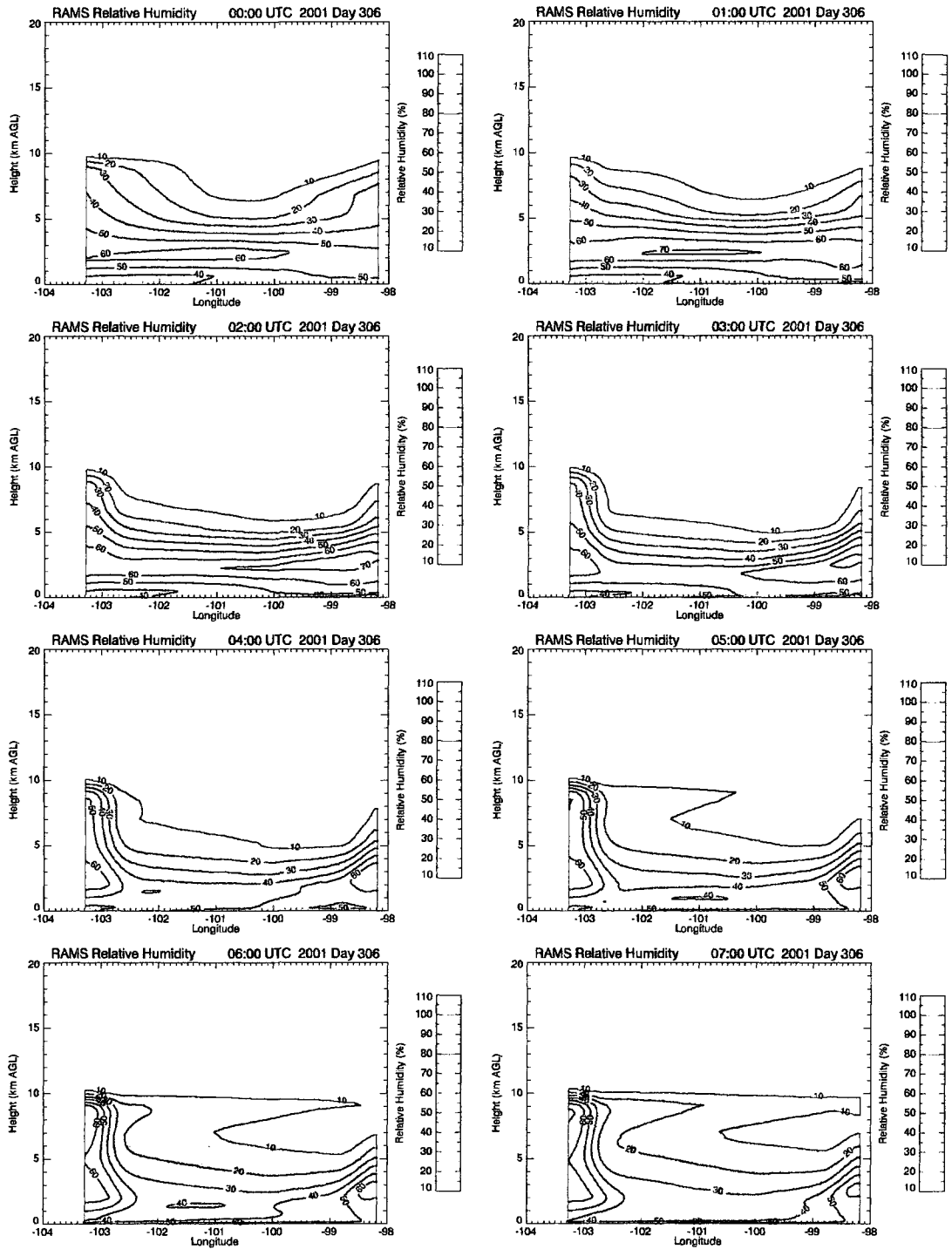


Figure 4.5. Same as Figure 4.1 except, in this case, the frequency of radiative transfer calculations was increased and nudging was added as described in the text.

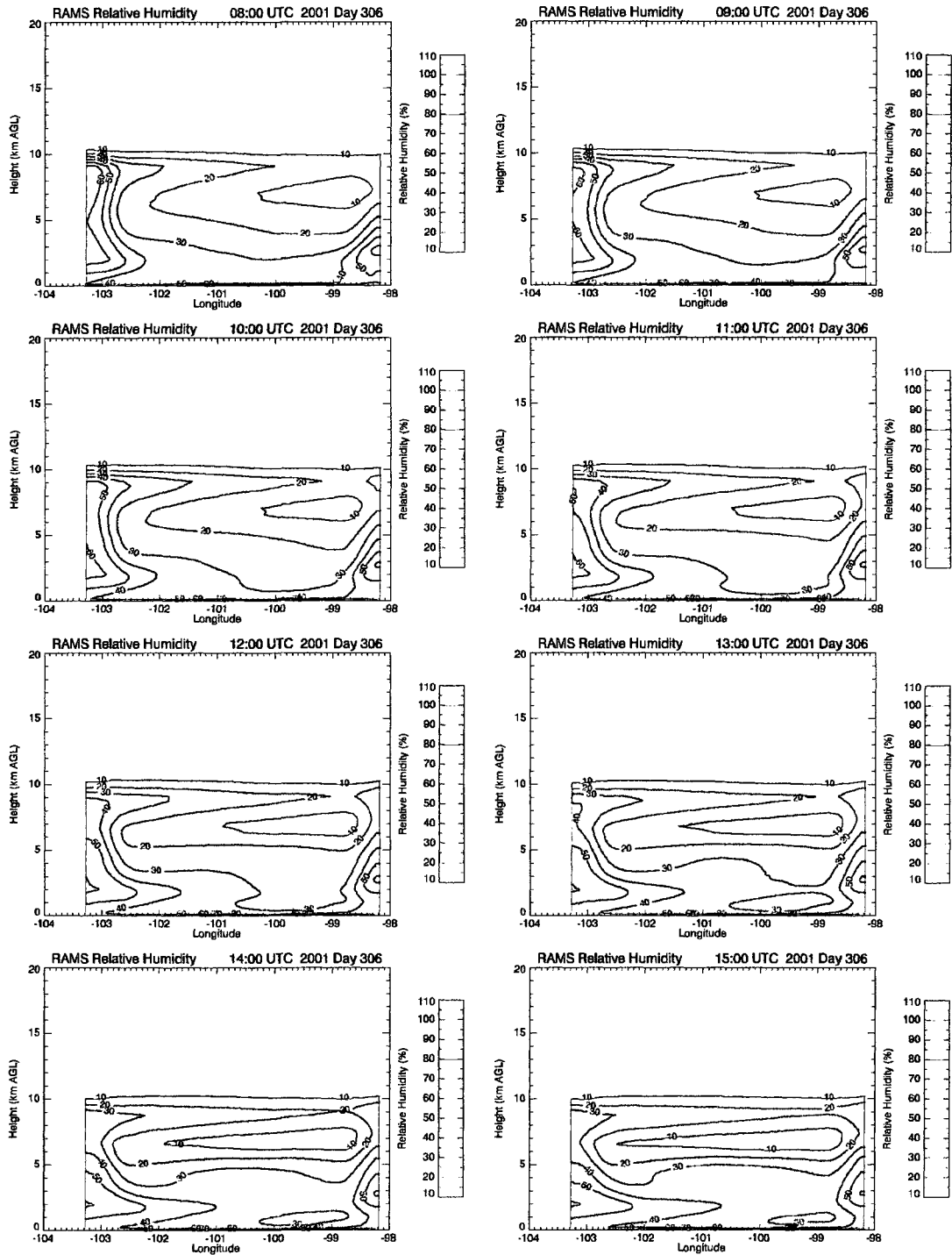


Figure 4.5 continued. Note that the relative humidity at 12:00 UTC between 1 and 5 km AGL is 10-20% greater than in Figure 4.1, due to improvements in the temperature profile.

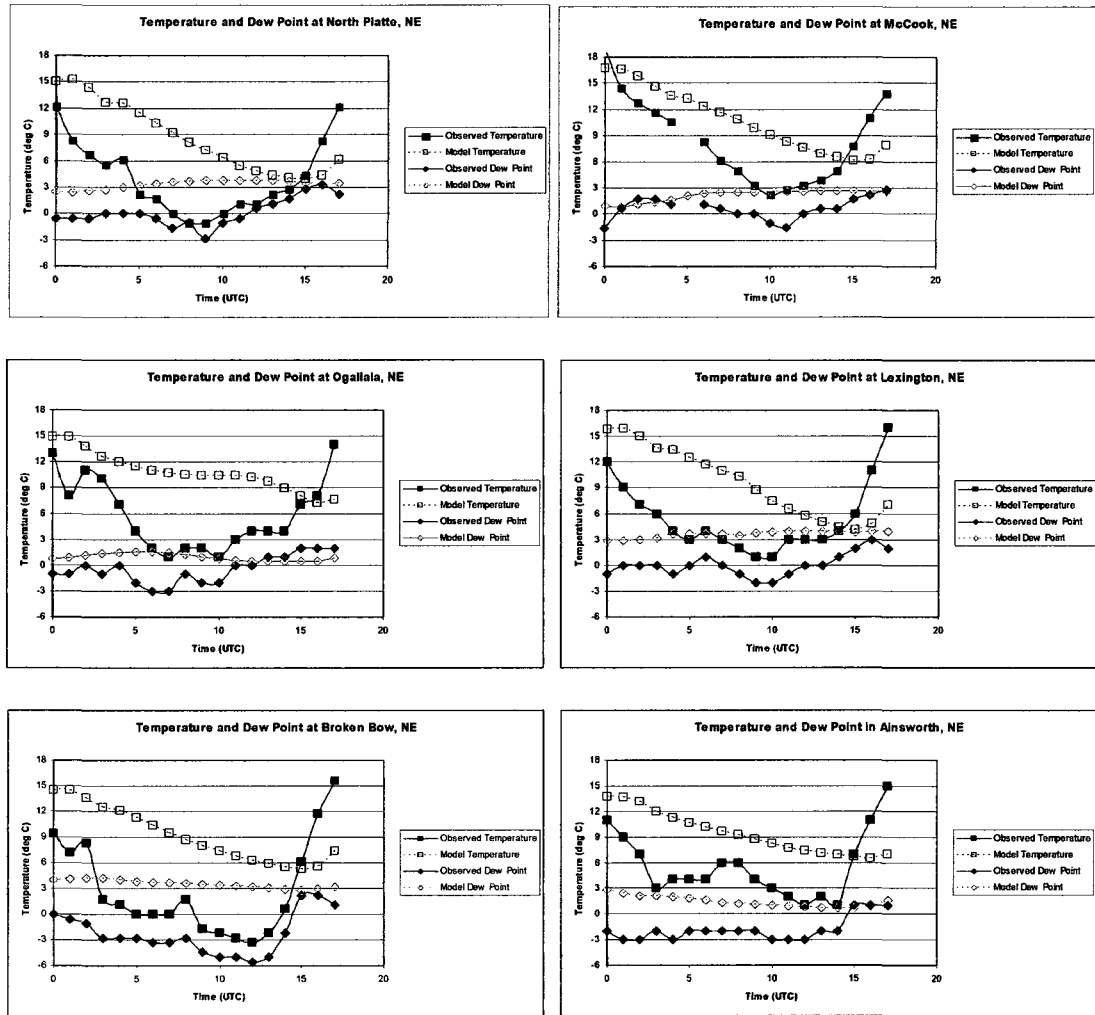


Figure 4.6. Time series plots of surface temperature (blue) and dew point (green) for 2 November 2001 from RAMS (open symbols, dashed lines) and surface observing stations (closed symbols, solid lines) for selected locations within the model domain. Model data extracted from the simulation represented by Figures 4.4 and 4.5. Observations courtesy of the National Severe Storms Laboratory Historic Weather Archive.

Although the results of the nudged forward model run are closer to the observations than the non-nudged model run, RAMDAS failed to find the minimum of the cost function for each of the assimilation experiments initialized with output from this “improved” run. This appears to be due to the model having less “wiggle room”, i.e. there is less the model can change that would decrease the cost function. The small cloud top inversion and thin layer of high

relative humidity evident in the observed sounding may also be below the sensitivity limit of RAMDAS, given the assumed decorrelation lengths. Therefore, in each of the assimilation experiments presented in this chapter, RAMDAS was initialized with output from the non-nudged forward model run represented by Figures 4.1-4.3, where a minimum of the cost function was found.

Neither of the RAMS simulations presented in this section performed as well as the simulations initialized with Eta reanalysis data presented in Section 2.3, except that none of them produced a cloud. This may be due to differences in grid size and spacing or to the quality of the reanalysis data. In this section, we have demonstrated that the forward model simulation can be improved by adding nudging and increasing the frequency of the radiative transfer calculations. However, from a data assimilation perspective, the fact that we are initializing the data assimilation experiments with the less accurate non-nudged simulation is considered a benefit rather than a hindrance. The observations to be assimilated are expected to have more of an impact on the forecast when the model and/or initialization data are poor and this impact will be more clearly visible.

4.2 Experiment 1: GOES Imager

The first experiment presented examines the impact of assimilating the water vapor channel (channel 3, 6.7 μm) and infrared window channel (channel 4, 10.7 μm) data from GOES Imager. As discussed previously, RAMDAS was initialized with the 11:00 UTC output of the initial (non-nudged) forward model run of RAMS presented in the previous section.

The GOES Imager brightness temperatures for each channel from one observation time (11:45 UTC) were assimilated.

The value of the observational component of the cost function after each iteration is shown in Figure 4.7, along with the cost associated with each channel. The minimization loop was stopped after four iterations, where the change in cost function value was deemed small enough and therefore the minimum had effectively been found. The total cost is the sum of the costs for each channel. This cost is dominated by the channel 4 cost, which is large due to the initial surface temperature bias and lack of clouds. Note, however, that the minimization algorithm is designed to minimize the total cost function, not the cost function for each channel. Thus, the cost associated with channel 3 increases during the second iteration, an increase that is more than offset by the large decrease in cost associated with channel 4. At the end of the assimilation, the final channel 3 cost is higher than its initial value.

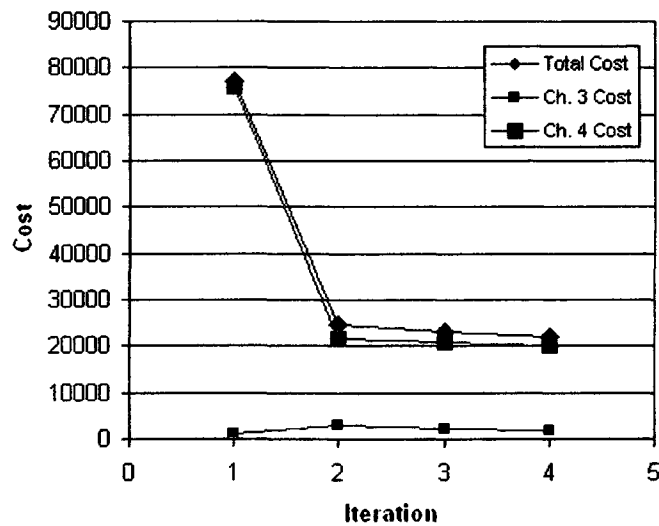


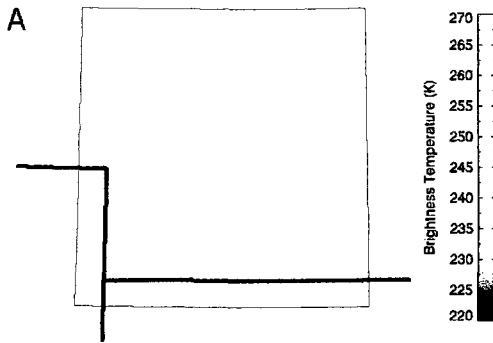
Figure 4.7. The observational component of the cost function vs. iteration number. The pink line indicates the cost due to GOES Imager channel 3 observations, the green line indicates the cost due to channel 4 observations and the blue line indicates the total cost of all observations.

The cost, as shown in Section 3.1, is effectively a weighted sum of the squared differences between the modeled and observed brightness temperatures at each grid point. The minimization algorithm adjusts the initial (11:00 UTC) conditions of the model to minimize the difference between the modeled and observed brightness temperatures at the time of the observations (11:45 UTC). A comparison of the modeled brightness temperatures to the observations both before and after assimilation demonstrates this (Figure 4.8) and explains the trends in the channel-specific cost functions. Initially, the model (as described in the last section) is much too warm and too dry, and virtually no cloud is present (Figure 4.8A, B). After the assimilation, the channel 4 brightness temperatures (Figure 4.8D) are reduced throughout the domain, although not enough to match the observed temperature of the cloud (Figure 4.8F). The channel 3 brightness temperatures (Figure 4.8A, C) are also reduced, most prominently in the southern half of the domain where the observed brightness temperatures are the lowest (Figure 4.8 E), although they are reduced a little too much (a fact that is reflected by the slight increase in the channel 3 cost over the course of the assimilation).

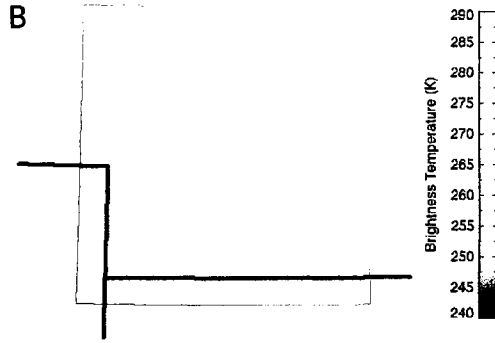
While the modeled brightness temperatures more closely match the observations, the result of the assimilation is no closer to forming a mid-level cloud. A comparison of the modeled and observed temperature and dew point soundings at North Platte shows that the reduction of brightness temperatures in the window channel (channel 4) is due to a cooling of the surface (Figure 4.9). This cooling of the surface occurs throughout the domain (Figure 4.10).

The X-Z cross-section of relative humidity through North Platte at the end of the assimilation (Figure 4.11) shows the relative humidity decreased throughout the low to mid-troposphere in this portion of the domain, except below 1 km AGL, where the relative humidity is greater than 90%. The low relative humidity is a result of the assimilation

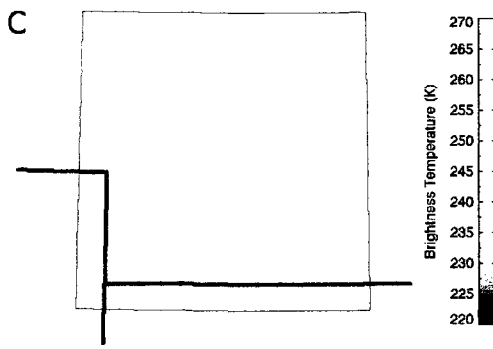
Ch. 3 Model (Before) 11:45 UTC 2001 Day 306



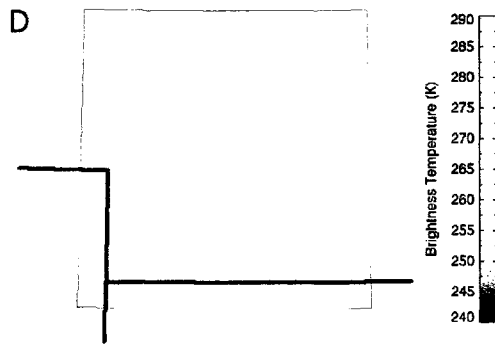
Ch. 4 Model (Before) 11:45 UTC 2001 Day 306



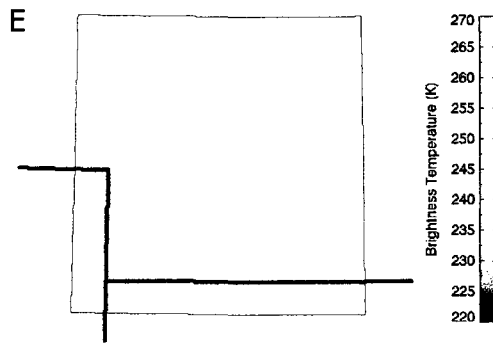
Ch. 3 Model (After) 11:45 UTC 2001 Day 306



Ch. 4 Model (After) 11:45 UTC 2001 Day 306



Ch. 3 Observed 11:45 UTC 2001 Day 306



Ch. 4 Observed 11:45 UTC 2001 Day 306

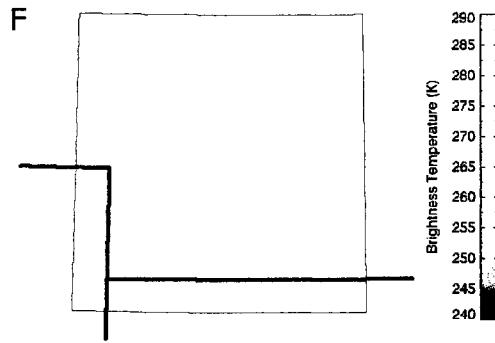


Figure 4.8. Comparison between model-simulated brightness temperatures and observed brightness temperatures for GOES Imager channels 3 and 4 at 11:45 UTC 2 November 2001. A – B) Modeled brightness temperatures for channels 3 and 4 before assimilation. C – D) Modeled brightness temperatures for channels 3 and 4 after assimilation. E - F) Observed brightness temperatures from GOES Imager channels 3 and 4.

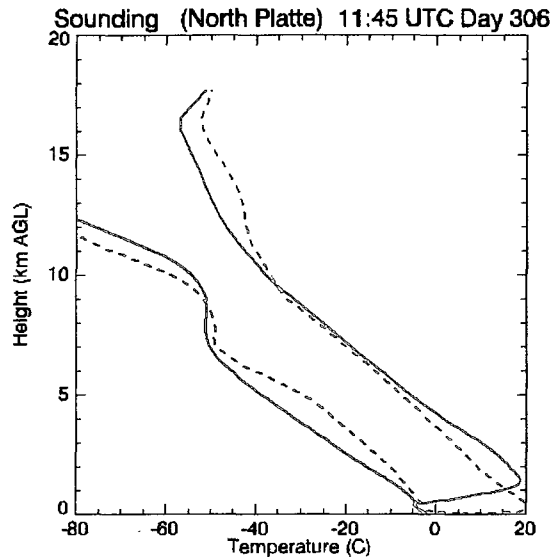


Figure 4.9. Comparison between model-simulated soundings of temperature (red) and dew point (green) at North Platte, 11:45 UTC, before assimilation of GOES Imager ch. 3 and 4 (dashed lines) and after assimilation (solid lines).

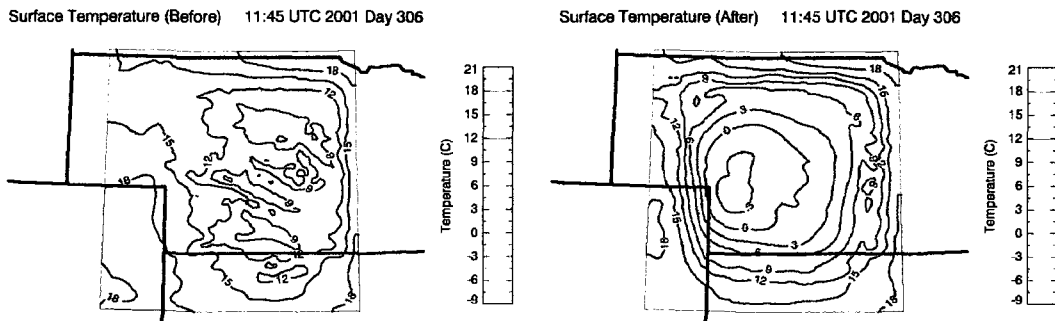


Figure 4.10. Model-simulated surface temperature ($^{\circ}\text{C}$) at 11:45 UTC before assimilation of GOES Imager ch. 3 and 4 (left) and after assimilation (right).

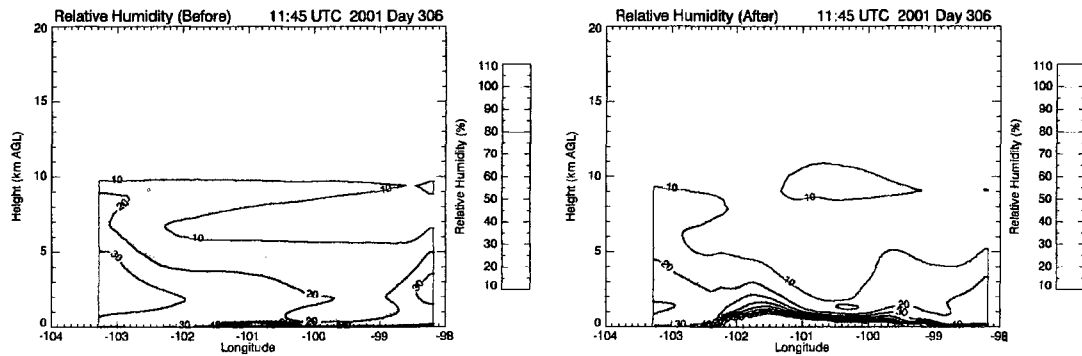


Figure 4.11. X-Z cross section of model-simulated relative humidity through North Platte at 11:45 UTC both before assimilation of GOES Imager ch. 3 and 4 (left) and after assimilation (right).

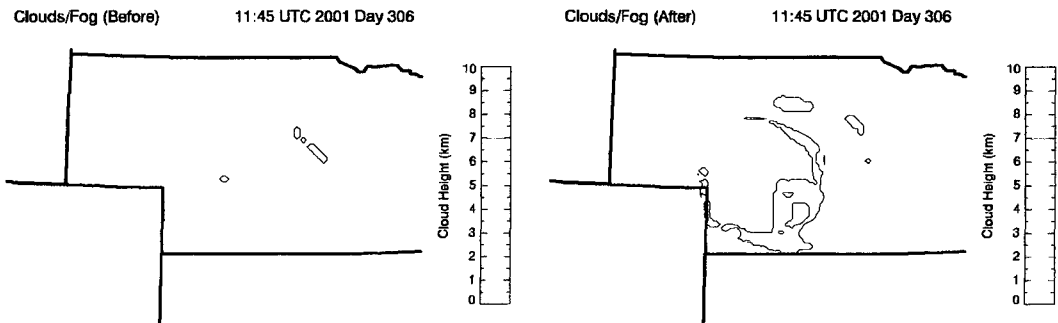


Figure 4.12. Location and height of model-simulated clouds, both before assimilation of GOES Imager ch. 3 and 4 (left) and after assimilation (right). Colors indicate height of the top of the cloud layer (km AGL).

both warming the atmosphere between 1 and 5 km AGL and drying the atmosphere below 7 km AGL (Figure 4.9). Note also in Figure 4.9 that the dew points were increased above 9 km AGL. A few patches of fog existed before assimilation, and the assimilation increased the amount of fog (Figure 4.12).

The dew point increase in the upper troposphere is more pronounced in the southern half of the domain (Figure 4.13), where the brightness temperatures in channel 3 were reduced the most (Figure 4.8). The relative humidity is increased to 80% at 7.5 km AGL and exceeds 90% at 11.5 km AGL in the X-Z cross-section through Imperial, NE (Figure 4.14), which is located 66 km south of the North Platte cross-section shown in Figure 4.11. These

elevated layers of high relative humidity occur much higher than the observed mid-level cloud.

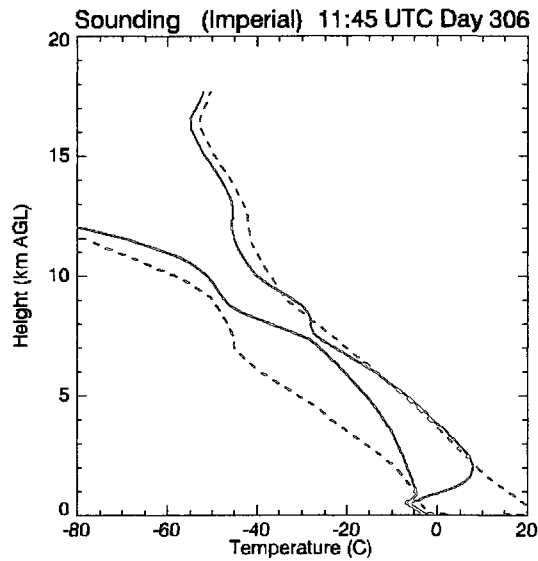


Figure 4.13. Comparison between model-simulated soundings of temperature (red) and dew point (green) at Imperial, NE, 11:45 UTC before assimilation of GOES Imager ch. 3 and 4 (dashed lines) and after assimilation (solid lines). Imperial is located approximately 100 km southwest of North Platte.

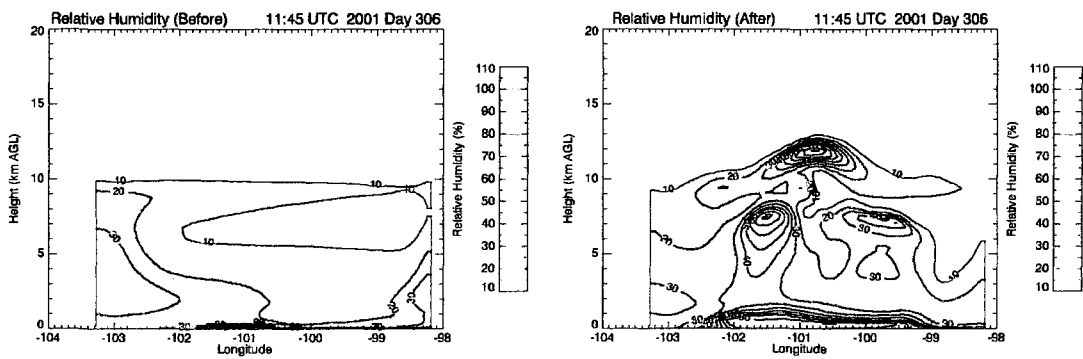


Figure 4.14. X-Z cross section of model-simulated relative humidity through Imperial, NE, at 11:45 UTC both before assimilation of GOES Imager ch. 3 and 4 (left) and after assimilation (right). This cross-section is located 66 km south of the North Platte cross-section shown in Figure 4.11.

The assimilation also significantly affected the horizontal and vertical winds. Figure 4.15 shows the simulated surface wind vectors both before assimilation and after. The initial surface wind field in the model is qualitatively similar to the observed wind field (not shown), although the speeds are biased high. After assimilation, the wind speeds have generally increased and become much more variable in direction. The assimilation also increased the vertical velocity (Figure 4.16), replacing the subsidence in the mid-troposphere with updrafts of up to 1.5 m s^{-1} .

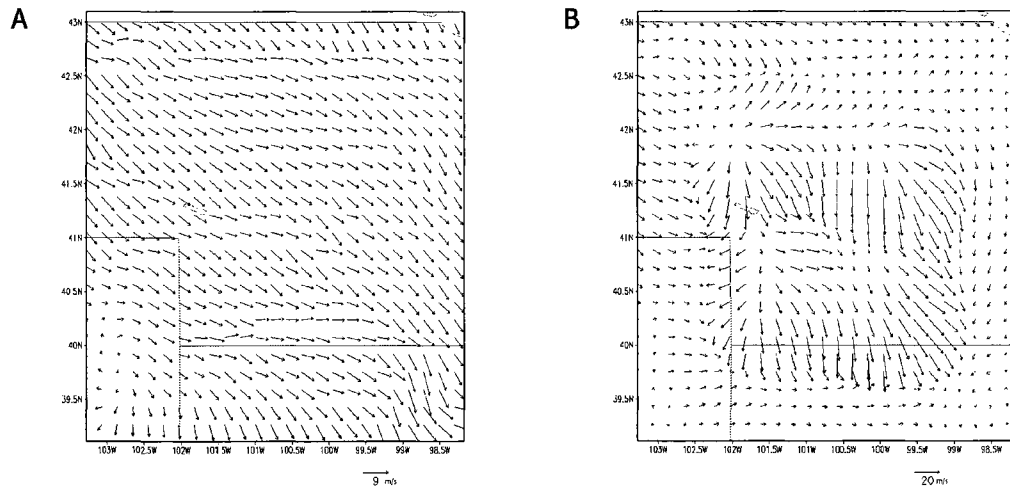


Figure 4.15. Comparison of model-simulated surface winds before assimilation of GOES Imager ch. 3 and 4 (A) and after assimilation (B). The unit-length vector in (A) represents a wind speed of 9 m s^{-1} . The unit-length vector in (B) represents a wind speed of 20 m s^{-1} .

The net result of assimilating these GOES Imager channels is that the model cooled the surface, and increased the humidity in the upper troposphere. This resulted in the production of fog, but not the mid-level cloud we are trying to capture. This can be explained by the properties of the assimilated channels and of the assimilation system itself. Channel 4 is an infrared window channel, meaning it is designed to be sensitive only to the surface or

to any clouds or particulate matter in the atmosphere. With the fog existing only in the lowest 50 m of the model prior to assimilation, the brightness temperature of the fog is nearly identical to the background surface, given the temperature profile, and is thus “invisible” in the wavelength band of channel 4. When the model contains no cloud (or “invisible” cloud as in this case), the adjoint calculates no sensitivity of the brightness temperatures to cloud. In that case, the highest sensitivity of the brightness temperatures in that channel is to the surface temperature. Thus, to minimize the cost, the model cools the surface. This cooling of the surface and lowest kilometer of the atmosphere is limited by the dew point, so that the cooling occurs until saturation is reached and fog is formed. Additionally, the increase in upper tropospheric humidity is due to the fact that channel 3 is most sensitive to upper tropospheric humidity. The adjoint-calculated sensitivities are thus constrained to the layers at which the satellite is most sensitive for each of the channels used.

4.3 Experiment 2: GOES Sounder

The second assimilation experiment explores the use of infrared window and water vapor channels from GOES Sounder. In this case, channel 7 (12.02 μm) is the window channel and channel 11 (7.02 μm) serves as the water vapor channel. Channel 11 was selected from the three water vapor channels on GOES sounder due to its designed sensitivity to mid-level water vapor. This experiment was run exactly as in the GOES Imager experiment in the previous section, except in the data that were assimilated.

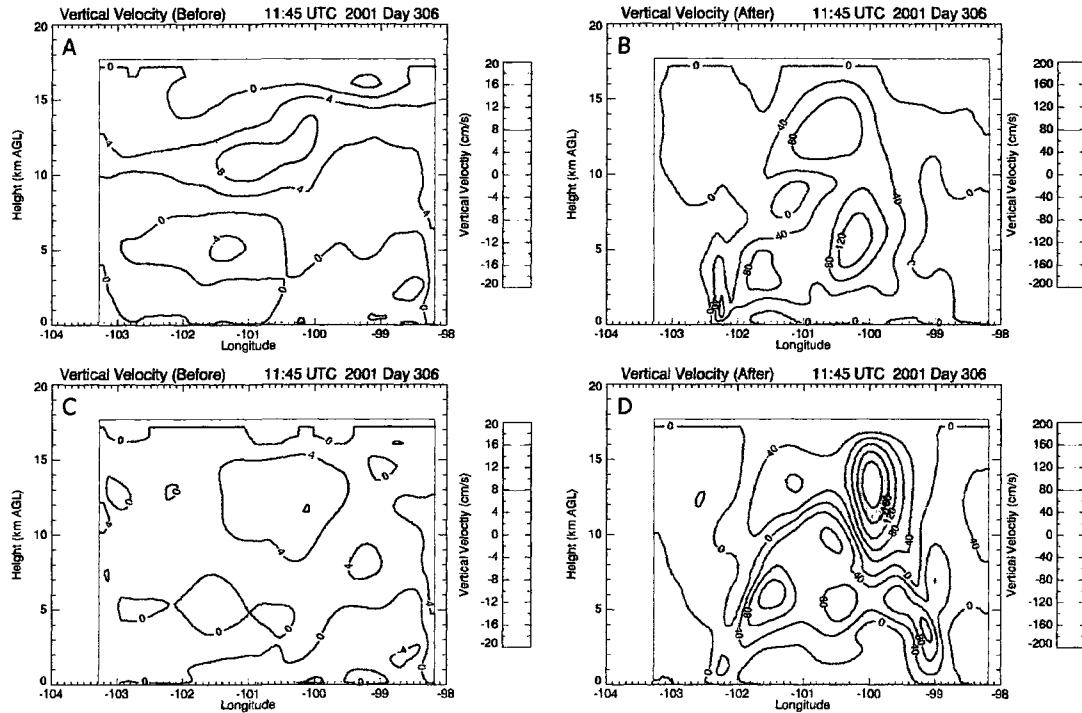


Figure 4.16. X-Z cross-section of model simulated vertical velocity (cm s^{-1}) through North Platte before assimilation of GOES Imager ch. 3 and 4 (A) and after assimilation (B). A similar cross-section through Imperial is shown also before assimilation (C) and after assimilation (D). Note the change in scales used between the before assimilation and after assimilation figures.

The observational component of the cost function vs. iteration number is shown in Figure 4.17. As with the Imager experiment, the assimilation system converged after four iterations. Also, the window channel (channel 7) cost dominates the total cost function, although the water vapor channel (channel 11) cost is nearly an order of magnitude larger. This, again, is due to the fact that the model is initially too warm and too dry. However, the total value of the cost function is initially only 58% as large as the cost function for the GOES Imager case (Figure 4.7), even though the initial model output is identical in both cases. After assimilation, the total cost function for the GOES Sounder experiment is 42% larger than in the GOES Imager experiment. As will be shown, the cost function by itself is not an accurate indicator of the quality of the results.

A comparison between the model-simulated brightness temperatures for each channel and the satellite observations at 11:45 UTC both before and after assimilation is shown in Figure 4.18. Brightness temperatures in both channels start out too high (Figure 4.18A, B), reflecting the temperature and humidity biases in the initial forward model run. After assimilation, brightness temperatures in both channels are reduced (Figure 4.18 C, D), although not to the extent of matching the observations (Figure 4.18 E, F).

Though the brightness temperature comparison and cost function values indicate that RAMDAS was unable to match the brightness temperatures as well in this experiment as in the GOES Imager experiment, a comparison of meteorological variables shows that this assimilation experiment came much closer to producing a mid-level cloud, particularly in the center of the domain. Figure 4.19 shows that the cooling in the window channel (channel 7) is not due to a dramatic decrease in the surface temperatures as in the Imager experiment. The lower brightness temperatures are instead due to the cooling and slight humidifying of the atmosphere near 2 km AGL (Figure 4.20A). The X-Z cross-section of relative humidity shows this layer clearly (Figure 4.21). This layer is approximately 2 km lower than the observed cloud (Figure 4.20B), although it is argued that an attempt to add a cloud in this layer is an improvement over the production of fog. The assimilation does not produce a cloud in this layer, and in fact does little with the few patches of fog present in the initial forward model run (Figure 4.22).

The comparison between the post-assimilation sounding with the observed sounding (Figure 4.20B) also reveals that this assimilation produced too much moisture between 3 and 13 km AGL near the center of the domain. This resulted in the reduction of model-simulated brightness temperatures in channel 11 to values to near what was observed (Figure 4.18B, D, F), although the assimilation failed to replicate the southwest-to-northeast gradient in moisture that was observed.

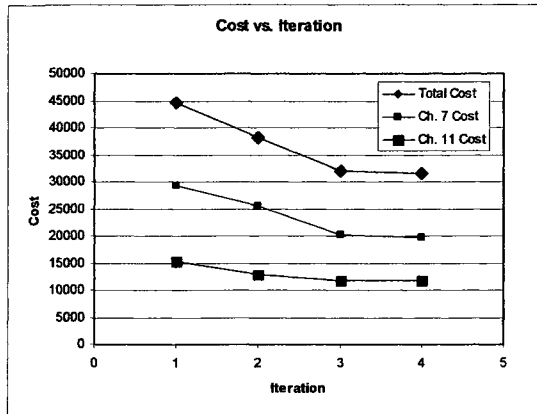
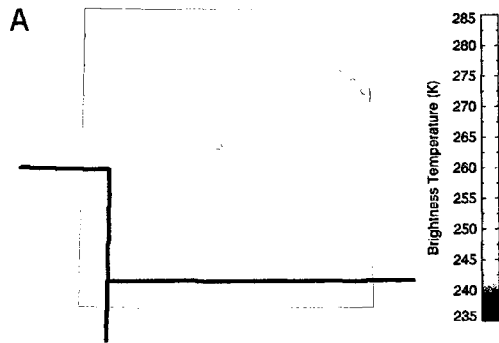


Figure 4.17. The observational component of the cost function vs. iteration number. The pink line indicates the cost due to GOES Sounder channel 7 observations, the green line indicates the cost due to channel 11 observations and the blue line indicates the total cost of all observations.

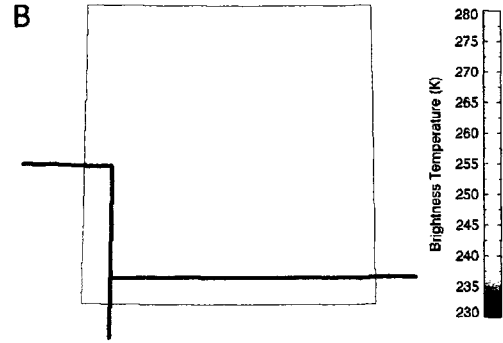
The extreme moistening of the mid- and upper troposphere in the center of the domain in this experiment may be explained as follows. In satellite water vapor channels, such as channel 11 in this case, the brightness temperature is related to the temperature of the primary emitting layer. As the amount of water vapor increases, the emitting layer shifts higher in the vertical, where temperatures are lower, resulting in reduced brightness temperatures. Since the model is 10 – 15 K too warm, the assimilation must add moisture to the mid- and upper troposphere until the emitting layer moves high enough that the model temperature of that layer is equal to the temperature of the actual emitting layer.

The wind field is also adjusted in interesting ways. Surface winds are changed to a radial pattern, with winds blowing outward from the center of the domain toward the boundaries of the domain over which the cost function is calculated (Figure 4.23). This results in updrafts along those boundaries and corresponding subsidence in the center of the domain (Figure 4.24). The subsidence strengthens the inversion at 2 km AGL (Figure 4.20) such that it is much larger than the observed cloud-top inversion.

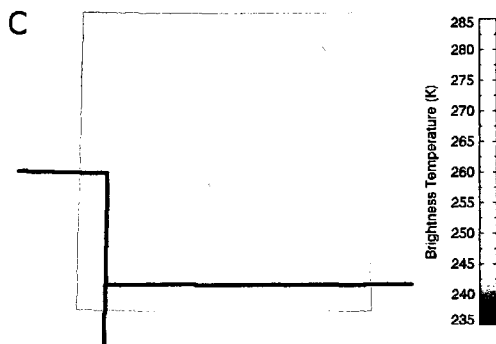
Ch. 7 Model (Before) 11:45 UTC 2001 Day 306



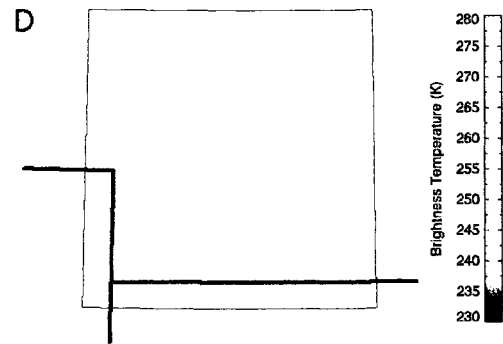
Ch. 11 Model (Before) 11:45 UTC 2001 Day 306



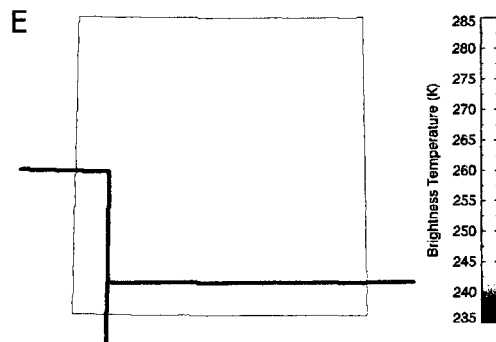
Ch. 7 Model (After) 11:45 UTC 2001 Day 306



Ch. 11 Model (After) 11:45 UTC 2001 Day 306



Ch. 7 Observed 11:45 UTC 2001 Day 306



Ch. 11 Observed 11:45 UTC 2001 Day 306

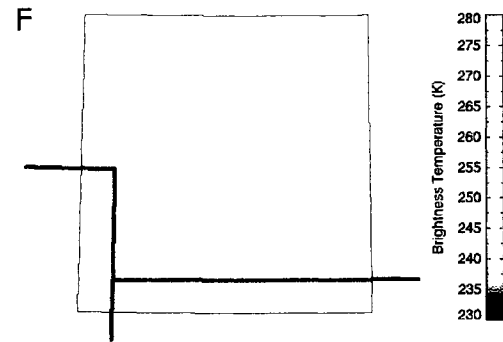


Figure 4.18. Comparison between model-simulated brightness temperatures and observed brightness temperatures for GOES Sounder channels 7 and 11 at 11:45 UTC 2 November 2001. A – B) Modeled brightness temperatures for channels 7 and 11 before assimilation. C – D) Modeled brightness temperatures for channels 7 and 11 after assimilation. E - F) Observed brightness temperatures from GOES Sounder channels 7 and 11.

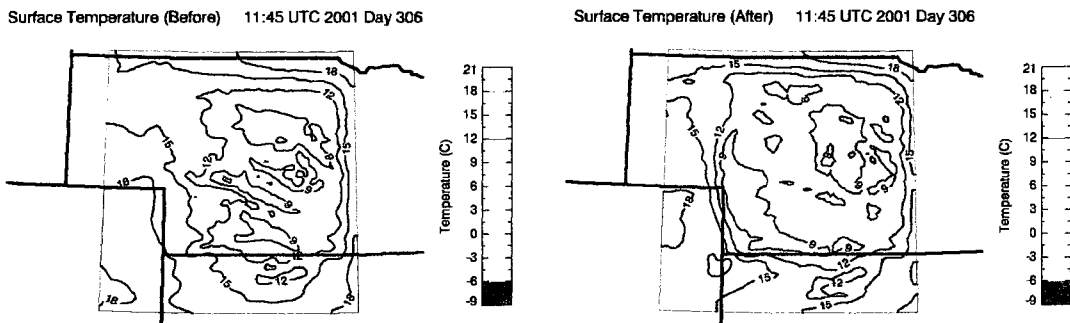


Figure 4.19. Model-simulated surface temperature ($^{\circ}\text{C}$) at 11:45 UTC before assimilation of GOES Sounder ch. 7 and 11 (left) and after assimilation (right).

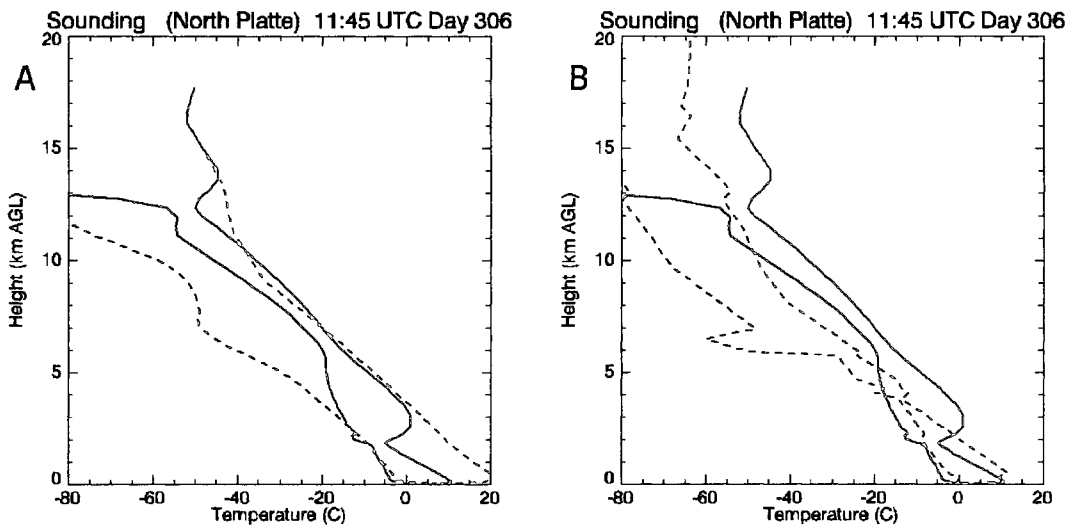


Figure 4.20 A) Comparison between model-simulated soundings of temperature (red) and dew point (green) at North Platte, 11:45 UTC, before assimilation of GOES Sounder ch. 7 and 11 (dashed lines) and after assimilation (solid lines). B) Same as A, except the dashed lines refer to the observed sounding from the National Weather Service office in North Platte at 12 UTC.

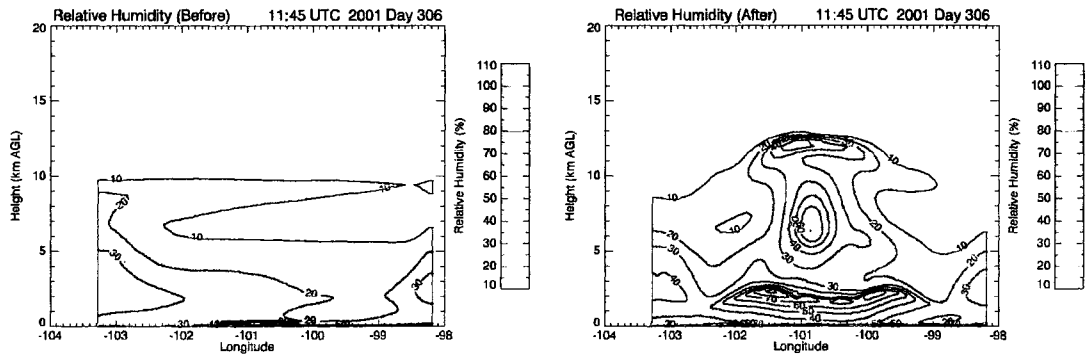


Figure 4.21. X-Z cross section of model-simulated relative humidity through North Platte, at 11:45 UTC both before assimilation of GOES Sounder ch. 7 and 11 (left) and after assimilation (right).

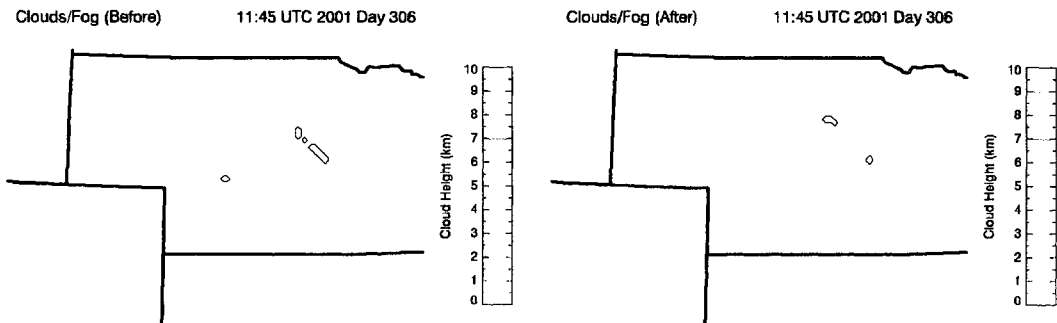


Figure 4.22. Location and height of model-simulated clouds, both before assimilation of GOES Sounder ch. 7 and 11 (left) and after assimilation (right). Colors indicate height of the top of the cloud layer (km AGL).

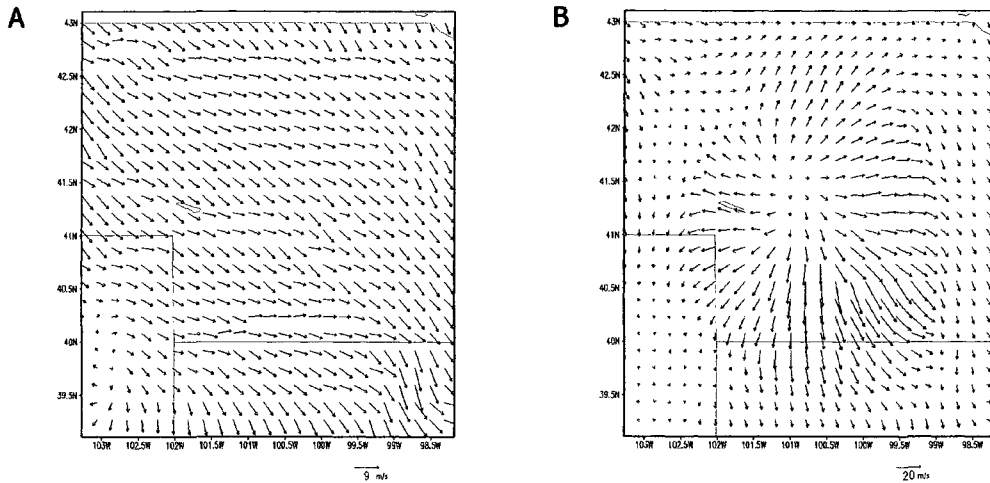


Figure 4.23. Comparison of model-simulated surface winds before assimilation of GOES Sounder ch. 7 and 11 (A) and after (B). The unit-length vector in (A) represents a wind speed of 9 m s^{-1} . The unit-length vector in (B) represents a wind speed of 20 m s^{-1} .

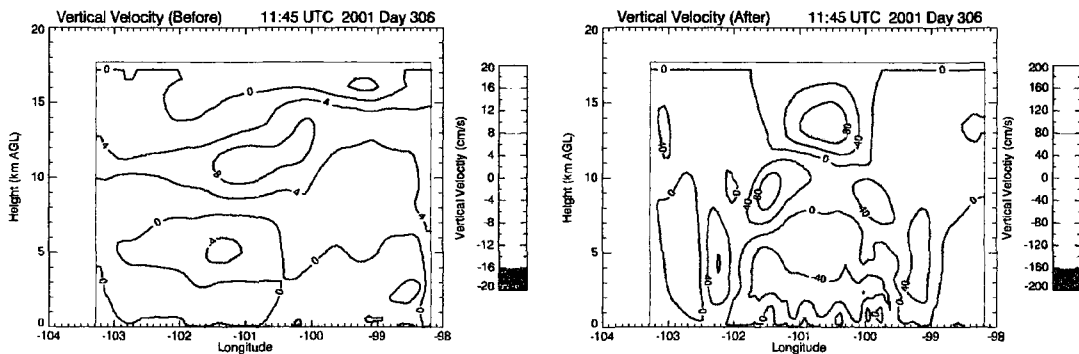


Figure 4.24. X-Z cross-section of model simulated vertical velocity (cm s^{-1}) through North Platte before assimilation of GOES Sounder ch. 7 and 11 (left) and after assimilation (right). Note the change in scales between the figures.

In summary, the primary impacts of assimilating GOES Sounder channels 7 and 11 are:

- 1) a subsidence inversion is formed near 2 km AGL, resulting in a layer of high relative humidity that is much closer to forming a mid-level cloud than the model without

assimilation; and 2) the humidity is increased too much between 4 and 13 km AGL in the center of the domain. The assimilation had less of an effect on the surface temperatures compared to the Imager experiment, and very little effect on the temperature profile above 4 km AGL.

4.4 Experiment 3: Water vapor channels only

The third and final experiment of this work utilizes only the two water vapor channels from the previous experiments: GOES Imager channel 3 (6.7 μm) and GOES Sounder channel 11 (7.02 μm). One of the original goals of this work was to determine if assimilating water vapor channel data from satellites would be sufficient to increase the mid-level humidity enough for the model to produce the cloud of 2 November 2001 (see Section 2.3). This experiment tests that hypothesis and allows us to quantify the differences between using only water vapor channels and using a combination of water vapor and window channels as shown in the previous sections.

Examination of the cost function once again indicates that RAMDAS was able to find a minimum within four iterations (Figure 4.25). Note that the initial value of the cost function for each channel is identical to the initial values for these channels shown in each of the previous experiments, due to the fact that the initial model run is identical for each of the experiments. The total cost function value is considerably less than in the previous experiments since neither channel is sensitive to the large surface temperature bias. The temperature bias in the mid- and upper troposphere is somewhat balanced by the dew point

bias in the upper troposphere (refer back to Figure 4.3). These factors combine, leading to the lower cost function values.

The results of this experiment are similar to that of the Sounder experiment presented in the previous section, although the impact of the observations is less. The comparison of brightness temperatures with the observations is presented in Figure 4. 26. This shows that brightness temperatures in each channel were reduced in a “bulls-eye” pattern near the center of the domain, although to a lesser extent than in the Sounder experiment. The model sounding at North Platte shows that this corresponds to a moistening between 3 and 13 km once again (Figure 4.27). A subsidence inversion is formed near 2 km AGL, but this inversion is not as strong as in the Sounder experiment. The relative humidity does not reach 60% anywhere in the mid-troposphere (Figure 4.28).

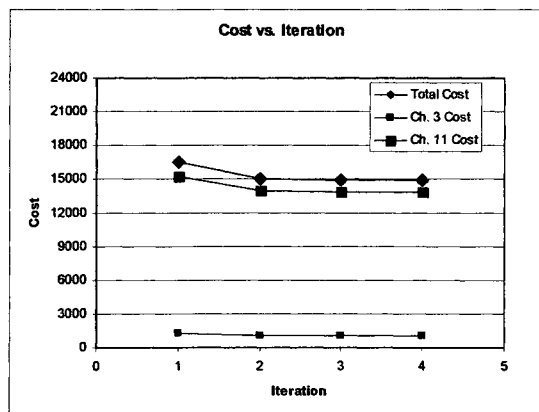


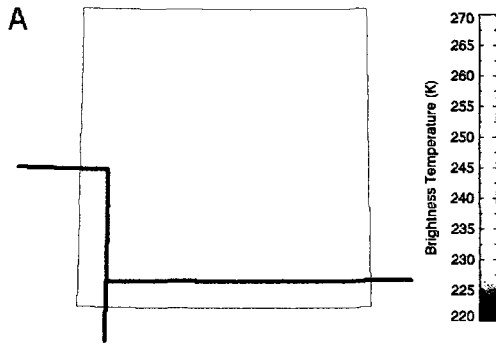
Figure 4.25. The observational component of the cost function vs. iteration number. The pink line indicates the cost due to GOES Imager channel 3 observations, the green line indicates the cost due to GOES Sounder channel 11 observations and the blue line indicates the total cost of all observations.

The assimilation induces a similar, but weaker, circulation as in the Sounder experiment (Figures 4.29 and 4.30). In this case the easterly surface winds induced to the west of the center point (North Platte) and flowing towards the boundary of the cost function domain cancel out the westerly component of the initial wind field (Figure 4.29), changing the northwest winds to north winds. Similarly, the southerly winds induced north of center (and northerly winds south of center) modify the wind field, which sets up a region of subsidence in lower troposphere at the center of the domain (Figure 4.30). Rising motions are thus induced on the boundaries of the cost function domain. This circulation results in the subsidence inversion at 2 km AGL.

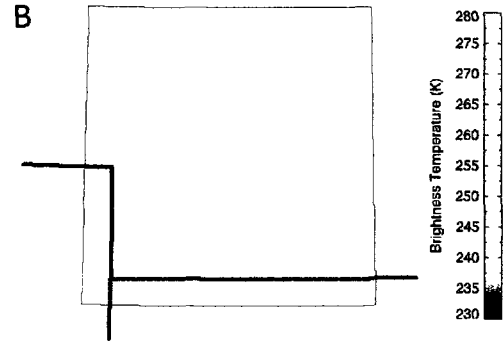
Apart from the change to the surface winds, the surface remains nearly the same after assimilation. Figure 4.31 shows that the surface temperature was largely unchanged and Figure 4.32 shows the lack of impact on the fog. No other cloud was produced as a result of the assimilation. Since neither water vapor channel is sensitive to the surface, the assimilation of only water vapor channels produces very little impact on surface parameters.

The net result of the assimilation of the two water vapor channels is that the model solution was pushed in the same direction as in the GOES Sounder experiment, although the innovation (the change in the model state vector brought about by assimilating the satellite data) was less. The model produced a subsidence inversion near 2 km AGL with a layer of higher relative humidity, but the assimilation was unable to overcome the temperature bias in the initial model run. Dew points were increased in the mid- and upper troposphere, but not enough to form a cloud.

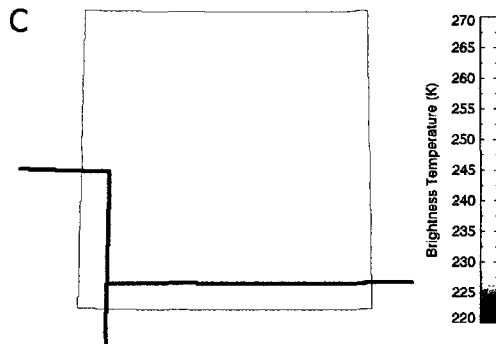
Ch. 3 Model (Before) 11:45 UTC 2001 Day 306



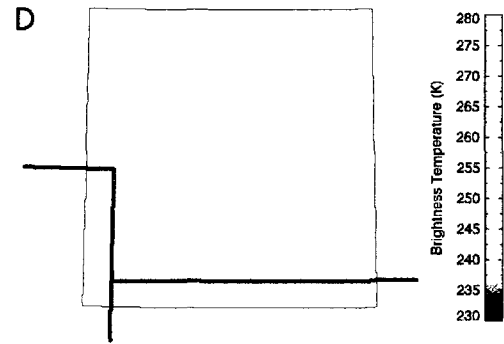
Ch. 11 Model (Before) 11:45 UTC 2001 Day 306



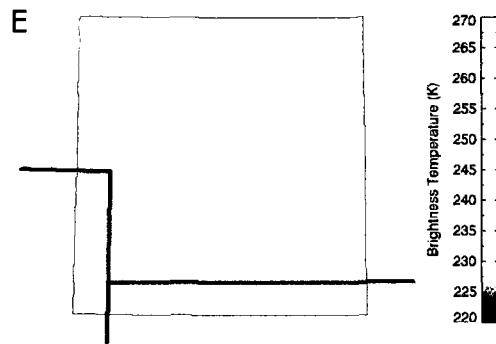
Ch. 3 Model (After) 11:45 UTC 2001 Day 306



Ch. 11 Model (After) 11:45 UTC 2001 Day 306



Ch. 3 Observed 11:45 UTC 2001 Day 306



Ch. 11 Observed 11:45 UTC 2001 Day 306

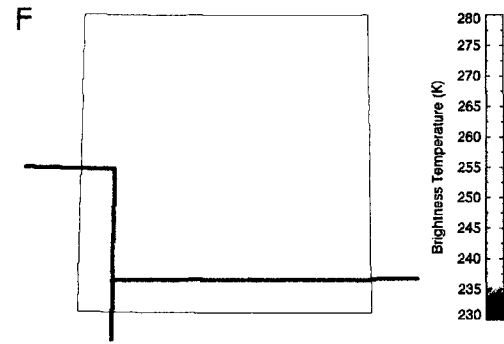


Figure 4.26. Comparison between model-simulated brightness temperatures and observed brightness temperatures for GOES Imager channel 3 and GOES Sounder channel 11 at 11:45 UTC 2 November 2001. A – B) Modeled brightness temperatures for channels 3 and 11 before assimilation. C – D) Modeled brightness temperatures for channels 3 and 11 after assimilation. E - F) Observed brightness temperatures from GOES Sounder channels 3 and 11.

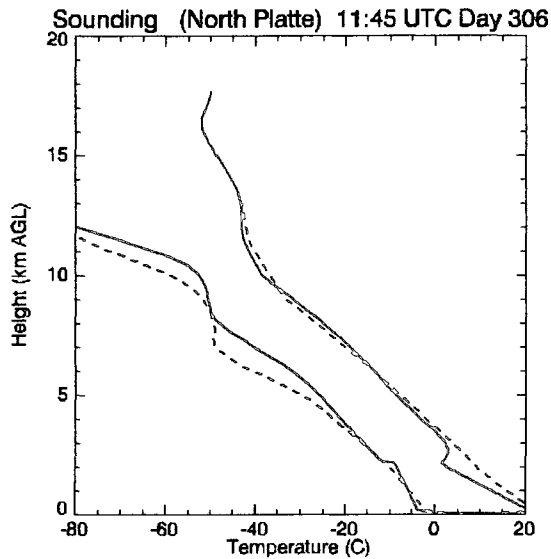


Figure 4.27. Comparison between model-simulated soundings of temperature (red) and dew point (green) at North Platte, 11:45 UTC, before assimilation of GOES Imager ch. 3 and GOES Sounder ch. 11 (dashed lines) and after assimilation (solid lines).

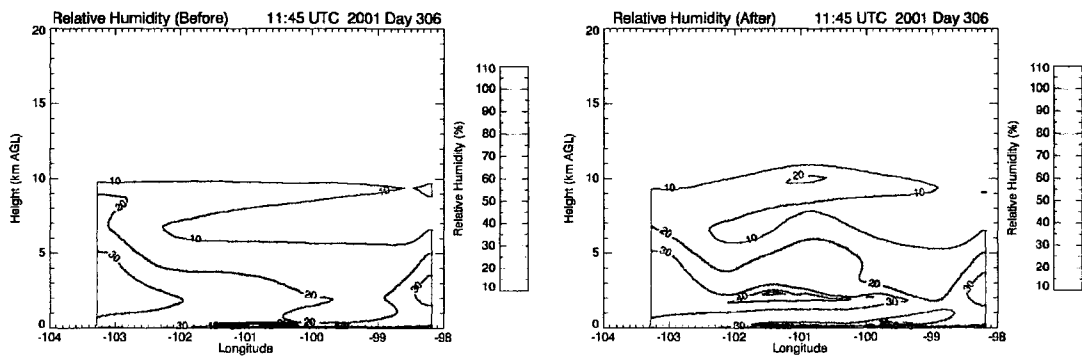


Figure 4.28. X-Z cross section of model-simulated relative humidity through North Platte, at 11:45 UTC both before assimilation of GOES Imager ch. 3 and GOES Sounder ch. 11 (left) and after assimilation (right).

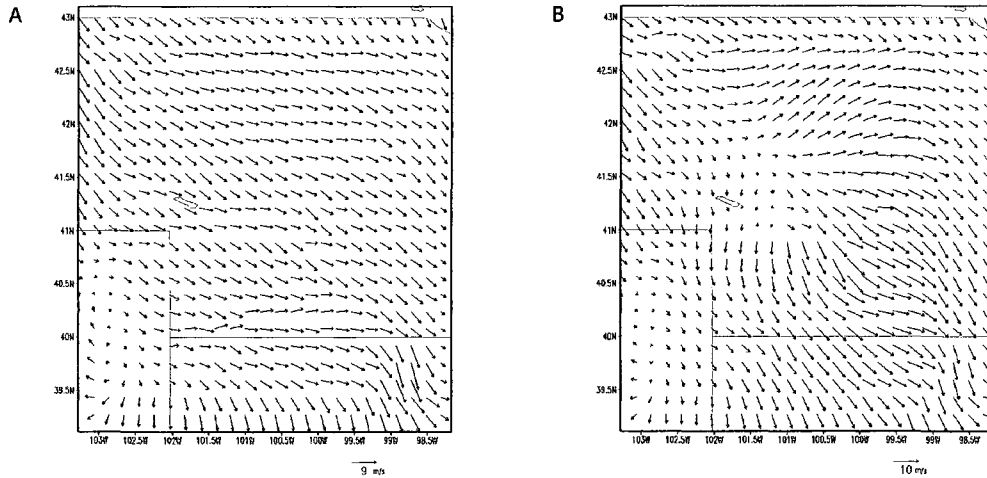


Figure 4.29. Comparison of model-simulated surface winds before assimilation of GOES Imager ch. 3 and GOES Sounder ch. 11 (A) and after assimilation (B). The unit-length vector in (A) represents a wind speed of 9 m s^{-1} . The unit-length vector in (B) represents a wind speed of 10 m s^{-1} .

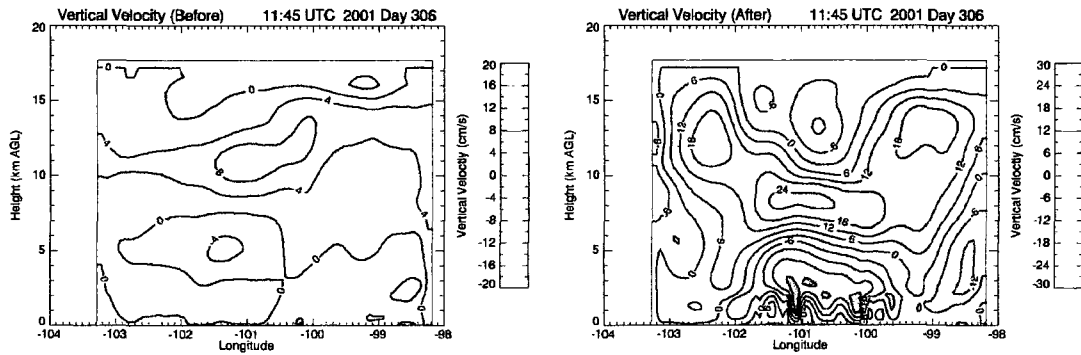


Figure 4.30. X-Z cross-section of model simulated vertical velocity (cm s^{-1}) through North Platte before assimilation of GOES Imager ch. 3 and GOES Sounder ch. 11 (left) and after assimilation (right). Note the change in scales between the figures.

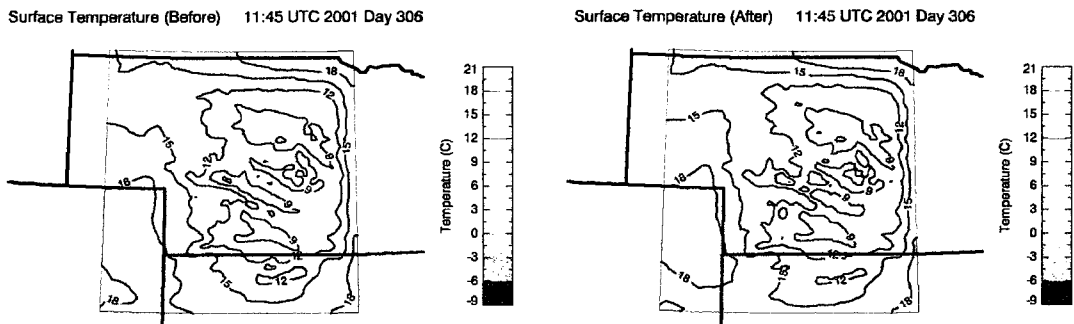


Figure 4.31. Model-simulated surface temperature ($^{\circ}\text{C}$) at 11:45 UTC before assimilation of GOES Imager ch. 3 and GOES Sounder ch. 11 (left) and after assimilation (right).

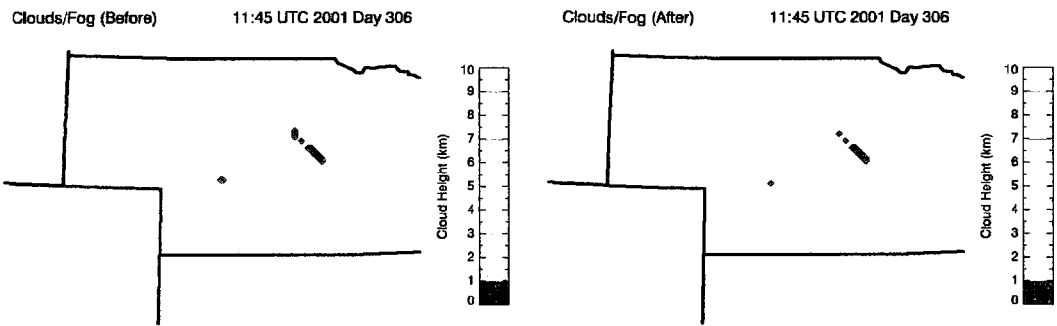


Figure 4.32. Location and height of model-simulated clouds, both before assimilation of GOES Imager ch. 3 and GOES Sounder ch. 11 (left) and after assimilation (right). Colors indicate height of the top of the cloud layer (km AGL).

4.5 The Effect of Varying Decorrelation Lengths

It has been mentioned in previous sections of this work that decorrelation lengths for atmospheric variables are not well known. Decorrelation lengths are used in the calculation of the background error covariance matrix in RAMDAS. The experiments presented earlier in this chapter used assumed values for the horizontal and vertical decorrelation lengths ($r_l^{x,y}$ and r_l^z , respectively) that are considered a reasonable first guess. These values are shown in Table 4.1. In this section, we discuss the effect changing the decorrelation lengths has on the results of the experiments already presented by both doubling and halving these decorrelation lengths.

Table 4.2 shows the values of the total observational component of the cost function after assimilation for each of the three main experiments (i.e. Imager-only, Sounder-only, and Water Vapor-only) and compares them to the cases where the decorrelation lengths presented in Table 4.1 are halved and doubled. The ratio of the post-assimilation cost function value, J_f , to the pre-assimilation cost function value, J_0 , for each of these cases is also shown. In each experiment, the value of the cost function decreases (increases) when the decorrelation lengths are increased (decreased). The observations have more (less) of an impact on the assimilation when the decorrelation lengths are increased (decreased). This may be seen more clearly from the specific results of each experiment.

Table 4.1. Default decorrelation lengths (km) for each of the control variables in RAMDAS. The horizontal decorrelation lengths are given by $r_i^{x,y}$ and the vertical decorrelation lengths are given by r_i^z .

Control Variable	$r_i^{x,y}$ [km]	r_i^z [km]
pressure	150	2.0
temperature	100	2.0
u-wind	150	2.0
v-wind	150	2.0
w-wind	50	1.0
total water mixing ratio	50	1.0
rain water mixing ratio	50	0.5
pristine ice water mixing ratio	50	0.5
snow water mixing ratio	50	0.5
aggregate ice water mixing ratio	50	0.5
groupel mixing ratio	50	0.5
hail mixing ratio	50	0.5

Table 4.2. Final cost function value (J_f) and the ratio of the final cost function value to the initial cost function value (J_0) for each set of data assimilated and each set of decorrelation lengths (r_i).

	Imager Ch. 3 & 4		Sounder Ch. 7 & 11		Imager Ch. 3 Sounder Ch. 11	
	J_f	J_f / J_0	J_f	J_f / J_0	J_f	J_f / J_0
$r_i / 2$	55144	0.714	42633	0.955	15703	0.952
default r_i	22065	0.286	31546	0.707	14914	0.904
$r_i \times 2$	16127	0.209	21119	0.473	12546	0.760

Figure 4.33 shows the comparison of the post-assimilation modeled temperature and dew point soundings from North Platte for each set of decorrelation lengths for each of the three experiments. In the case of the GOES Imager experiment, when the decorrelation lengths are halved (Figure 4.33 A), the surface is cooled less, and the inversion is not as deep or as strong as when using the default values. When the decorrelation lengths are doubled, however, the surface is cooled more and the inversion is approximately 1 km deeper (Figure 4.33 B). Similarly, assimilating the GOES Sounder data, the halved decorrelation lengths result in less cooling and, hence, a weaker inversion at and near 2 km AGL, while the doubled decorrelation lengths increased the cooling at 2 km AGL and extended this cooling all the way down to the surface (Figure 4.33 C-D). Also in the water vapor-only experiment we see the same pattern: more cooling at the inversion height (2 km AGL) when the decorrelation lengths are doubled, and less cooling when they are halved (Figure 4.33 E-F).

The additional cooling present in each experiment when the decorrelation lengths are doubled is (at least partially, if not mostly) responsible for the reduced values in the cost function seen in Table 4.2. In the water vapor-only experiment, there is also additional moistening above 7 km AGL (Figure 4.33 F) that contributes to the reduced cost function value. Recall from Sections 4.2 and 4.3 that in the window channels (Imager ch. 4 and Sounder ch. 7) the modeled brightness temperatures were still biased warm after the assimilation. Doubling the decorrelation lengths reduced this bias in both cases due to the additional cooling of the surface and lower troposphere.

In the case of the Sounder experiment, doubling the decorrelation lengths increased the depth of the layer of high (>90%) relative humidity (Figure 4.34) and resulted in the formation of clouds above 2 km AGL (Figure 4.35). This was the only configuration to produce a cloud that could be considered mid-level.

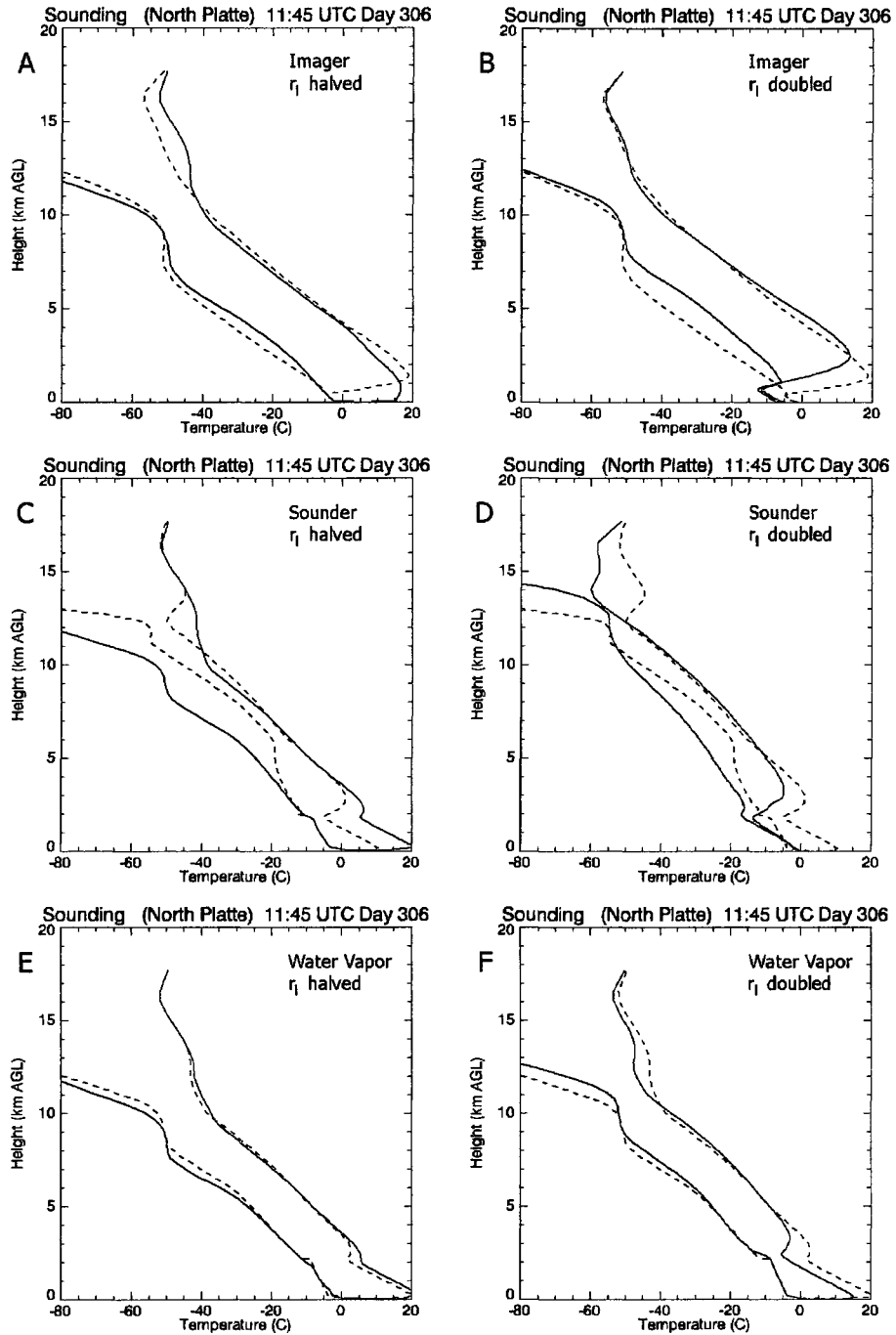


Figure 4.33. Model temperature (red) and dew point (green) soundings from North Platte, after assimilation of GOES Imager ch. 3 & 4 with decorrelation lengths halved (A) and doubled (B), after assimilation of GOES Sounder ch. 7 & 11 with decorrelation lengths halved (C) and doubled (D), and after assimilation of GOES Imager ch. 3 and GOES Sounder ch. 11 with decorrelation lengths halved (E) and doubled (F). In each figure, the dashed lines correspond to model soundings using the default values for the decorrelation lengths.

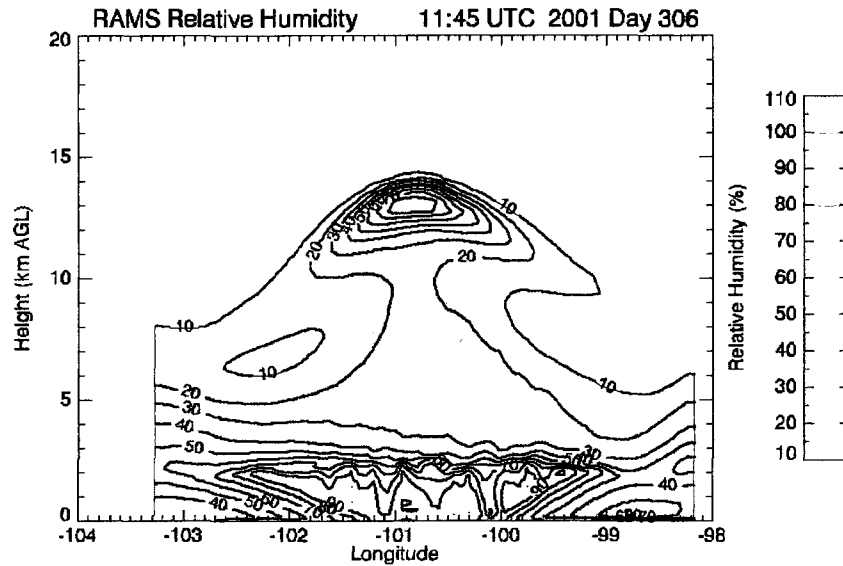


Figure 4.34. X-Z cross-section of model simulated relative humidity through North Platte after assimilation of GOES Sounder channels 7 & 11, using doubled decorrelation lengths.

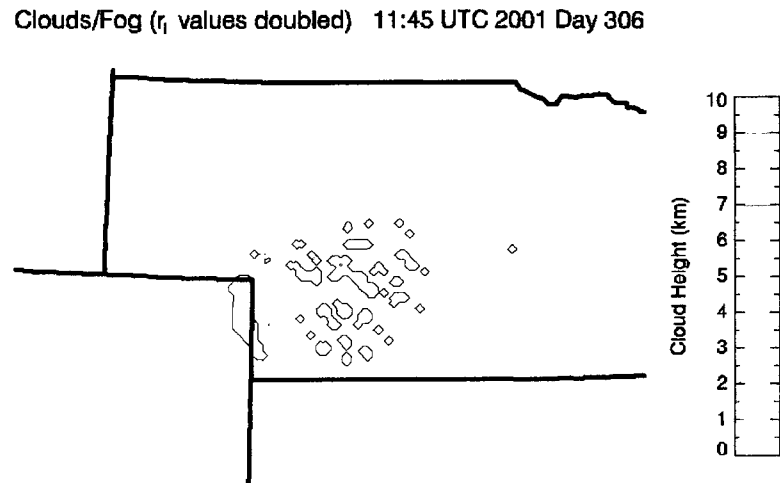


Figure 4.35. Location and height of model-simulated clouds after assimilation of GOES Sounder channels 7 & 11 using doubled decorrelation lengths. Colors indicate height of the top of the cloud layer (km AGL). The lighter blue cloud along the Nebraska-Colorado border formed between 2 and 2.5 km AGL and may be considered mid-level, although it is ~ 1.5 km below the observed altocumulus and much smaller in horizontal extent.

In each experiment, reducing the decorrelation lengths reduced the innovation. This prevented the assimilation from overcoming the large warm and dry biases in the initial model state, leading to higher cost function values. Reducing (increasing) the decorrelation lengths also had the effect of weakening (strengthening) the wind circulations. In each experiment, surface winds speeds were reduced as decorrelation lengths were reduced, while the wind field pattern was largely unchanged. The spatial pattern of the vertical velocity was changed, however, such as in the Sounder-only experiment (Figure 4.36). A similar effect on vertical velocity by changing the decorrelation lengths was found in the Imager and water vapor-only experiments.

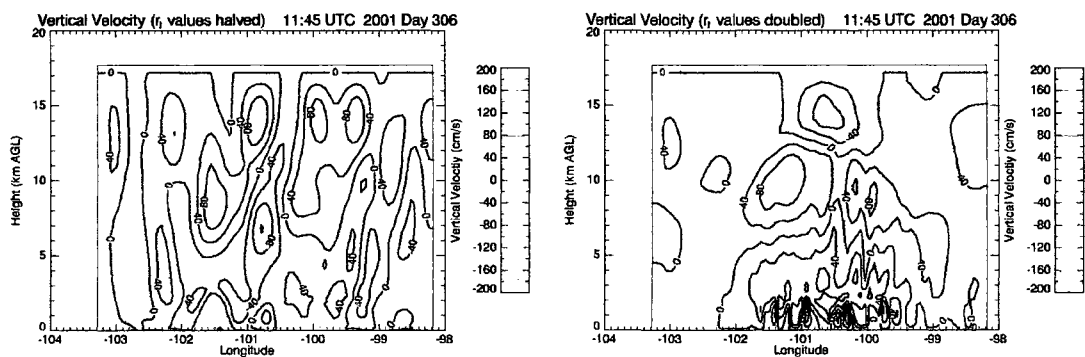


Figure 4.36. X-Z cross-sections of vertical velocity (cm s^{-1}) through North Platte after assimilation of GOES Sounder channels 7 and 11 for the case where the decorrelation lengths have been halved (left) and doubled (right).

4.6 The Effect of Constraining Surface Temperature

The results of the GOES Imager experiment (Section 4.2) highlight the need for additional physical constraints within the 4-DVAR algorithm in order to capture the observed cloud in cloud-free initial conditions. Recall that the most significant changes to the model state after the assimilation of the two Imager channels were that the surface was cooled and upper-tropospheric humidity were increased. This is due to the fact that when the forward model contains no cloud, the adjoint calculates sensitivities based on the assumption there is no cloud. In the case of the GOES Imager experiment, channel 4 is most sensitive to surface temperature and channel 3 is most sensitive to upper-tropospheric humidity when no cloud is present.

In many cases, a change in surface temperature as large as 10 – 15 K as shown in Figure 4.10 is undesired, if not unphysical. For a case over the ocean, for example, a change in surface temperature of similar magnitude would be unphysical since the heat capacity of the ocean prevents the surface temperature from changing that much or that quickly. It is hypothesized that constraining the surface temperature may also benefit the Imager experiment results presented above by forcing the model to change the temperature profile elsewhere to match the brightness temperatures. In this section that hypothesis is tested by re-running the GOES Imager experiment with the constraint that temperatures below 1 km AGL are not allowed to be updated during the minimization. The choice of 1 km as a cut-off for the temperature constraint is due to the fact that it is this layer where the largest changes in temperature occurred (Figure 4.9). The GOES Sounder and Water Vapor-only experiments were re-run with this constraint but, as expected, the results were

almost entirely unchanged due to the fact that the Sounder and water vapor channels are much less sensitive to temperatures in the layer below 1 km AGL.

The observational component of the cost function vs. iteration is shown in Figure 4.37. While the total cost in the original GOES Imager experiment was reduced 71% by the assimilation (Table 4.2), the total cost only decreases by 17% with surface temperatures constrained. This is due to the fact that the warm surface temperature bias is not reduced by the assimilation (by design) and no broad area of cloudiness is formed. In this case, two small patches of cirrus cloud are formed (Figures 4.38 and 4.39). Once again, the cost due to channel 3 is increased as the upper tropospheric humidity was increased too much, particularly in the southern half of the domain where the cirrus clouds are formed (Figure 4.38).

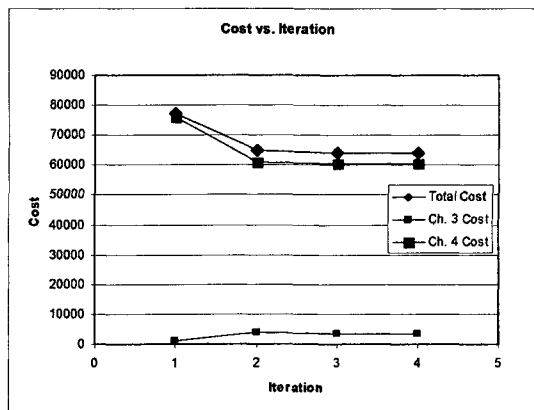
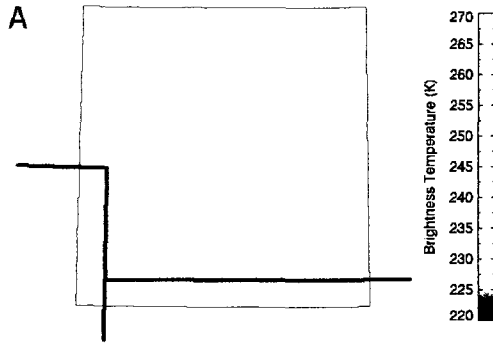
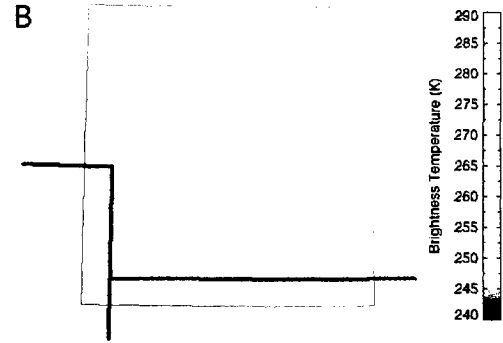


Figure 4.37. The observational component of the cost function vs. iteration number for the assimilation of GOES Imager channels 3 & 4 with temperatures below 1 km AGL constrained. The pink line indicates the cost due to channel 3 observations, the green line indicates the cost due to channel 4 observations and the blue line indicates the total cost of all observations.

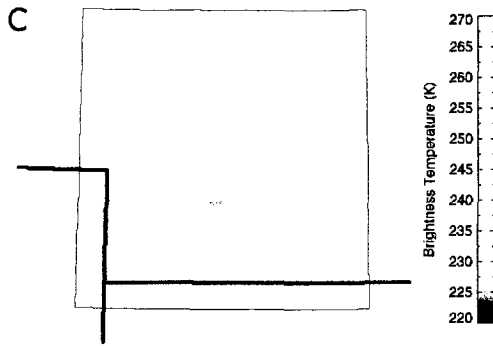
Ch. 3 Model (Before) 11:45 UTC 2001 Day 306



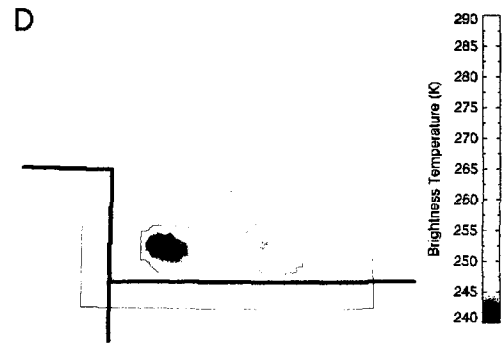
Ch. 4 Model (Before) 11:45 UTC 2001 Day 306



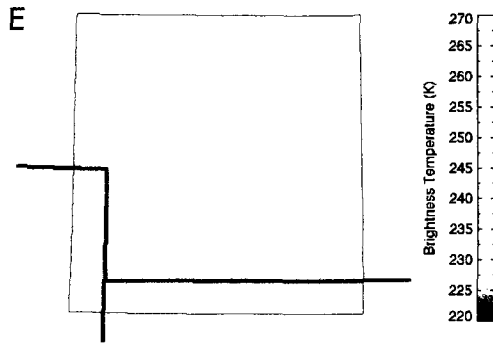
Ch. 3 Model (After) 11:45 UTC 2001 Day 306



Ch. 4 Model (After) 11:45 UTC 2001 Day 306



Ch. 3 Observed 11:45 UTC 2001 Day 306



Ch. 4 Observed 11:45 UTC 2001 Day 306

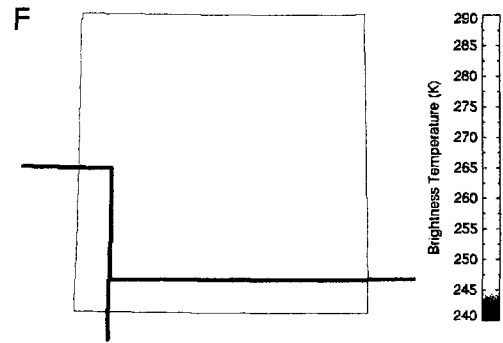


Figure 4.38. Comparison between model-simulated brightness temperatures and observed brightness temperatures for GOES Imager channels 3 and 4 at 11:45 UTC 2 November 2001 with temperatures below 1 km AGL constrained. A – B) Modeled brightness temperatures for channels 3 and 4 before assimilation. C – D) Modeled brightness temperatures for channels 3 and 4 after assimilation. E - F) Observed brightness temperatures from GOES Imager channels 3 and 4.

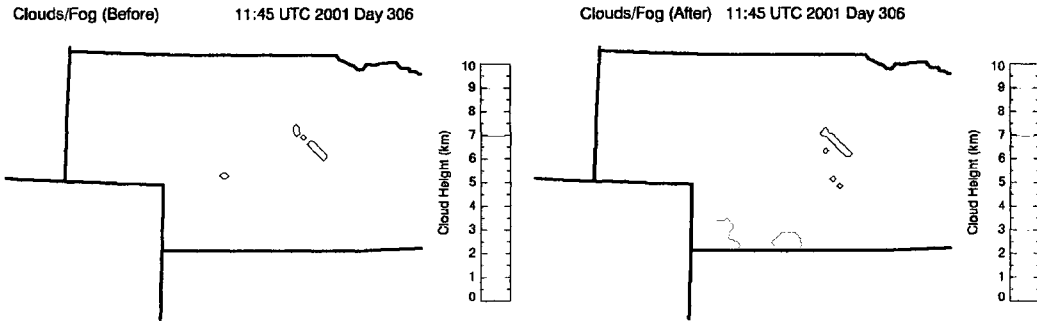


Figure 4.39. Location and height of model-simulated clouds, both before assimilation of GOES Imager ch. 3 and 4 (left) and after assimilation (right) for the case where the temperature was constrained below 1 km. Colors indicate height of the top of the cloud layer (km AGL).

Modeled brightness temperatures from channel 4 in Figure 4.38 reveal changes to the background surface temperature, which are shown more clearly in Figure 4.40. The surface temperatures increase as much as 8 K in the center of the domain. Surface temperatures are reduced by generally 3 – 6 K and as much as 10 K on the west side of the domain. Even though the temperatures below 1 km AGL are not modified directly by the minimization, temperature changes above 1 km AGL mix down to the surface during the 45-minute assimilation period.

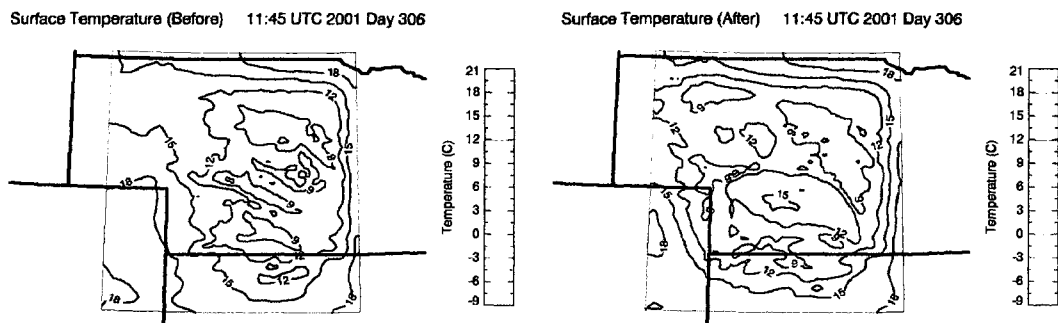


Figure 4.40. Model-simulated surface temperature ($^{\circ}\text{C}$) at 11:45 UTC before assimilation of GOES Imager ch. 3 and 4 (left) and after assimilation (right). In this case, the temperature was constrained below 1 km.

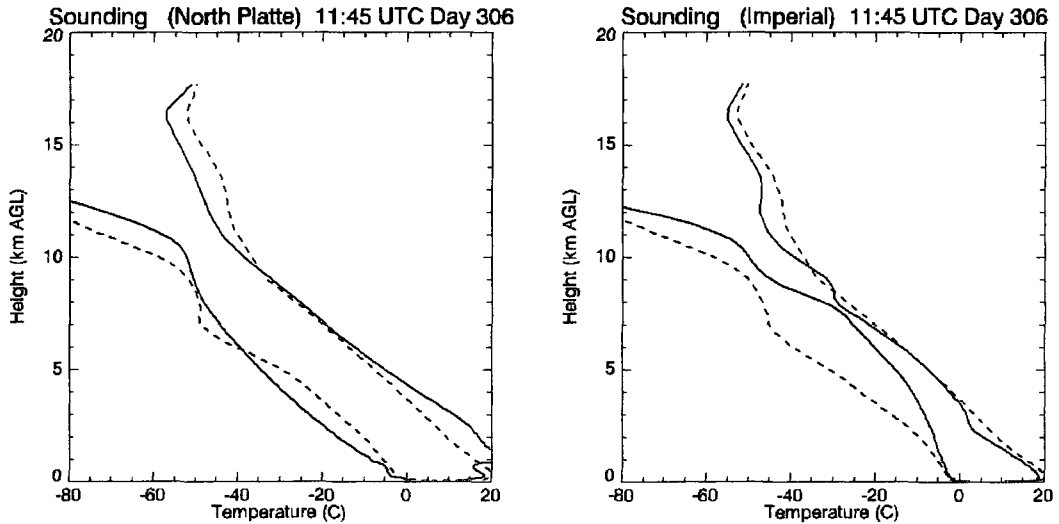


Figure 4.41. Comparison between model-simulated soundings of temperature (red) and dew point (green) at North Platte (left) and Imperial (right), at 11:45 UTC, before assimilation of GOES Imager ch. 3 and 4 (dashed lines) and after assimilation (solid lines).

The temperature changes above 1 km AGL are shown in the soundings at both North Platte and Imperial (Figure 4.41). At North Platte, where the surface temperatures were increased, the model sounding shows that temperatures throughout the troposphere above 1 km AGL were increased. This temperature increase is largest between 1 and 3 km AGL, with a magnitude of 7-8 K. At Imperial, where surface temperatures were cooled, the sounding shows temperatures in the low to mid-troposphere were cooled, with a maximum magnitude of 4 K at 2.3 km AGL.

Vertical cross-sections of relative humidity through Imperial (Figure 4.42) indicate the increase in upper-tropospheric humidity and the approximate level where the cirrus clouds formed. This is similar to the original GOES Imager experiment with no constraint (Figure 4.14), except the relative humidity is generally higher in the upper troposphere with the temperature constraint. This 10 – 20% increase in humidity was enough to form the cirrus clouds. The temperature constraint also prevented fog formation (Figure 4.39) as the constraint indirectly constrained the relative humidity below 1 km AGL.

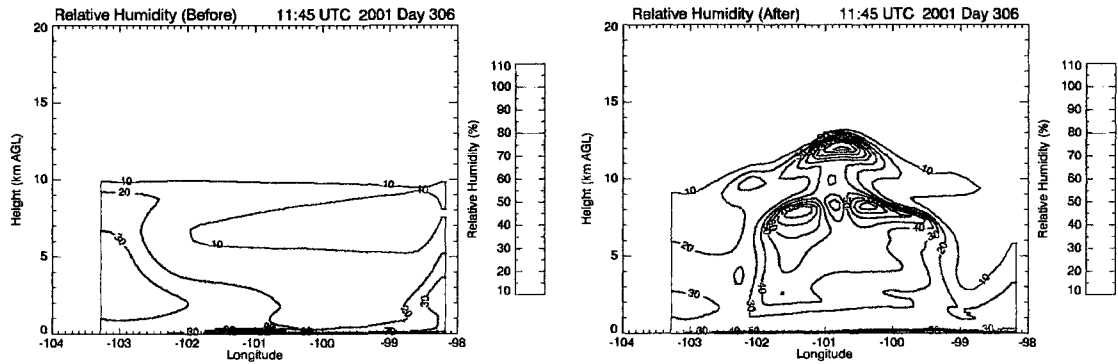


Figure 4.42. X-Z cross section of model-simulated relative humidity through Imperial, NE, at 11:45 UTC both before assimilation of GOES Imager ch. 3 and 4 (left) and after assimilation (right) for the case where temperatures were constrained below 1 km.

It is clear that simply constraining the temperatures below 1 km AGL as done here is not enough to produce the proper cloud. The primary response in this experiment was the increase in upper tropospheric humidity (beyond that of the GOES Imager experiment with no constraint) that led to the production of cirrus clouds. The surface temperature was still modified by the assimilation even with the constraint, due to the changes elsewhere in the state vector feeding back to the surface. The wind field, not shown, was not significantly affected by the temperature constraint.

5. Conclusions

5.1 Discussion of Results

In this work, three experiments were presented that were designed to test the usefulness of assimilating infrared water vapor and window channel data from geostationary satellites into a mesoscale, four-dimensional variational (4-DVAR) data assimilation system (RAMDAS) for the purpose of improving forecasts of mid-level clouds. Mid-level clouds are difficult to forecast because they are typically thin, mixed-phased, associated with relatively weak vertical velocity and form in the mid-troposphere where models typically have coarse vertical resolution and poor moisture information. One case of an isolated, long-lived, mid-level cloud was presented as an ideal case for assimilating this satellite data, and used as the basis of the assimilation experiments.

This case of the altocumulus cloud of 2 November 2001 over North Platte, NE, was poorly handled by the RAMS model initialized with the FNL reanalysis data. The observations contained a cold (260 K cloud top), broad, mid-level cloud, while the model contained only a few small patches of fog and a large (5 – 10 K), warm temperature bias throughout the troposphere. This led to a large brightness temperature bias in both window channels in the model, while the bias in the water vapor channels was not as large due to the fact that the model also overestimated the humidity in the mid- and upper troposphere. The observed mid-level cloud existed near 4 km AGL, where the biases in temperature and dew point were +10 and –10 K, respectively. Subsidence dominated the mid-troposphere in

the model as well, which combined with the temperature and dew point biases to prevent a mid-level cloud from forming.

In this work, the poorly handled initial model simulation is not considered a hindrance and may, in fact, be considered a benefit. As this research was supported by the Department of Defense, it is important to keep in mind the constraints inherent in forecasting for military applications. It is often necessary to set up and run mesoscale models for regions that have little to no regular weather observations (either from surface observing stations or radiosonde launch sites). For these regions, initialization from global model reanalysis data sets, as done in this study, may be a necessity. In addition, satellite observations may be the only source of weather information available. In an assimilation framework, the observations that are assimilated are expected to have a larger impact on the model state in cases where the initial model simulation is poor and this impact would be easier to gauge. The theoretical framework of 4-DVAR has no method of accounting for model error and the attempts at developing a linear model error term for RAMDAS (Zupanski 1997) have not shown any practical benefit in mesoscale satellite data assimilation (Vukićević et al. 2006).

With virtually no cloud present in the initial model simulation, the experiments thus tested the usefulness of assimilating cloudy scene satellite radiance data into a cloud-free model analysis. In each of the experiments presented, satellite radiance data from two different wavelengths at one observation time were assimilated and the impacts on the model analysis were discussed.

The first experiment explored the assimilation of the water vapor channel (6.7 μm , channel 3) and the infrared window channel (10.7 μm , channel 4) from GOES Imager. The primary effects of these data on the analysis were: 1) the surface was cooled and 2) moisture was increased in the upper troposphere. The surface was cooled by 5 – 15 K

throughout the portion of the domain where the cost function was calculated and the initial conditions were adjusted. The increase in humidity in the upper troposphere was most prominent in the southern half of the domain, where the observed brightness temperatures in the water vapor channel were the lowest. Additional fog was produced in the model, but the model was no closer to producing a mid-level cloud.

The second experiment explored the assimilation of the infrared window channel (12.02 μm , channel 7) and the mid-level water vapor channel (7.02 μm , channel 11) from GOES Sounder. The primary effects of the data on the analysis in this experiment were: 1) the atmosphere was cooled and slightly moistened near 2 km AGL, where a subsidence inversion was formed, 2) the atmosphere was moistened in the mid- and upper troposphere, particularly in the center of the domain and 3) the wind field was modified such that rising motion was increased along the boundaries of the cost function domain with subsidence in the mid- and lower troposphere in the center of the domain. The atmosphere was cooled by nearly 15 K at the base of the inversion layer in the center of the domain. The model was much closer to producing a cloud at 2 km AGL, the lower limit of what could be called a mid-level cloud, although this was off by nearly 2 km in the vertical from where the observed cloud existed. The surface was largely unchanged except for the winds, which flowed out from the center of the domain toward the boundaries of the cost function domain, resulting from the subsidence/rising motion pattern mentioned above.

The third experiment explored the assimilation of the two water vapor channels used in the previous experiments, GOES Imager channel 3 and GOES Sounder channel 11, with no window channel data. In this experiment, the data produced a similar effect on the analysis as in the GOES Sounder experiment, except that changes were smaller in magnitude. Cooling of ~ 5 K occurred near 2 km AGL with a slight increase in the dew point, where a subsidence inversion was formed. Moisture was also increased in the mid- and upper troposphere, particularly in the center of the domain, although to a lesser extent than in the

GOES Sounder experiment. The wind field was modified in an identical way to the GOES Sounder experiment, but again with a smaller magnitude change. This experiment produced the smallest magnitude change in the analysis at the surface.

The results of each experiment are explained by the weighting functions of each channel. Weighting functions characterize the emission the satellite would observe at the top of the atmosphere in the wavelength band of the particular channel as a function of height. Theoretical weighting functions for the GOES Imager and Sounder channels used in this study are shown in Figure 5.1, assuming a U.S. standard atmosphere with no clouds. As discussed in Chapter 3, GOES Imager channel 4 is a window channel designed to not be sensitive to any atmospheric constituents, therefore its weighting function peaks at the surface in the absence of clouds. GOES Sounder channel 7, a window channel at a different wavelength, has some sensitivity to lower tropospheric humidity and, as a result, its weighting function peaks above the surface. The two water vapor channels are sensitive to water vapor at different levels, with GOES Imager channel 3 more sensitive to upper tropospheric humidity and GOES Sounder channel 11 more sensitive to mid- tropospheric humidity, which is reflected by their respective weighting functions. The weighting functions represent the layers in which the modeled brightness temperatures are sensitive to changes in the model variables (e.g. temperature, pressure, humidity, etc.) and it is these sensitivities that are calculated by the adjoint.

Given the formulation of the cost function used in this work (equation 3.2), the assimilation system is designed to minimize the difference between the observed and modeled brightness temperatures. In the case of the GOES Imager experiment, the assimilation system minimized this difference by cooling the surface and increasing the upper tropospheric humidity, since this is where channel 3 and channel 4 are most sensitive when no cloud is present. In contrast, the GOES Sounder channels used are more sensitive to changes in the lower to mid- troposphere, where the assimilation produced the most

significant changes to the sounding. The water vapor-only experiment produced changes similar to the Sounder experiment as Sounder channel 11 has sensitivity down to around 2 km AGL, although the initial biases in the water vapor channels were smaller, so the changes to the model state were necessarily smaller.

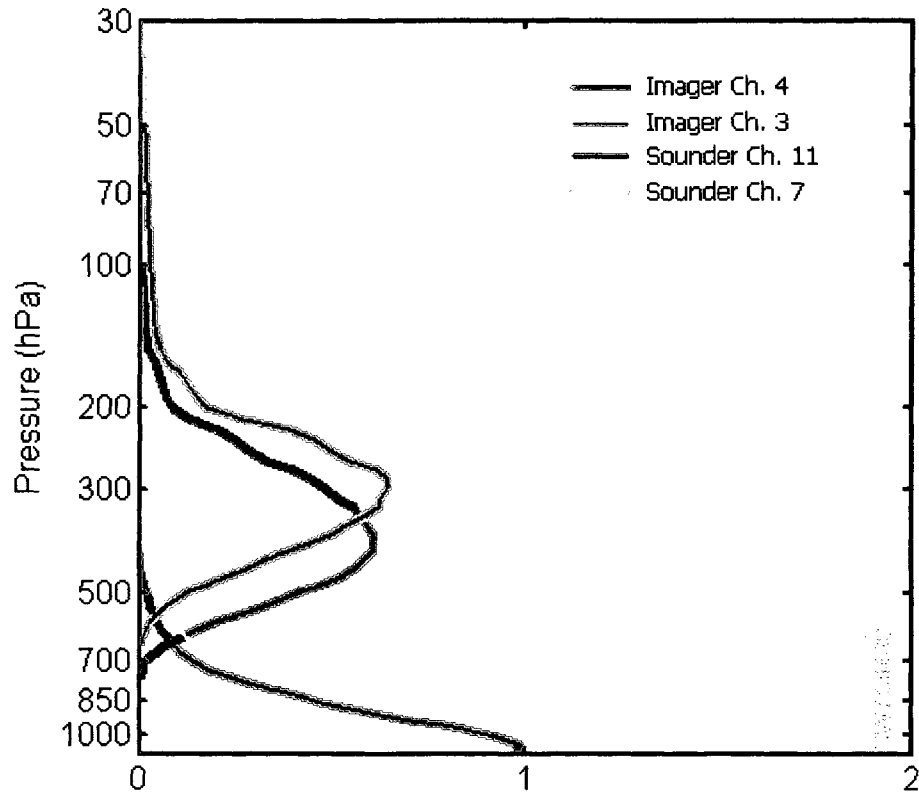


Figure 5.1. Theoretical weighting functions for GOES Imager and Sounder channels used in this study. Image courtesy University of Wisconsin-Madison/CIMMS. The weighting function values have been normalized to the maximum value of GOES Imager channel 4.

The effect of varying the decorrelation lengths was examined for each of the experiments. In each experiment, increasing the decorrelation lengths increased the impact of the observations as evidenced by the larger decreases in the cost function values over the course of the assimilation. This led to more surface cooling in the GOES Imager experiment and more cooling at the inversion height in the GOES Sounder and water vapor-

only experiments. In the GOES Sounder experiment, this also led to the formation of a small cloud between 2 and 2.5 km AGL. Decreasing the decorrelation lengths had the opposite effect, leading to less cooling and reducing the change in the cost function.

It was not shown, but the other variable component of the background error covariance matrix (apart from the decorrelation length), the variance, was also varied by a factor of two. This had no significant impact on the results.

It was also not shown, but another set of the three experiments was run to determine the sensitivity of the results to surface temperature. For the GOES Imager and GOES Sounder experiments, it was determined that adding or removing a surface temperature bias of 5 K was enough to prevent the assimilation system from finding a minimum in the cost function. For the water vapor-only experiment, the results were unaffected by changes in the surface temperature, due to the fact that neither water vapor channel is sensitive to the surface.

A final set of experiments was run in which the near-surface temperatures were constrained. In these experiments, the minimization was prevented from modifying the temperature below 1 km AGL. This constraint had virtually no impact on the GOES Sounder and water vapor-only experiments. Results from the GOES Imager experiment showed that the constraint led to an extra increase in upper-tropospheric humidity beyond that of the GOES Imager experiment with no constraint. This led to the formation of cirrus clouds. The constraint also prevented the formation of fog.

5.2 Conclusions

The results presented in the previous section, combined with the results of Vukićević et al. (2006) allow us to draw some generalized conclusions about the usefulness of assimilating geostationary, infrared satellite data in cloudy scenes using a cloud resolving

mesoscale model. The adjoints calculate the sensitivities of the modeled brightness temperatures to the model variables, which are represented by weighting functions. Vukićević et al. (2006) demonstrated that, in the case where cloud is present in the model, the model's characterization of the cloud may be improved by assimilating satellite observations that are sensitive to the cloud. The adjoint in that case then calculated the sensitivities of the brightness temperatures to the cloud variables (ice water mixing ratio, for example).

In this work, the mid-level cloud present in the observations was not present in the model. Thus, the adjoint calculated sensitivities based on the assumption that there was no cloud. This led to the system modifying the surface temperature in the case of GOES Imager channel 4, as that is what channel 4 is most sensitive to when no clouds are present. The assimilation of the GOES Sounder channels produced better results than the GOES Imager channels from a mid-level cloud forecasting perspective because the Sounder channels used are more sensitive to the state of the low to mid- troposphere.

Brightness temperatures are a non-unique function of atmospheric variables. A cold surface in a clear scene for one case may have the same brightness temperature as a mid-level cloud in another case, depending on the wavelength band of the data and other particulars. This is similar to the problem of cloud detection over snow (Ebert 1987). Additional information (e.g. cloud top pressure) is required for the assimilation to produce a cloud in a cloud-free initial state and put it in the right place.

Vukićević et al. (2006) discussed the importance of lateral boundary conditions on the results of the assimilation. In this work, it was found that the surface temperature also acts as an important boundary condition when assimilating infrared window channel data from satellites.

Decorrelation lengths were found to have a significant impact on the results. Doubling the decorrelation lengths was enough for the assimilation to produce a cloud near 2 km AGL

in the GOES Sounder experiment. Halving the decorrelation lengths produced the smallest magnitude changes to the model state in each experiment. It is thought that using the larger decorrelation lengths produced better results in this case because the observed cloud was broad, and fairly horizontally homogeneous. This is expected to not be the case should this type of experiment be performed on fair weather cumulus, or cumulonimbus clouds, for example, that occur on smaller horizontal spatial scales.

5.3 Future Work

This work should be treated as a preliminary examination of the assimilation of geostationary infrared satellite observations in cloudy scenes where the model has no cloud. It is a goal of this work to serve as guidance and to give direction to possible future work on this topic. While this research focused on the forecasting of mid-level clouds, the results are applicable to other forecasting applications. In particular, these results indicate that the most significant changes to the model state by the assimilation are changes that minimize the largest contributors to the total cost function. It is expected that, in a cloud-free model state, the assimilation of infrared window channels like GOES Imager channel 4 in cloudy scenes would result in a change to the surface temperature, with larger changes from observations of colder clouds. It is also expected that the assimilation of window channels would be more difficult in cases with more complex backgrounds or multiple cloud types or layers.

In a case over the ocean, a change in surface temperature of similar magnitude as the GOES Imager experiment would be unphysical. The heat capacity of the ocean prevents the surface temperature from changing that much or that quickly. The experiment of Section 4.6 addressed this by attempting to constrain the temperatures below 1 km AGL. This simple

constraint did not improve the model analysis from a mid-level cloud forecasting perspective. In addition, it was largely unsuccessful in constraining the surface temperature, as changes to the model state above 1 km, eventually fed back to the surface temperature. Recall also that, in this work, the surface temperature was initially biased by 5 – 10 K throughout the domain. The system should be allowed some freedom in selecting the appropriate surface temperature, but not too much. It is clear that more research needs to be done in this area to develop a better constraint on surface temperatures.

The conclusion that, in a cloud-free model state, the adjoint calculates sensitivities based on the assumption that there is no cloud is a significant one. RAMDAS was designed to handle both clear and cloudy scene radiance assimilation. It is important for the adjoint to calculate sensitivities to cloud when cloud is present and calculate no sensitivity to cloud when cloud is absent. It is suggested that, in cases of a cloud-free model state, the observations themselves may be used to provide information on whether (and where) clouds are present. A cloud mask may be applied (e.g. Coakley and Bretherton 1982) to determine the presence of clouds in the satellite observations and retrievals of cloud top pressure or temperature (e.g. Jones and Vonder Haar 2003) to determine the location of the cloud in the vertical. This information may be used to provide guidance to the assimilation and improve the results.

There are sixteen other infrared and near-infrared channels on the GOES Sounder instrument and two other infrared and near-infrared channels on the current GOES Imager instrument that may be assimilated in the manner presented here. These channels are sensitive to a variety of different levels in the atmosphere and are expected to be more beneficial in some applications than others (e.g. GOES Imager channel 3, which is sensitive to the upper troposphere, would have little to no benefit in a boundary layer stratus case). More research is needed to examine this further.

It should also be noted that the next generation of GOES satellites (GOES-R) will not have an instrument equivalent to the Sounder, although the recently developed Advanced Baseline Imager for GOES-R will retain some of the channels (Schmit et al. 2008). The present work demonstrated that the Sounder provided more useful information in this mid-level cloud application than did the Imager. Perhaps more such studies would provide justification for the development of the next generation sounding instrument.

Based on the results of this work, it is clear that more research needs to be done to determine ideal decorrelation lengths. This is a difficult problem as it is expected that different synoptic conditions have different decorrelation lengths. It may be necessary to devise a system that varies decorrelation lengths based on the synoptic conditions.

The 4-DVAR assimilation system used in this study (RAMDAS) assumes that the errors involved are normally distributed. However, it has been shown that many moisture and cloud variables are not normally distributed and are better represented by a log-normal distribution (Mielke et al. 1977; Miles et al. 2000; Sengupta et al. 2004). The assumption of normally distributed errors for log-normally distributed variables results in the assimilation giving undue weight to model states that are less likely to occur in nature (Fletcher and Zupanski 2007). Formulations of variational data assimilation theory assuming log-normally distributed variables have recently been derived in Fletcher and Zupanski (2006a,b). It is believed that future studies of cloudy-scene radiance data assimilation performed using a log-normal framework would provide more accurate results.

It is important to keep in mind that the experiments presented in this work tested the impact of assimilating data from only one observation time. Vukicevic et al. (2006) showed added benefit by assimilating data from multiple observation times at the highest temporal resolution of the data (15 min. in the case of GOES Imager). In an operational setting, satellite data are typically assimilated continually at the highest temporal resolution possible. Adding observations from more observation times in the case of the GOES Sounder

experiment may be enough on its own to produce a mid-level cloud without making any significant changes to RAMDAS.

6. References

- Barker, D. M., W. Huang, Y.-R. Guo, A. J. Bourgeoise, and Q. N. Xiao, 2004: A Three Dimensional Variational Data Assimilation System for MM5: Implementation and Initial Results. *Monthly Weather Review*, **132**, 897-914.
- Bauer, P., P. Lopez, D. Salmond, A. Benedetti, S. Saarinen, and M. Bonazzola, 2006: Implementation of 1D+4D-Var assimilation of precipitation-affected microwave radiances at ECMWF. II: 4-Dvar. *Quarterly Journal of the Royal Meteorological Society*, **132**, 2307-2332.
- Benjamin, S. G., D. Devenyi, S. S. Weygandt, K. J. Brundage, J. M. Brown, G. A. Grell, D. Kim, B. E. Schwartz, T. G. Smirnova, and T. L. Smith, 2004: An Hourly Forecast Assimilation Cycle: The RUC. *Monthly Weather Review*, **132**, 495-518.
- Black, T. L., 1994: The New NMC Mesoscale Eta Model: Description and Forecast Examples. *Weather and Forecasting*, **9**, 265-278.
- Bower, K. N., S. J. Moss, D. W. Johnson, T. W. Choullarton, J. Latham, P. R. A Brown, A. M. Blyth, and J. Cardwell, 1996: A parameterization of the ice water content observed in frontal and convective clouds. *Quarterly Journal of the Royal Meteorological Society*, **122**, 1815-1844.

- Bryant, F. D. and P. Latimer, 1969: Optical efficiencies of large particles of arbitrary shape and orientation. *Journal of Colloid and Interface Science*, **30**, 291-304.
- Carey, L. D., J. Niu, P. Yang, J. A. Kankiewicz, V. E. Larson and T. H. Vonder Haar, 2008: The Vertical Profile of Liquid and Ice Water Content in Mid-latitude, Mixed-phase Altocumulus Clouds. *Journal of Applied Meteorology and Climatology*, **47**, 2487-2495.
- Coakley, J. A., and F. P. Bretherton, 1982: Cloud Cover From High-Resolution Scanner Data: Detecting and Allowing for Partially Filled Fields of View. *Journal of Geophysical Research*, **87**, 4917-4932.
- Cohn, S. E., 1997: An introduction to estimation theory. *Journal of the Meteorological Society of Japan*, **75**, 257–288.
- Cotton, W. R., R. A. Pielke, Sr., R. L. Walko, G. E. Liston, C. J. Tremback, H. Jiang, R. L. McAnelly, J. Y. Harrington, M. E. Nicholls, G. G. Carrio and J. P. McFadden, 2003: RAMS 2001: Current status and future directions. *Meteorology and Atmospheric Physics*, **82**, 5-29.
- Courtier, P., C. Freydier, J. F. Geleyn, F. Rabier, and M. Rochas, 1991: The ARPEGE project at Météo-France. *Proc. ECMWF Seminar*, Vol. 2, 193–231.
- Cox, S. K., D. S. McDougal, D. A. Randall, and R. A. Schiffer, 1987: FIRE- the First ISCCP Regional Experiment. *Bulletin of the American Meteorological Society*, **88**, 114-118.
- Cucurull, L. and J. C. Derber, 2007: Operational Implementation of COSMIC Observations into NCEP's Global Data Assimilation System. *Weather and Forecasting*, **23**, 702-711.

- Cucurull, L., J. C. Derber, R. Treadon and R. J. Purser, 2008: Preliminary Impact Studies Using Global Positioning System Radio Occultation Profiles at NCEP. *Monthly Weather Review*, **136**, 1865-1877.
- Cullen, M. J. P., 1993: The unified forecast/climate model. *Meteorology Magazine*, **122**, 81-94.
- Deblonde, G. and S. English, 2003: One Dimensional Variational Retrievals from SSMIS Simulated Observations. *Journal of Applied Meteorology*, **42**, 1406-1420.
- Deeter, M., and K. F. Evans, 1998: A hybrid Eddington-single scattering radiative transfer model for computing radiances from thermally emitting atmospheres. *Journal of Quantitative Spectroscopy and Radiative Transfer*, **60**, 635-648.
- Doms, G. and U. Schättler, 2002: A Description of the Non-Hydrostatic Regional Model LM Part I: Dynamics and Numerics. [Available online at <http://cosmo-model.cscs.ch/content/model/documentation/core/default.htm>]
- Ebert, E., 1987: A Pattern Recognition Technique for Distinguishing Surface and Cloud Types in the Polar Regions. *Journal of Climatology and Applied Meteorology*, **26**, 1412-1427.
- Evans, K. F., 1998: The spherical harmonics discrete ordinate method for three-dimensional atmospheric radiative transfer. *Journal of the Atmospheric Sciences*, **55**, 429-446.
- Fan, X. and J. S. Tilley, 2005: Dynamic Assimilation of MODIS-Retrieved Humidity Profiles within a Regional Model for High- Latitude Forecast Applications. *Monthly Weather Review*, **133**, 3450-3480.

- Ferrare, R. A., S. H. Melfi, D. N. Whiteman, K. D. Evans, F. J. Schmidlin, and D. O'C Starr, 1995: A Comparison of Water Vapor Measurements made by Raman Lidar and Radiosondes. *Journal of Atmospheric and Oceanic Technology*, **12**, 1177-1195.
- Field, P. R., 1999: Aircraft Observations of Ice Crystal Evolution in an Altostratus Cloud. *Journal of the Atmospheric Sciences*, **56**, 1925-1941.
- Fleishauer, R. P., 2001: Observed Microphysical and Radiative Structure of Mid-level, Mixed-phase Clouds. CSU PhD Dissertation, Colorado State University, Ft. Collins, CO, 176 pp.
- Fleishauer, R. P., V. E. Larson and T. H. Vonder Haar, 2002: Observed Microphysical Structure of Midlevel, Mixed-Phase Clouds. *Journal of the Atmospheric Sciences*, **59**, 1779-1804.
- Fletcher, S. J. and M. Zupanski, 2006a: A data assimilation method for log-normally distributed observational errors. *Quarterly Journal of the Royal Meteorological Society*, **132**, 2505-2519.
- Fletcher, S. J. and M. Zupanski, 2006b: A hybrid multivariate normal and lognormal distribution for data assimilation. *Atmospheric Science Letters*, **7**, 43-46.
- Fletcher, S. J. and M. Zupanski, 2007: Implications and impacts of transforming lognormal variables into normal variables in VAR. *Meteorologische Zeitschrift*, **15**, 1-11.
- Fowler, L. D., and D. A. Randall, 1996: Liquid and Ice Cloud Microphysics in the CSU General Circulation Model: Part III. Sensitivity to Modeling Assumptions. *Journal of Climate*, **9**, 561-586.

- Fowler, L. D., D. A. Randall and S. A. Rutledge, 1996: Liquid and Ice Cloud Microphysics in the CSU General Circulation Model: Part I. Model Description and Simulated Microphysical Processes. *Journal of Climate*, **9**, 489-529.
- Fu, Q. and K. N. Liou, 1992: On the Correlated k-distribution Method for Radiative Transfer in Non-homogeneous Atmospheres. *Journal of the Atmospheric Sciences*, **49**, 2139-2156.
- Garand, L. and J. Hallé, 1997: Assimilation of Clear and Cloudy Sky Upper Tropospheric Humidity Estimates Using GOES-8 and GOES-9 Data. *Journal of Atmospheric and Oceanic Technology*, **14**, 1036-1054.
- Gedzelman, S. D., 1988: In Praise of Altocumulus. *Weatherwise*, **41**, 143-149.
- Greenwald, T. J., R. Hertenstein and T. Vukićević, 2002: An all-weather observational operator for satellite radiance assimilation with mesoscale forecast models. *Monthly Weather Review*, **130**, 1882-1897.
- Greenwald, T. J., T. Vukićević, L. D. Grasso and T. H. Vonder Haar, 2004: Adjoint sensitivity analysis of an observational operator for cloudy visible and infrared radiance assimilation. *Quarterly Journal of the Royal Meteorological Society*, **130**, 685-705.
- Ha, S.-Y., Y.-H. Kuo, Y.-R. Guo, and G.-Y. Lim, 2003: Variational Assimilation of Slant-Path Wet Delay Measurements from a Hypothetical Ground-Based GPS Network. Part I: Comparison with Precipitable Water Assimilation. *Monthly Weather Review*, **131**, 2635-2655.

- Harrington, J. Y., 1997: The effects of radiation and microphysical processes on simulated warm and transition season Arctic stratus. CSU PhD Dissertation, Colorado State University, Ft. Collins, CO, 289 pp.
- Harrington, J. Y., T. Reisin, W. R. Cotton, and S. M. Kreidenweis, 1999: Cloud Resolving Simulations of Arctic Stratus Part II: Transition-Season Clouds. *Atmospheric Research*, **51**, 45-75.
- Heymsfield, A. J. and L. M. Miloshevich, 1993: Homogeneous Ice Nucleation and Supercooled Liquid Water in Orographic Wave Clouds. *Journal of the Atmospheric Sciences*, **50**, 2335-2353.
- Heymsfield, A. J., L. M. Miloshevich, A. Slingo, K. Sassen, and D. O'C. Starr, 1991: An Observational and Theoretical Study of Highly Supercooled Altocumulus. *Journal of the Atmospheric Sciences*, **48**, 923-945.
- Hobbs, P. V. and A. L. Rangno, 1985: Ice Particle Concentrations in Clouds. *Journal of the Atmospheric Sciences*, **42**, 2523-2549.
- Hobbs, P. V. and A. L. Rangno, 1998: Microstructures of Low and Middle-Level Clouds over the Beaufort Sea. *Quarterly Journal of the Royal Meteorological Society*, **124**, 2035-2071.
- Hoffman, R. N., C. Grassotti, R. G. Isaacs, J.-F. Louis, and T. Nehr Korn, 1990: Assessment of Simulated Satellite Lidar Wind and Retrieved 183 GHz Water Vapor Observations on a Global Data Assimilation System. *Monthly Weather Review*, **118**, 2513-2542.

- Hogan, T. F. and T. E. Rosmond, 1991: The Description of the Navy Operational Global Atmospheric Prediction System's Spectral Forecast Model. *Monthly Weather Review*, **119**, 1786–1815.
- Holton, J. R., 1992: *An Introduction to Dynamic Meteorology*. Academic Press, 511pp.
- Huang, X.-Y., and P. Lynch, 1993: Diabatic digital-filtering initialization: Application to the HIRLAM model. *Monthly Weather Review*, **121**, 589–603.
- Illingworth, A. J., R. J. Hogan, E. J. O'Connor, D. Bouniol, M. E. Brooks, J. Delanoë, D. P. Donovan, J. D. Eastment, N. Gaussiat, J. W. F. Goddard, M. Haeffelin, H. Klein Baltink, O. A. Krasnov, J. Pelon, J.-M. Piriou, A. Protat, H. W. J. Russchenberg, A. Seifert, A. M. Tompkins, G.-J. van Zadelhoff, F. Vinit, U. Willén, D. R. Wilson, and C. L. Wrench, 2007: Cloudnet. *Bulletin of the American Meteorological Society*, **88**, 883–898
- Jones, A. S. and T. H. Vonder Haar, 2002: A Dynamic Parallel Data-Computing Environment for Cross-Sensor Satellite Data Merger and Scientific Analysis. *Journal of Atmospheric and Oceanic Technology*, **19**, 1307-1317.
- Jones, C. G., U. Willén, A. Ullerstig, and U. Hansson, 2004. The Rossby Centre Regional Atmospheric Climate Model Part I: Model Climatology and Performance for the Present Climate over Europe. *Ambio*, **33:4-5**, 199-210.
- Jones, J. C. and T. H. Vonder Haar, 2003: Comparisons of Satellite-derived Cloud Heights with Radar Measurements of Mid-level, Mixed-phase Clouds. CSU Masters Thesis, Colorado State University, Ft. Collins, CO, 66 pp.

- Kalnay, E., 2003: *Atmospheric Modeling, Data Assimilation and Predictability*. Cambridge University Press, 341 pp.
- Kanamitsu, M., J. C. Alpert, K. A. Campana, P. M. Caplan, D. G. Deaven, M. Iredell, B. Katz, H.-L. Pan, J. Sela, and G. H. White, 1991: Recent changes implemented into the global forecast system at NMC. *Weather and Forecasting*, **6**, 425-435.
- Khairoutdinov, M. F. and D. A. Randall, 2003: Cloud resolving modeling of the ARM Summer 1997 IOP: Model formulation, results, uncertainties, and sensitivities. *Journal of Atmospheric Science*, **60**, 607-625.
- King, M. D., W. P. Menzel, Y. J. Kaufman, D. Tanre, B.-C. Gao, S. Platnick, S. A. Ackerman, L. A. Remer, R. Pincus, and P. A. Hubanks, 2003: Cloud and aerosol properties, precipitable water, and profiles of temperature and water vapor from MODIS. *IEEE Transactions on Geosciences and Remote Sensing*, **41**, 442–458.
- Kley, D., J. M. Russell, III, and C. Phillips (eds.), 2000: SPARC Assessment of Upper Tropospheric and Stratospheric Water Vapor. *World Meteorological Organization Technical Document 143*. World Climate Research Programme, Geneva.
- Korolev, A. and G. Isaac, 2003: Phase Transformation of Mixed-phase Clouds. *Quarterly Journal of the Royal Meteorological Society*, **129**, 19-38.
- Korolev, A. V., G. A. Isaac, S. G. Cober, J. W. Strapp and J. Hallett, 2003: Microphysical characterization of mixed-phase clouds. *Quarterly Journal of the Royal Meteorological Society*, **129**, 39-65.

- Koyama, T., T. Vukićević, M. Sengupta, T. H. Vonder Haar, and A. S. Jones, 2006: Analysis of Information Content of Infrared Sounding Radiances in Cloudy Conditions. *Monthly Weather Review*, **134**, 3657-3667.
- Larson, V. E., R. P. Fleishauer, J. A. Kankiewicz, D. L. Reinke and T. H. Vonder Haar, 2001: The Death of an Altocumulus Cloud. *Geophysical Research Letters*, **28**, 2609-2612.
- Larson, V. E., K. E. Kotenburg and N. B. Wood, 2007: An analytic longwave radiation formula for liquid layer clouds. *Monthly Weather Review*, **135**, 689-699.
- Larson, V. E., A. J. Smith, M. J. Faulk, K. E. Kotenberg and J.-C. Golaz, 2006: What determines altocumulus dissipation time? *Journal of Geophysical Research*, **111**, D19207, doi: 10.1029/2005JD007002.
- Lawson, R. P., B. A. Baker, and C. G. Schmitt, 2001: An overview of microphysical properties of Arctic clouds observed in May and July 1998 during FIRE ACE. *Journal of Geophysical Research*, **106**, 14989-15014.
- Lenderink, G., B. J. J. M. van den Hurk, E. van Meijgaard, A. P. van Ulden, and H. Cuijpers, 2003: Simulation of present-day climate in RACMO2: first results and model developments. Technical Report TR-252, Royal Netherlands Meteorological Institute, De Bilt.
- Lesht, B. M. and J. C. Liljegren, 1997: Comparison of Precipitable Water Vapor Measurements Obtained by Microwave Radiometers and Radiosondes at the Southern Great Plains Cloud and Radiation Testbed Site. *Proceedings of the Sixth Atmospheric Radiation Measurement Science Team Meeting, San Antonio, TX*. 165-168.

- Li, Z. -X. and H. Le Treut, 1992: Cloud-radiation feedbacks in a general circulation model and their dependence on cloud modeling assumptions. *Climate Dynamics*, **7**, 133-139.
- Liu, S. and S. K. Krueger, 1998: Numerical Simulations of Altocumulus Using a Cloud Resolving Model and a Mixed Layer Model. *Atmospheric Research*, **47-48**, 461-474.
- Ma, X. L., T. J. Schmit, and W. L. Smith, 1999: A Nonlinear Physical Retrieval Algorithm – Its Application to the GOES 8/9 Sounder. *Journal of Applied Meteorology*, **38**, 501-513.
- MacDonald, A. E., 2005: A Global Profiling System for Improved Weather and Climate Prediction. *Bulletin of the American Meteorological Society*, **86**, 1747-1764.
- Marecal, V. and J.- F. Mahfouf, 2002: Four-Dimensional Variational Assimilation of Total Column Water Vapor in Rainy Areas. *Monthly Weather Review*, **130**, 43-58.
- McFarquhar, G. M. and S. G. Cober, 2004: Single-scattering properties of mixed-phase Arctic clouds at solar wavelengths: impacts on radiative transfer. *Journal of Climate*, **17**, 3799-3813.
- McFarquhar, G. M., A. J. Heymsfield, J. Spinhirne and B. Hart, 2000: Thin and Subvisual Tropopause Tropical Cirrus: Observations and Radiative Impacts. *Journal of the Atmospheric Sciences*, **57**, 1841–1853.
- McMillin, L. M., L. J. Crone, M. D. Goldberg, and T. J. Kleespies, 1995: Atmospheric transmittance of an absorbing gas, 4. OPTRAN: A computationally fast and accurate transmittance model for absorbing gases with fixed and variable mixing ratios at variable viewing angles. *Journal of Applied Optics*, **34**, 6269-6274.

- McNally, A. P., J. C. Derber, W.-S. Wu and B. B. Katz, 2000: The use of TOVS level-1B radiances in the NCEP SSI analysis system. *Quarterly Journal of the Royal Meteorological Society*, **126**, 689-724.
- McNally, A. P., and M. Vesperini, 1996: Variational Analysis of Humidity Information from TOVS Radiances. *Quarterly Journal of the Royal Meteorological Society*, **122**, 1521-1544.
- Menzel, W. P., and J. F. W. Purdom, 1994: Introducing *GOES-I*: The first of a new generation of geostationary operational environmental satellites. *Bulletin of the American Meteorological Society*, **75**, 757-781.
- Meyers, M. P., R. L. Walko, J. Y. Harrington, and W. R. Cotton, 1997: New RAMS cloud microphysics parameterization. Part II: The two-moment scheme. *Atmospheric Research*, **45**, 3-39.
- Mielke, P. W., J. S. Williams and S.-C. Wu, 1977: Covariance analysis techniques based upon bivariate lognormal distribution with weather modification applications. *Journal of Applied Meteorology*, **16**, 183-187.
- Miles, N. L., J. Verlinde and E. E. Clothiaux, 2000: Cloud droplet size distribution in low-level stratiform clouds. *Journal of the Atmospheric Sciences*, **57**, 295-311.
- Miloshevich, L. M., H. Vomel, A. Paukkunen, A. J. Heymsfield and S. J. Oltmans, 2001: Characterization and Correction of Relative Humidity Measurements from Vaisala RS80A Radiosondes at Cold Temperatures. *Journal of Atmospheric and Oceanic Technology*, **18**, 135-155.

- Mokhov, I. and M. E. Schlesinger, 1993: Analysis of Global Cloudiness, Part I: Comparison of METEOR, Nimbus-7 and ISCCP Satellite Data, *Journal of Geophysical Research*, **98**, 12849-12868.
- Niu, J., L. D. Carey, P. Yang, and T. H. Vonder Haar, 2008: Optical properties of a vertically inhomogeneous, midlatitude, mid-level, mixed-phase altocumulus in the infrared region. *Atmospheric Research*, in press.
- Nocedal, J., 1980: Updating quasi-Newton matrices with limited storage. *Mathematics of Computation*, **35**, 773–782.
- Paltridge, G. W., W. J. King and C. M. R. Platt, 1986: A Case Study of Ice Particle Growth in a Mixed-Phase Altostratus Cloud. *Australian Meteorology Magazine*, **34**, 149-154.
- Parrish, D. F. and J. C. Derber, 1992: The National Meteorological Center's Spectral Statistical Interpolation Analysis System. *Monthly Weather Review*, **120**, 1747-1763.
- Pielke, R. A., and Coauthors, 1992: A comprehensive meteorological modeling system—RAMS. *Meteorology and Atmospheric Physics*, **49**, 69–91.
- Pinto, J. O., 1998: Autumnal Mixed-Phase Cloudy Boundary Layers in the Arctic. *Journal of the Atmospheric Sciences*, **55**, 2016-2037.
- Poetsch-Heffter, C., Q. Liu, E. Ruperecht, and C. Simmer, 1995: Effect of Cloud Types on the Earth Radiation Budget Calculated with the ISCCP CI Dataset: Methodology and Initial Results. *Journal of Climate*, **8**, 829-843.
- Rabier, F., H. Jarvinen, E. Klinker, J-F Mahfouf and A. Simmons, 2000: The ECMWF Operational Implementation of Four-Dimensional Variational Assimilation Part I:

- Experimental Results with Simplified Physics, *Quarterly Journal of the Royal Meteorological Society*, **126**, 1143-1170.
- Rasch, P. J. and J. E. Kristjansson, 1998: A comparison of the CCM3 model climate using diagnosed and predicted condensate parameterizations. *Journal of Climate*, **11**, 1587-1614.
- Rauber, R. M. and A. Tokay, 1991: An Explanation for the Existence of Supercooled Water at the Tops of Cold Clouds. *Journal of the Atmospheric Sciences*, **48**, 1005-1023.
- Raymond, W. H., G. S. Wade and T. H. Zapotocny, 2004: Assimilating GOES Brightness Temperatures. Part I: Upper-Tropospheric Moisture. *Journal of Applied Meteorology*, **43**, 17-27.
- Reale, A. L., D. G. Gray, M. W. Chalfont, A. Swaroop and A. Nappi, 1986: Higher resolution operational satellite retrievals. *2nd Conference on Satellite Meteorology/Remote Sensing and Applications*, American Meteorological Society, Boston, pp. 16-19.
- Ritter, B. and J. F. Geleyn, 1992: A Comprehensive Radiation Scheme for Numerical Weather Prediction Models with Potential Applications in Climate Situations. *Monthly Weather Review*, **120**, 303-325.
- Rossow, W. B., and E. N. Dueñas, 2004: The ISCCP Web Site, an Online Source for Research, *Bulletin of the American Meteorological Society*, **85**, 167-172.
- Ruggiero, F. H., K. D. Sashegyi, A. E. Lipton, R. V. Madala, and S. Raman, 1999: Coupled Assimilation of Geostationary Satellite Sounder Data into a Mesoscale Model Using the Bratseth Analysis Approach. *Monthly Weather Review*, **127**, 802-821.

- Ruston, B. C., and T. H. Vonder Haar, 2004: Characterization of summertime microwave emissivities from the Special Sensor Microwave Imager over the conterminous United States. *Journal of Geophysical Research*, **109**, D19103, doi:10.1029/2004JD004890.
- Schiffer, R. A. and W. B. Rossow, 1983: The International Satellite Cloud Climatology Project (ISCCP): The First Project of the World Climate Research Programme. *Bulletin of the American Meteorological Society*, **64**, 779-784.
- Schmit, T. J., Ju. Li, J. J. Gurka, M. D. Goldberg, K. J. Schrab, Ji. Li, and W. F. Feltz, 2008: The GOES-R Advanced Baseline Imager and the Continuation of Current Sounder Products. *Bulletin of the American Meteorological Society*, **89**, 2696-2711.
- Seaman, C. J. and T. H. Vonder Haar, 2003: *Observed and Calculated Properties of Mid-level, Mixed-phase Clouds*. Masters Thesis, Colorado State University, Fort Collins, CO, 92 pp.
- Seaman, C. J., J. A. Kankiewicz, J. M. Davis and K. E. Eis, 2005: Simulated Transmissivity of Mid-level, Mixed-phase Clouds. *Battlespace Atmosphere and Cloud Impacts on Military Operations (BACIMO) Conference 2005*, Monterey, CA, 12-14 October 2005.
- Sengupta, M., E. E. Clothiaux and T. P. Ackerman, 2004: Climatology of warm boundary layer clouds at the ARM SGP site and their comparisons to models. *Journal of Climate*, **17**, 4760-4782.
- Shanno, D. F., 1950: Globally convergent conjugate gradient algorithms. *Mathematical Programming*, **33**, 61-67.

- Smith, R. N. B. 1990: A scheme for predicting layer clouds and their water content in a general circulation model. *Quarterly Journal of the Royal Meteorological Society*, **116**, 435-460.
- Soden, B. J. and F. P. Bretherton, 1993: Upper Tropospheric Relative Humidity from GOES-7: Method and Climatology for July 1987. *Journal of Geophysical Research*, **98**, 16669-16688.
- Soden, B. J., S. A. Ackerman, D. O'C. Starr, S. H. Melfi and R. A. Ferrare, 1994: Comparison of Upper Tropospheric Water Vapor from GOES, Raman Lidar, and CLASS Sonde Measurements. *Journal of Geophysical Research*, **99**, 21005-21016.
- Soden, B. J., D. D. Turner, B. M. Lesht, and L. M. Miloshevich, 2004: An Analysis of Satellite, Radiosonde, and Lidar Observations of Upper Tropospheric Water Vapor from the ARM Program. *Journal of Geophysical Research*, **109**, D04105.
- Starr, D. O'C., 1987: A Cirrus Cloud Experiment: Intensive Field Observations Planned for FIRE. *Bulletin of the American Meteorological Society*, **68**, 119-124.
- Stephens, G. L., 1994: *Remote Sensing of the Lower Atmosphere*, Oxford University Press, New York, NY, 523 pp.
- Stephens G. L., R. G. Ellingson, J. Vitko Jr., W. Bolton, T. P. Tooman, F. P. J. Valero, P. Minnis, P. Pilewskie, G. S. Phipps, S. Sekelsky, J. R. Carswell, S. D. Miller, A. Benedetti, R. B. McCoy, R. F. McCoy Jr., A. Lederbuhr, and R. Bambha, 2000: The Department of Energy's Atmospheric Radiation Measurement (ARM) Unmanned Aerospace Vehicle (UAV) Program. *Bulletin of the American Meteorological Society*, **81**, 2915–2938.

- Stephens, G. L., S. Tsay, P. W. Stackhouse, P. J. Flatau, 1990: The Relevance of Microphysical and Radiative Properties of Cirrus Clouds to Climate and Climatic Feedback. *Journal of the Atmospheric Sciences*, **47**, 1742-1753.
- Stephens, G. L., D. G. Vane, R. J. Boain, G. G. Mace, K. Sassen, Z. Wang, A. J. Illingworth, E. J. O'Connor, W. B. Rossow, S. L. Durden, S. D. Miller, R. T. Austin, A. Benedetti, C. Mitrescu, and the CLOUDSAT Science Team, 2002: The CLOUDSAT Mission and the A-Train: A New Dimension of Space-Based Observations of Clouds and Precipitation. *Bulletin of the American Meteorological Society*, **83**, 1771-1790.
- Stunder, B. J. B., 1997: NCEP Model Output – FNL Archive Data. TD-6141, National Climatic Data Center. [Available online at <http://www.arl.noaa.gov/fnl.php>]
- Sun, Z., and K. P. Shine, 1994: Studies of the Radiative Properties of Ice and Mixed-Phase Clouds. *Quarterly Journal of the Royal Meteorological Society*, **120**, 111-137.
- Sun, Z., and K. P. Shine, 1995: Parameterization of Ice Cloud Radiative Properties and Its Application to the Potential Climatic Importance of Mixed-Phase Clouds. *Journal of Climate*, **8**, 1874-1888.
- Tripoli, G. J. and W. R. Cotton, 1982: The Colorado State University three-dimensional cloud/mesoscale model – 1982. Part I: General theoretical framework and sensitivity experiments. *Journal de Recherches Atmospheriques*, **16**, 185-219.
- Tulich, S. N. and T. H. Vonder Haar, 1998: Measured and Calculated Structures of a Multi-Layer Altocumulus Cloud. Masters Thesis, CSU Atmospheric Science Paper #647, Colorado State University, Ft. Collins, CO, 190 pp.

- Turner, D. D., B. M. Lesht, S. A. Clough, J. C. Liljegren, H. E. Revercomb, and D. C. Tobin, 2003: Dry Bias and Variability in Vaisala Radiosondes: The ARM Experience. *Journal of Atmospheric and Oceanic Technology*, **20**, 117-132.
- van Leeuwen, P. J., 2001: An ensemble smoother with error estimates. *Monthly Weather Review*, **129**, 709-728.
- Verlinde, J., J. Y. Harrington, G. M. McFarquhar, V. T. Yannuzzi, A. Avramov, S. Greenberg, N. Johnson, G. Zhang, M. R. Poellot, J. H. Mather, D. D. Turner, E. W. Eloranta, B. D. Zak, A. J. Prenni, J. S. Daniel, G. L. Kok, D. C. Tobin, R. Holz, K. Sassen, D. Spangenberg, P. Minnis, T. P. Tooman, M. D. Ivey, S. J. Richardson, C. P. Bahrmann, M. Shupe, P. J. DeMott, A. J. Heymsfield and R. Schofield, 2007: The Mixed-Phase Arctic Cloud Experiment. *Bulletin of the American Meteorological Society*, **88**, 205-221.
- Vonder Haar, T. H., S. K. Cox, G. L. Stephens, J. M. Davis, T. L. Schneider, W. A. Peterson, A. C. Huffman, K. E. Eis, D. L. Reinke and J. M. Forsythe, 1997: Overview and Objectives of the DoD Center for Geosciences Sponsored "Complex Layered Cloud Experiment". Preprints, Cloud Impacts on DoD Operations and Systems Conference, September 23-25, Newport, R.I.
- Vukićević, T., T. Greenwald, M. Zupanski, D. Zupanski, T. Vonder Haar and A. Jones, 2004: Mesoscale cloud state estimation from visible and infrared satellite radiances. *Monthly Weather Review*, **132**, 3066-3077.
- Vukićević, T., M. Sengupta, A. S. Jones and T. H. Vonder Haar, 2006: Cloud Resolving Satellite Data Assimilation: Information Content of IR Window Observations and Uncertainties in Estimation. *Journal of the Atmospheric Sciences*, **63**, 901-919.

- Walko, R. L., L. E. Band, J. Baron, T. G. F. Kittel, R. Lammers, T. J. Lee, D. Ojima, R. A. Pielke, Sr., C. Taylor, C. Tague, C. J. Tremback, and P. L. Vidale, 2000: Coupled Atmosphere-Biophysics-Hydrology Models for Environmental Modeling. *Journal of Applied Meteorology*, **39**, 931-944.
- Walko, R., W. R. Cotton, M. P. Meyers, and J. Y. Harrington, 1995: New RAMS cloud microphysics parameterization. Part I: The single-moment scheme. *Atmospheric Research*, **38**, 29–62.
- Walko, R. L. and C. J. Tremback, 2002: Regional Atmospheric Modeling System Version 4.3/4.4 Model Input Namelist Parameters. [Available online at <http://www.atmet.com/html/docs/documentation.shtml>]
- Wang, J., H. L. Cole, D. J. Carlson, E. R. Miller, K. Beirle, A. Paukkunen, and T. K. Laine, 2002: Corrections of Humidity Measurement Errors from the Vaisala RS80 Radiosonde- Application to TOGA-COARE Data. *Journal of Atmospheric and Oceanic Technology*, **19**, 981-1002.
- Warren, S. G., C. J. Hahn, J. London, R. M. Chervin and R. Jenne, 1986: Global Distribution of Total Cloud Cover and Cloud Type Amount Over Land. NCAR TN-317 STR, 212 pp.
- Warren, S. G., C. J. Hahn, J. London, R. M. Chervin and R. Jenne, 1988: Global Distribution of Total Cloud Cover and Cloud Type Amount Over the Ocean. NCAR TN-317 STR, 212 pp.
- Weng, F., T. Zhu and B. Yan, 2007: Satellite Data Assimilation in Numerical Weather Prediction Models. Part II: Uses of Rain-Affected Radiances from Microwave

Observations for Hurricane Vortex Analysis. *Journal of the Atmospheric Sciences*, **64**, 3910-3925.

Wu, X., G. R. Diak, C. M. Hayden and J. A. Young, 1995: Short-Range Precipitation Forecasts Using Assimilation of Simulated Satellite Water Vapor Profiles and Column Cloud Liquid Water Amounts. *Monthly Weather Review*, **123**, 347-365.

Yang, P., H. Wei, B. A. Baum, H. Huang, A. J. Heymsfield, Y. X. Hu, B. Gao and D. D. Turner, 2003: The spectral signature of mixed-phase clouds composed of nonspherical ice crystals and spherical liquid droplets in the terrestrial window region. *Journal of Quantitative Spectroscopy and Radiative Transfer*, **79-80**, 1171-1188.

Zapotocny, T. H., W. P. Menzel, J. P. Nelson III, and J. A. Jung, 2002: An Impact Study of Five Remotely Sensed and Five In Situ Data Types in the Eta Data Assimilation System. *Weather and Forecasting*, **17**, 263-285.

Zhang, M., W. Lin, C. S. Bretherton, J. J. Hack, and P. J. Rasch, 2003: A modified formulation of fractional stratiform condensation rate in the NCAR Community Atmospheric Model (CAM2). *Journal of Geophysical Research*, **108**, 4035, doi: 10.1029/2002JD002523.

Zuidema, P., B. Baker, Y. Han, J. Intrieri, J. Key, P. Lawson, S. Matrosov, M. Shupe, R. Stone and T. Uttal, 2005: An Arctic springtime mixed-phase cloudy boundary layer observed during SHEBA. *Journal of Atmospheric Science*, **62**, 160-176.

Zupanski, D., 1997: A general weak constraint applicable to operational 4DVAR data assimilation systems. *Monthly Weather Review*, **125**, 2274-2292.

- Zupanski, M., 1993: A preconditioning algorithm for large-scale minimization problems. *Tellus*, **45A**, 478-492.
- Zupanski, M., 1996: A preconditioning algorithm for four-dimensional variational data assimilation. *Monthly Weather Review*, **124**, 2562–2573.
- Zupanski, M., D. Zupanski, D. Parrish, E. Rogers, and D. DiMego, 2002: Four-dimensional variational data assimilation for the blizzard of 2000. *Monthly Weather Review*, **130**, 1967–1988.
- Zupanski, M., D. Zupanski, T. Vukićević, K. Eis, and T. Vonder Haar, 2005: CIRA/CSU four-dimensional variational data assimilation system. *Monthly Weather Review*, **133**, 829–843.